Looking for the Blake River in the Swayze: Characterization of Volcanic Rocks in the Swayze Area, Abitibi Greenstone Belt, Ontario

By

Aidan Buyers

A Thesis Submitted to
Saint Mary's University, Halifax, Nova Scotia
in Partial Fulfillment of the Requirements for
the Degree of Bachelor of Science in Geology

April 30, 2023, Halifax, Nova Scotia

Approved: Dr. Jacob Hanley
Supervisor, Full Professor

Approved: Kevin Neyedley
Second Reader

Date: April 30, 2023

Looking for the Blake River in the Swayze: Characterization of Volcanic Rocks in the Swayze Area, Abitibi Greenstone Belt, Ontario

By: Aidan Buyers

Abstract

The Abitibi Greenstone Belt's VMS mineralization has been largely constrained to several key chronostratigraphic volcanic assemblages. The most productive of these is the Blake River assemblage (2704 – 2695 Ma). Blake River volcanism in the Swayze area has long since been identified by other workers, however no economic VMS deposits have been identified. The study area for this project comprises two large felsic volcanic packages in the central Swayze area in the western Abitibi, previously mapped as part of the Blake River. A sub-economic VMS occurrence hosted in the southern package. This study found that these two packages of rock have distinctly different chemical characteristics from each other, indicating a genetic relationship between them is unlikely. The two groups show (i) differing levels of HREE depletion and LREE concentration, (ii) different zircon trace element fractionation trends, (iii) and are of different ages. Neither of these groups of samples display REE signatures of felsic volcanics that are typically associated with Archean VMS deposits (e.g., FII, FIIIa, and FIIIb rhyolites). Furthermore, zircon U-Pb CA-ID-TIMS indicate that these two volcanic packages are not Blake River aged, but in fact belong to the assemblages that temporally flank the Blake River: the Tisdale and Porcupine assemblages. This study exemplifies the powerful synergy of using whole rock geochemistry, zircon trace element chemistry, and zircon U-Pb dating to distinguish between nearby volcanic assemblages in the Abitibi Greenstone Belt.

Date: April 30, 2023

Table of Contents

Abstract--2

List of Figures--5

List of Tables--6

Acknowledgements---7

1.0 Introduction--8

2.0 Background Information--11

2.1 – Abitibi Greenstone Belt--11

2.2 – Sedimentary Successor Basins--20

2.3 – Swayze Area---21

2.4 – VMS Deposits---23

3.0 Methods--24

3.1 Field Mapping and Sampling--24

3.2 Whole Rock Geochemistry---25

3.3 Petrography---26

3.4 Heavy mineral separation and mount preparation-----------------------------------26

3.5 Zircon LA-ICP-MS---28

3.6 Zircon SEM-BSE-EDS--30

3.7 Zircon U-Pb CA-ID-TIMS--30

3.8 Mirco-XRF--34

4.0 Results--34

4.1 Field Relationships--34

4.2 Petrography---38

4.3 Whole Rock Geochemistry---43

4.4 VMS Mineralization---47

4.5 Zircon Textural Interpretation--55

4.6 Zircon Trace Element Data---60

4.7 Zircon U-Pb CA-ID-TIMS Geochronology---70

5.0 Discussion---71

5.1 Zircon Trace Element Concentrations--72

5.2 Group 1---73

5.3 Group 2---74

5.3 VMS Viability---77

5.4 Technical Synergy---80

6.0 Conclusions--81

6.1 Recommendations for Future Work---81

References--82

List of Figures

Figure 1: Map of the superior province and its subprovinces-------------------------------------12

Figure 2: Geological assemblage map of the Abitibi Greenstone Belt---------------------------14

Figure 3: Geological assemblage map of the Swayze area showing the study area------------22

Figure 4: Lithological map of the Swayze, Dore, and Garnet townships-----------------------35

Figure 5: Field photos of outcrops encountered in the study area-------------------------------36

Figure 6: Photomicrographs of unmineralized samples---39

Figure 7: Accessory mineral photomicrographs--42

Figure 8: Whole rock geochemistry plots---44

Figure 9: Field photos of a Swayze VMS occurrence--49

Figure 10: Schematic diagram of VMS occurrence and scans of mineralized samples-------51

Figure 11: Photomicrographs of mineralized samples---52

Figure 12: Micro XRF elemental maps and scans of mineralized samples---------------------54

Figure 13: Scans of samples from which zircon were obtained-----------------------------------57

Figure 14: CL images of select zircon---59

Figure 15: Zircon trace element plots Sm_{CN}/Ce_{CN} vs Yb_{CN}/Gd_{CN}--------------------------------62

Figure 16: Zircon trace element plots Th/U vs Yb_{CN}/Gd_{CN}--65

Figure 17: Zircon trace element plots Hf vs Ti--69

Figure 18: Relative ore mineral abundances of mineralized samples---------------------------79

List of Tables

Table 1: Correlation between assemblage and stratigraphic nomenclature--------------------17

Table 2: REE groups of felsic volcanics in the study area--47

Supplemental Material Tables (separate documents)

Table 1: Sample list

Table 2: Whole rock geochemistry

Table 3: Optical petrography

Table 4a: Mineralized sample data and geochemistry

Table 4b: Mineralized sample petrography

Table 5: Zircon CA-ID-TIMS data

Table 6: Zircon LA-ICP-MS data

Acknowledgements

I would like to deeply thank my supervisor Dr. Jacob Hanley for his guidance and patience throughout this project. I would also like to thank Kevin Neyedley for his crucial help during this process. I would like to thank Thomas Gemmell for his invaluable contributions and personal support during the field season, and while writing this thesis. I would also like to thank him for inspiring throughout my career so far in geology. I would like to thank field assistants Ben Bates, Emilia Butty, Johnathan Enright, and Sarah Mills for their contributions during the field season and continued friendship afterward. I would like to acknowledge and thank the Boise State University Isotope Geology Laboratory staff for the tireless and excellent work they put into our samples. Specific thanks are given to Dr. Jim Crowley, Leticia Sutherland and Krystl Malhas for their work on our samples and the hospitality they showed me during my visit. I would like to acknowledge Saint Mary's University faculty members Dr. Mitch Kerr, Xiang Yang, Dr. Erin Adlakha and staff member Delaney Carter for their help and use of their equipment during this project. I would like to thank Dr. Michael Hamilton from the Jack Slatterly Geochronology Laboratory at University of Toronto for his help sourcing archived zircon. This project would not have been possible without the support of the Ontario Geological Survey and Metal Earth Research Centre. Funding for this project was supplied to Dr. Hanley by the Natural Sciences and Engineering Research Council of Canada (NSERC) and Targeted Geoscience Initiative – 6 (TGI-6). Additional research funding was given to the author via the Society of Economic Geologists Canada Foundation Award.

1.0 Introduction

Volcanogenic massive sulphide (VMS) deposits are important sources of Cu, Zn and to a lesser extent Pb, Ag, Au, Cd, Se, Sn, In and Bi (Gibson et al. 2007); many of these metals Canada has deemed critical in the transition towards a “greener” economy (Natural Resources Canada, 2022). The Abitibi Greenstone Belt (AGB) is host to many of Canada’s most strategic and economically important VMS deposits. Therefore, developing a robust understanding of how, when, and where in the volcanic stratigraphy these deposits formed is critical for identifying prospective areas in the AGB.

The AGB is divided into seven volcanic chronostratigraphic assemblages (Figure 2), most recently characterized by Ayer et al. (2002b, 2005) and Thurston et al. (2008). Three of these assemblages host the vast majority of economic VMS mineralization. The Deloro (2734 -2724 Ma), hosts the largest number of VMS deposits at 36, with a total ore contribution of 158 Mt. The Kidd-Munro hosts only three deposits, but these contain 196.6 Mt of ore (170.9 Mt at Kidd Creek mine; Hannington et al., 2017). The Blake River (BR; ~2704 – 2695 Ma) is the most metal endowed volcanic episode in the AGB (Mercier-Langevin et al. 2011). The 30 VMS deposits associated with this assemblage account for ~46% of the total VMS tonnage (at 357.0 Mt), and ~92% of the total VMS gold endowment of the entire AGB (Monecke et al., 2017; data from Franklin et al., 2005; Galley et al., 2007; Mercier-Langevin et al., 2011a; Mercier-Langevin and Bécu (unpublished data)). In the eastern ABG, the Noranda and Doyon-Bousquet-LaRonde (DBL) mining camps are hosted in BR rocks and contain world class Au-rich VMS deposits (Quemont; 2.46 Moz Au, Horne; 11.4 Moz Au, Bousquet 2-Dumagami; 3.6 Moz Au, and LaRonde Penna; 9.2 Moz Au) (McNicoll et al., 2014). The main area where the importance of the BR was realized, and the rocks characterized, is an ellipsoidal area bound by the Porcupine-Destor and Cadillac-Larder Lake regional fault zones to the north and south, respectively. This is where all of the aforementioned Au-rich VMS deposits are hosted.

Independent of these periods of productive VMS mineralization, several characteristics are common among all VMS mineral systems. High temperature hydrothermal systems are what drive the scavenging and exhalative concentration of economic minerals in VMS deposits. To power these hydrothermal systems, models invoke the presence of a shallow sub-volcanic intrusion of sufficient size and temperature to produce and maintain these hydrothermal convection cells (Cathles, 1981; Cathles et al., 1997). These intrusions may also contribute magmatic fluids to the hydrothermal system during their emplacement (Herzig et al., 1998). Deep faults that penetrate the volcanic strata are often important features to focus the recharge and discharge of metal laden fluids at or near the seafloor (Gibson et al., 2007). Extensional tectonic settings have been identified in nearly all VMS environments, and their importance is multifold. During extension the crust is thinned which depressurizes and allows the mantle to well up to shallower levels and initiate melting at the base of the crust, which produces mafic melts. If rifting is long lived and these mafic melts fractionate sufficiently, felsic melts can be derived from them (Gibson et al., 2007). The extensional faults create thermal corridors that can be important magma pathways to encourage the ascent and emplacement of shallow magma bodies. They also grant cross-stratal structural permeability, which allows the hydrothermal fluids to interact with a larger volume of rock (Gibson et al., 2007).

The Swayze Area is located ~200 km west of the DBL, north of the western expression of the Larder Lake-Cadillac Fault Zone (LLCFZ), locally known as the Rideout (Figure 2). Past workers, through regional mapping and geochronological studies, have identified BR volcanics in the

Swayze Area (Heather 2001; van Breemen et al., 2006). However, no economic VMS deposits have been found. During recent mapping initiatives by the Ontario Geological Survey, a VMS-style massive sulphide lens hosted in suspected BR rocks was identified. Despite being composed of largely barren sulphides (pyrrhotite and pyrite), this occurrence, and the BR rocks of the Swayze as a whole, provide an opportunity for research to be conducted on an area that shares some characteristics with world class mining districts. The contrasting distribution of VMS deposits between the eastern and western regions of the AGB is not well understood.

This study investigates possible causes for the discrepancy by looking closely at the geochemical characteristics of the magmatic systems that produced suspected barren BR rocks in the Swayze area, so that comparisons can be made between these and the more productive eastern AGB systems.

To characterize the rocks hosting (and proximal to), a sub-economic VMS occurrence in the Swayze area, mapping was done and representative samples of volcanic rocks from different stratigraphic levels were taken in order to characterize them by whole rock geochemistry and petrography. To aid in this characterization, several samples of felsic volcanics were also sent for heavy mineral separation so that zircon crystals could be obtained for zircon chemistry, U-Pb geochronology, and future melt inclusion studies. Separates of previously dated zircons from the study area were also obtained from the Ontario Geological Survey and Jack Slaterley Labs at the University of Toronto, to add to the coverage. Zircons have long since been identified to record the magmatic histories of the igneous rocks they are found in, both by capturing trace element contents from different stages of their growth, as well as being reliable U-Pb geochronometers for Archean rocks. Furthermore, they often trap silicate melt inclusions (SMI), representing samples of the unadulterated melt from which the zircons were crystalizing from. In this study, these techniques will be used to characterize the volcanic rocks in the Swayze Area in order to confidently place them into the chronostratigraphic groups of the AGB and comment on the area's VMS potential.

2.0 Background Information

2.1 Abitibi Greenstone Belt

The AGB is a uniquely well-preserved Neoarchean terrane, that is dominantly composed of metavolcanic rocks, with significant metasedimentary components. The belt lies in the north-eastern part of the Wawa-Abitibi subprovince and forms the southeastern part of the Superior province, straddling the Ontario-Quebec border (Figure 1). The majority of the supracrustal rocks of the AGB were formed over a ~125 m.y. period, spanning from 2795-2670 Ma.

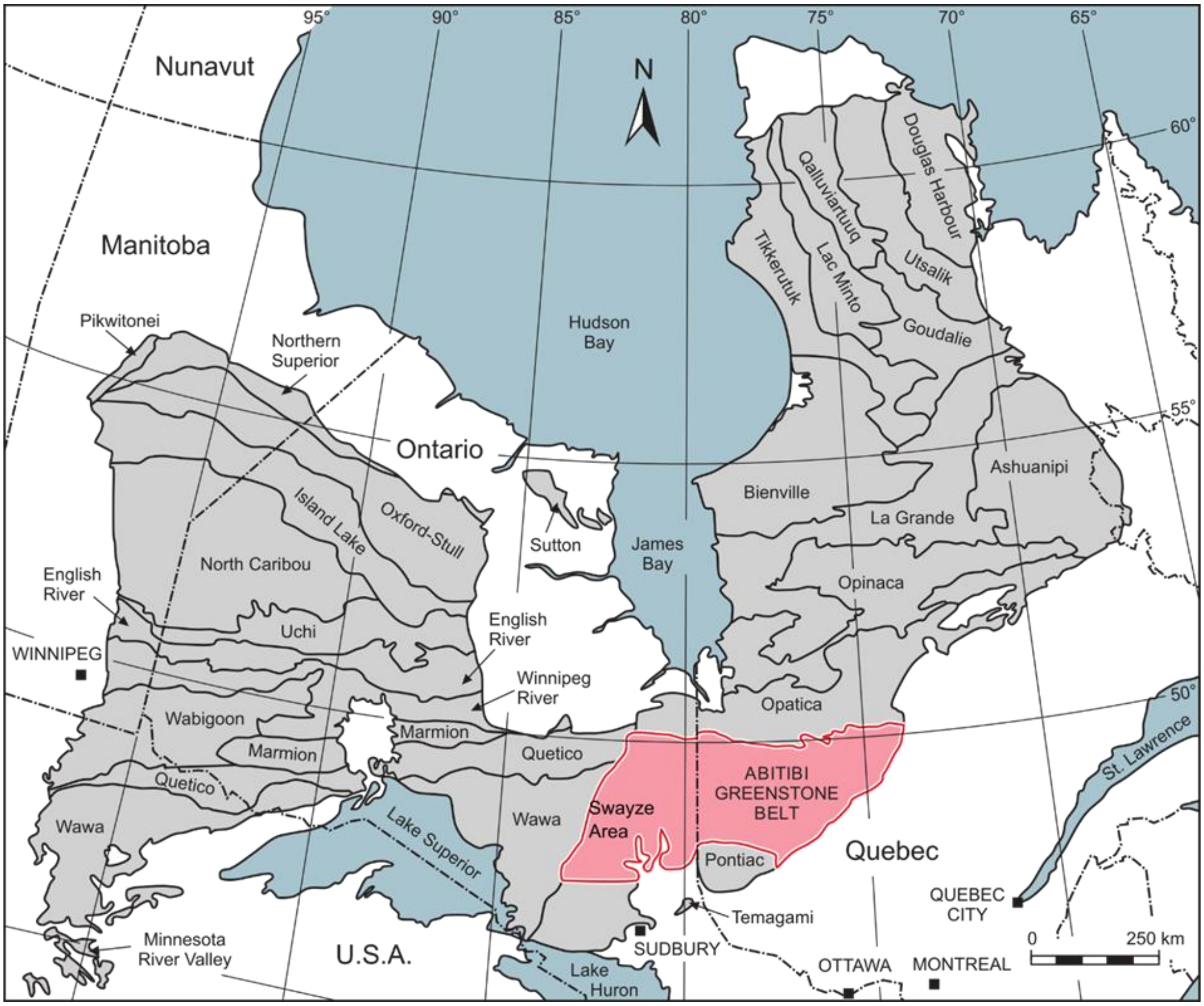

Figure 1: The Superior province and its subprovinces. Abitibi Greenstone Belt shown in red. Modified from Moneke et al., 2017.

The AGB is truncated by the 500 km long NNE trending Kapuskasing Structural Zone to the west. The Kapuskasing Structural Zone is a west dipping Paleoproterozoic thrust that brought granulite facies Archean lower continental crust to the surface (Percival and West, 1994; Percival et al., 1989). To the north the AGB is bound by the Opatica subprovince, a dominantly meta-intrusive suite consisting of high-grade metamorphic rocks that structurally underlie the AGB (Benn and Moyen, 2008; Figure 1). To the east the AGB is truncated by the Grenville Front tectonic zone (Mesoproterozoic age). The Grenville Front tectonic zone is a series of south-dipping thrust faults that juxtapose higher grade metamorphic rocks adjacent to the AGB.

The southeastern portion of the AGB is in contact with the Pontiac subprovince, a succession of greywacke and mudstone with intercalated units of conglomerate; and the AGB was thrusted upon these sedimentary packages (Rocheleau, 1980; Lajoie and Ludden, 1984; Camiré and Burg, 1993; Benn et al., 1994; Daigneault et al., 2002; Bedeaux et al., 2017). In the south and southwest the AGB is unconformably overlain by the Paleoproterozoic Huronian supergroup consisting of a southward thickening package of sedimentary rocks deposited in a rift to passive margin setting (Young and Nesbit, 1985; Bennett et al., 1991; Young et al., 2001).

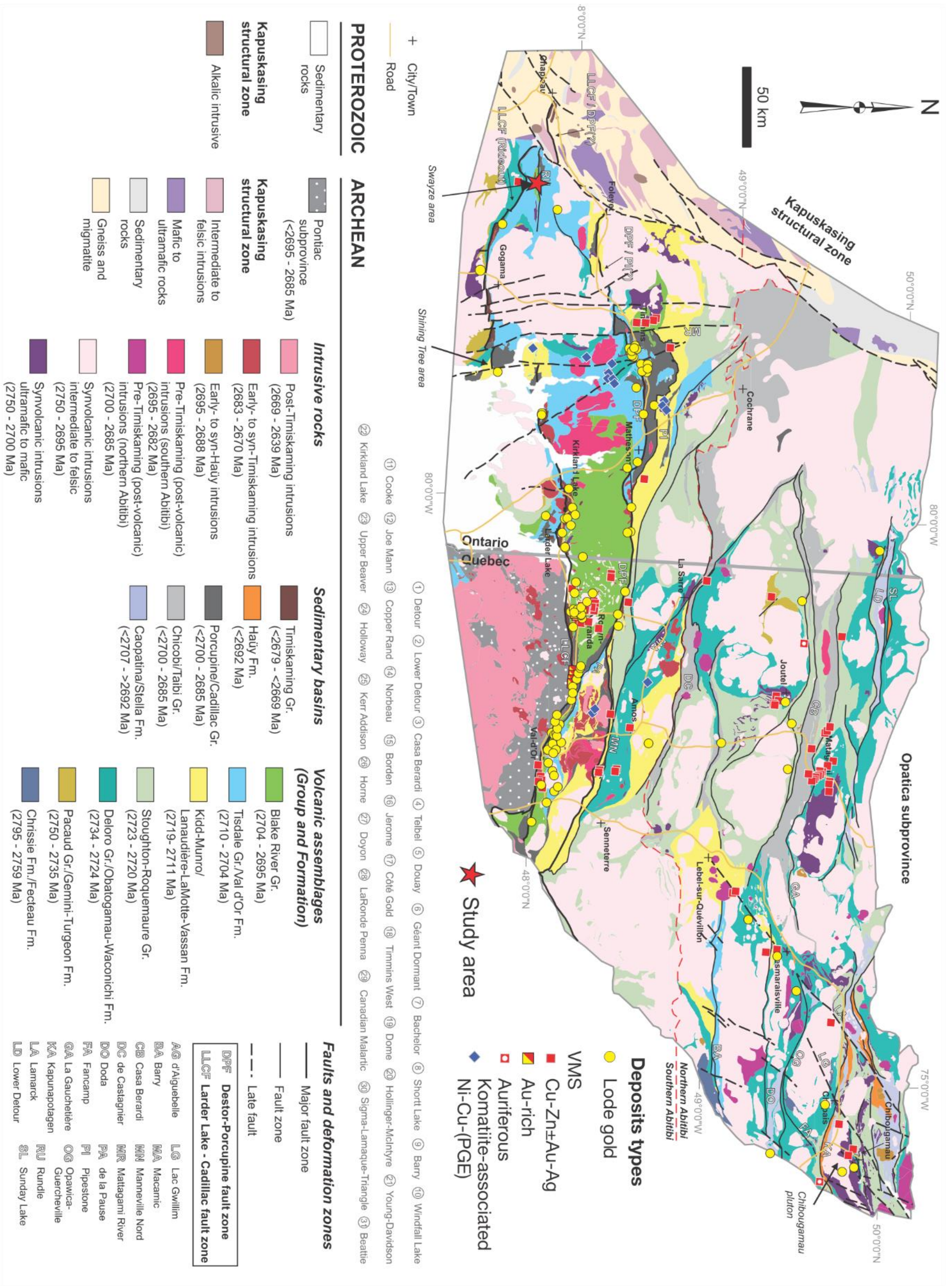
N
50 km
Kapuskasing structural zone
Opatica subprovince
Study area
Swayze area
Shining Tree area
Chapleau
Foleyet
Gogama
Timmins
Cochrane
Matheson
Kirkland Lake
Larder Lake
Rouyn-Noranda
Val-d'Or
Amos
La Sarre
Joutel
Matagami
Senneterre
Lebel-sur-Quévillon
Desmaraisville
Chapais
Chibougamau
Chibougamau pluton
Ontario
Quebec
49°0'0"N
50°0'0"N
48°0'0"N
80°0'0"W
75°0'0"W
Northern Abitibi
Southern Abitibi
Deposits types
Lode gold
VMS
Cu-Zn±Au-Ag
Au-rich
Auriferous
Komatiite-associated Ni-Cu-(PGE)
① Detour ② Lower Detour ③ Casa Berardi ④ Telbel ⑤ Douay ⑥ Géant Dormant ⑦ Bachelor ⑧ Shortt Lake ⑨ Barry ⑩ Windfall Lake
⑪ Cooke ⑫ Joe Mann ⑬ Copper Rand ⑭ Norbeau ⑮ Borden ⑯ Jerome ⑰ Côté Gold ⑱ Timmins West ⑲ Dome ⑳ Hollinger-McIntyre ㉑ Young-Davidson
㉒ Kirkland Lake ㉓ Upper Beaver ㉔ Holloway ㉕ Kerr Addison ㉖ Horne ㉗ Doyon ㉘ LaRonde Penna ㉙ Canadian Malartic ㉚ Sigma-Lamaque-Triangle ㉛ Beattie
+ City/Town
Road
PROTEROZOIC
Sedimentary rocks
Kapuskasing structural zone
Alkalic intrusive
ARCHEAN
Pontiac subprovince (<2695 - 2685 Ma)
Kapuskasing structural zone
Intermediate to felsic intrusions
Mafic to ultramafic rocks
Sedimentary rocks
Gneiss and migmatite
Intrusive rocks
Post-Timiskaming intrusions (2669 - 2639 Ma)
Early- to syn-Timiskaming intrusions (2683 - 2670 Ma)
Early- to syn-Haüy intrusions (2695 - 2688 Ma)
Pre-Timiskaming (post-volcanic) intrusions (southern Abitibi) (2695 - 2682 Ma)
Pre-Timiskaming (post-volcanic) intrusions (northern Abitibi) (2700 - 2685 Ma)
Synvolcanic intrusions intermediate to felsic (2750 - 2695 Ma)
Synvolcanic intrusions ultramafic to mafic (2750 - 2700 Ma)
Sedimentary basins
Timiskaming Gr. (<2679 - <2669 Ma)
Haüy Fm. (<2692 Ma)
Porcupine/Cadillac Gr. (<2700 - 2685 Ma)
Chicobi/Taïbi Gr. (<2700 - 2685 Ma)
Caopatina/Stella Fm. (<2707 - >2692 Ma)
Volcanic assemblages (Group and Formation)
Blake River Gr. (2704 - 2695 Ma)
Tisdale Gr./Val d'Or Fm. (2710 - 2704 Ma)
Kidd-Munro/Lanaudière-LaMotte-Vassan Fm. (2719- 2711 Ma)
Stoughton-Roquemaure Gr. (2723 - 2720 Ma)
Deloro Gr./Obatogamau-Waconichi Fm. (2734 - 2724 Ma)
Pacaud Gr./Gemini-Turgeon Fm. (2750 - 2735 Ma)
Chrissie Fm./Fecteau Fm. (2795 - 2759 Ma)
Faults and deformation zones
Major fault zone
Fault zone
Late fault
DPF Destor-Porcupine fault zone
LLCF Larder Lake - Cadillac fault zone
AG d'Aiguebelle
BA Barry
CB Casa Berardi
DC de Castagnier
DO Doda
FA Fancamp
GA La Gauchetière
KA Kapunapotagen
LA Lamarck
LD Lower Detour
LG Lac Gwillim
MA Macamic
MN Manneville Nord
MR Mattagami River
PA de la Pause
PI Pipestone
OG Opawica-Guercheville
RU Rundle
SL Sunday Lake
LLCF / DPF?
LLCF (Ridout)
DPF / PI (?)
RU
MR
DPF
PI
LLCF
DC
CB
MN
GA
BA
OG
LG
DO
FA
KA
LA
LD
SL

Figure 2: Map of the Abitibi Greenstone Belt showing the volcanic assemblages and the locations of mineral deposits. Location of the Swayze Area (study area) shown with a red star. Modified after Dubé and Mercier-Langevin, (2020) and Monecke et al. (2017).

The AGB is generally made up of east-trending folds of metavolcanic and metasedimentary rocks, and variable exposures of granitic intrusive rocks. The rock's compositions range from felsic to ultramafic and are of tholeiitic to calc-alkaline affinity. A summary of the seven volcanic assemblages and their local stratigraphic nomenclature is presented in Table 1. On small scale maps, the AGB appears to consist of laterally continuous mafic and felsic metavolcanic and metasedimentary units. However, more detailed mapping has revealed that, due to a lack of consistent marker horizons, it is difficult to correlate volcanic units over large distances. Chemical metasedimentary units (ironstones and/or banded iron formations) are more clearly laterally continuous over large distances. These chemical sedimentary rocks are important for understanding the construction of the AGB as they represent periods of volcanic quiescence and can be important when evaluating the VMS potential of a given area or lithological package (Thurston et al., 2008).

The belt has been divided into the northern and southern Abitibi Greenstone Belt historically. This subdivision was based on the volume of intrusive rocks exposed and the metamorphic grade. In the northern AGB, ~ 40% of the exposed outcrops are intrusive rocks and the metamorphic grade is greenschist to amphibolite facies. In the south, ~ 20% of the outcrops are intrusive rocks and the metamorphic grade is generally lower (prehnite-pumpellyite to lower greenschist facies). Upon the discovery that equivalent units in the north and south are of similar ages, a conclusion was made that these discrepancies were likely due to different levels of exhumation (Bleeker, 2012, 2015).

Table 1: Correlation Between Assemblage and Stratigraphic Nomenclature for the Southern Abitibi Greenstone Belt[1, 2] (From Monecke et al., 2017)

Assemblage	Group	Formations[3]	Geographic distribution (references)
Timiskaming	Indian Lake Group		Shining Tree area (this paper)
(≤2679–≤2669 Ma)	Pamour Group	Dome Fm.	Timmins area (Dubé et al., 2017; this paper)
		Three Nations Fm.	
	Ridout Group	Opeepeesway Fm.	Swayze area (this paper)
	Timiskaming Group	Duparquet Fm.	Duparquet area (this paper)
		Granada Fm.	Rouyn-Noranda area (Poulsen, 2017; this paper)
		La Bruère Fm.	
		McWatters Fm.	
Porcupine	Cadillac Group		Rouyn-Noranda, Doyon-Bousquet-LaRonde, Cadillac, Malartic, and Val-d’Or areas (De Souza et al.,
(≤2690–≤2685 Ma)			2017; Houlé et al., 2017; Mercier-Langevin et al., 2017a, b; Poulsen, 2017; this paper)
	Hearst Group		Larder Lake area (Poulsen, 2017; this paper)
	Kewagama Group	Caste Fm.	Rouyn-Noranda, Doyon-Bousquet-LaRonde, Preissac Lake, Cadillac, Malartic, and Val-d’Or areas
		Mont-Brun Fm.	(De Souza et al., 2017; Houlé et al., 2017; Mercier-Langevin et al., 2017a, b; Poulsen, 2017; this paper)
	Porcupine Group	Beatty Fm.	Timmins area (Dubé et al., 2017; this paper)
		Hoyle Fm.	
		Krist Fm.	
		Whitney Fm.	
Blake River	Blake River Group	Hébécourt Fm.	Rouyn-Noranda area (Poulsen, 2017; Monecke et al., 2017; this paper)[4]
(2704–2695 Ma)		Noranda Fm.	
		Reneault-Dufresnoy Fm.	
		Rouyn-Pelletier Fm.	
		Bousquet Fm.	Doyon-Bousquet-LaRonde and Cadillac areas (Mercier-Langevin et al., 2017a, b; Poulsen, 2017;
		Hébécourt Fm.	this paper)
	Kinojevis Group[5]		Matheson area (this paper)
	Malartic Group / Upper Malartic	Héva Fm.	Preissac Lake, Malartic, and Val-d’Or areas (De Souza et al., 2017; Houlé et al., 2017; Poulsen, 2017;
	Group/ Louvicourt Group[6]	Val-d'Or Fm.	this paper)
	Skead Group		
	Swayze Group	Brett Lake Fm.	Swayze area (this paper)
		Newton Fm.	
	Villebon Group		Val-d’Or area (Poulsen, 2017; this paper)
Tisdale	Larder Lake Group		Matachewan, Kirkland Lake, and Larder Lake areas (Poulsen, 2017; this paper)
(2710–2704 Ma)	Malartic Group[7]	Dubuisson Fm.	Preissac Lake, Malartic, and Val-d’Or areas (Houlé et al., 2017; Poulsen, 2017; this paper)
		Jacola Fm.	
	Tisdale Group	Central Fm.	Timmins area (Dubé et al., 2017; this paper)
		Gold Centre Fm.	
		Hersey Lake Fm.	
		Vipond Fm.	
	Trailbreaker Group	Heenan Fm.	Swayze area (this paper)
		October Lake Fm.	
Kidd-Munro	Kinojevis Group[5]	Lanaudière Fm.	Duparquet and Preissac Lake area (Houlé et al., 2017; this paper)
(2720–2710 Ma)	Malartic Group[7]	La Motte-Vassan Fm.	Preissac Lake area (Houlé et al., 2017; Poulsen, 2017; this paper)
	Unassigned	Kidd Creek Basalt fm.	Kidd Creek area (Hannington et al., 2017)
		Kidd Creek Rhyolite fm.	
		Kidd Creek Komatiite fm.	
Stoughton-Roquemaure	Catherine Group	Deguisier Fm.	Kirkland Lake area (this paper)
(2723–2720 Ma)	Kinojevis Group[5]		Duparquet and Preissac Lake areas (Houlé et al., 2017; this paper)
	Stoughton-Roquemaure Group		Duparquet area (this paper)
	Wawbewawa Group		Kirkland Lake area (this paper)
Deloro	Hunter Mine Group		Duparquet area (this paper)
(2734–2724 Ma)	Marion Group	Rush River Fm.	Swayze area (this paper)
		Strata Lake Fm.	
		Woman River Fm.	
Pacaud	Chester Group	Arbutus Fm.	Swayze area (this paper)
(2750–2735 Ma)		Yeo Fm.	

[1] Table only lists stratigraphic terms used in this volume

[2] Due to the absence of geochronological constraints, ultramafic and mafic volcanic rocks of the Piché Group are not assigned to a volcanic assemblage; volcanic rocks of the Piché Group represent the lithological expression of the Larder Lake-Cadillac fault zone and can be traced over a distance of about 250 km (Poulsen, 2017)

[3] Formally named formations are capitalized

[4] Stratigraphic assignment of the volcanic rocks of the Noranda camp is discussed by Monecke et al. (2017)

[5] The Kinojevis Group includes parts of the Stoughton-Roquemaure, Kidd-Munro, and Blake River assemblages; Ayer et al. (2005) introduced the term lower Blake River assemblage to allow distinction

[6] The Malartic Group was originally defined by Gunning and Ambrose (1940); Latulippe (1976) assigned volcanic rocks that form part of the Blake River assemblage to the Upper Malartic Group; following Scott et al. (2002), rocks of the Blake River assemblage are assigned to the Louvicourt Group; note that Poulsen (2017) in this volume uses the original stratigraphic nomenclature as established by Gunning and Ambrose (1940); in contrast, De Souza et al. (2017), Houlé et al. (2017), and this paper follow the nomenclature by Scott et al. (2002)

[7] The Malartic Group was originally defined by Gunning and Ambrose (1940); subsequent changes in nomenclature have been proposed by Scott et al. (2002) and are adapted here

The most recent and widely used naming convention for the volcanic stratigraphy of the AGB divides the belt into seven volcanic episodes, utilizing the ~500 geochronological constraints (U-Pb dates provided in Ayer et al., 2002b, 2005; Thurston et al. 2008) with large scale lithotectonic assemblages described by previous workers (Jackson and Fyon, 1991; Jackson et al., 1994).

However, most mining districts and regional areas have also developed their own local terminology for specific deposits. Although it is unwieldy, it is important to be able to translate between the volcanic assemblages and their local subdivisions as we study things at a variety of scales (Table 1). The seven volcanic episodes are as follows: Pre-2750 Ma volcanic unit(s) (>2750 Ma), Pacaud assemblage (2750-2735 Ma), Deloro assemblage (2734-2724 Ma), Stoughton-Roquemaure assemblage (2723-2720 Ma), Kidd-Munro assemblage (2719-2711 Ma), Tisdale assemblage (2710-2704 Ma), and the Blake River assemblage (2704-2695 Ma). Several of these assemblages have been subdivided into upper and lower members. The Kidd-Munro assemblage is divided into the lower Kidd-Munro (2719-2717 Ma) and the upper Kidd-Munro (2717-2711 Ma). The Tisdale assemblage is divided into the lower Tisdale (2710-2706 Ma) and the upper Tisdale (2706-2704 Ma). The Blake River assemblage is divided into the lower Blake River (2704-2701 Ma) and the upper Blake River (2701-2695 Ma) (Thurston et al., 2008).

The Tisdale assemblage outcrops extensively from the Kapuskasing structural zone to the west to the Larder Lake area in the east, mostly between the Porcupine-Destor and Cadillac-Larder Lake fault zones. In the Timmins area, the Tisdale is floored by a ~600m succession of komatiites and basaltic komatiites termed the Hersey Lake Formation. Overlying this is the Central Formation which is up to 450 m thick and composed mostly basalt with minor carbonaceous mudstone (Mason and Melnik, 1986; Bateman et al., 2008). The Vipond Formation is characterized by 200 – 300 m of distinctly spherulitic basalt flows. One of the flows in the Vipond Formation was dated and returned a zircon U-Pb age of 2706.9 ± 3.1 Ma (Ayer et al., 2002b). The youngest Tisdale volcanics in the area are a ~800 m thick succession called the Gold Centre Formation (Bateman et al., 2008; and references therein). In the eastern part of the Timmins mining camp, mafic and ultramafic volcanics with similar geochemical characteristics to those of the Hersey Lake and Central formations (but baring an age), are in contact with the younger sedimentary rocks of the Porcupine and Timiskaming assemblages (Bateman et al., 2008; Dinel et al., 2008b).

In Quebec, the Tisdale assemblage volcanics are present to the north of the Cadillac-Larder Lake fault zone, between Cadillac and Val-d'Or. They are divided into the Dubuisson and overlying Jacola formations, both part of the Malartic Group. The most recently revised stratigraphy is provided by Scott et al., 2002. The Dubuisson Formation is composed of intercalated komatiites and massive to pillowed basalt flows. The Jacola Formation consists of nonvesicular, massive to pillowed flows of mafic to ultramafic composition (Imreh, 1980). Komatiite units in the Jacola Formation reach thicknesses of 100 – 200 m. The top of the Jacola Formation has returned a U-Pb age of 2703.8 ± 1.2 Ma (Scott et al., 2002).

In the Swayze area, Tisdale aged rocks are present as the Trailbreaker Group (Table 1). The Trailbreaker group consists of mafic to intermediate volcanics of the October Lake Formation and overlying felsic to intermediate rocks of the Heenan Formation (Gemmell and McDonald, 2016). A Heenan Formation felsic volcanic was dated using zircon U-Pb and returned an age of 2705 ± 2 Ma (van Breemen et al., 2006).

The Blake River assemblage is the youngest of the six volcanically dominated episodes in the AGB. Most of the BR in the southern AGB is found between the Porcupine-Destor and Cadillac-Larder Lake fault zones, straddling the Ontario-Quebec border as an ellipsoidal volcanic mass. It is dominated by mafic volcanic rocks showing both massive and pillowed flow morphologies. Less than 5% of the outcrop area of the Blake River is intermediate to felsic in composition (Ayer et al. 2002b). It is host to approximately half of the polymetallic VMS tonnage, and about 90% of the VMS associated gold in the AGB (Mercier-Langevin et al., 2010c; Mercier-Langevin et al. 2011). In the Swayze area, BR volcanics were termed as the Swayze Group. The base of the Swayze Group is the Newton Formation, consisting of mafic to ultramafic flows and sills. Overlying the Newton Formation is the Brett Lake Formation, which is volcanic succession of felsic to intermediate flows and volcaniclastic rocks that were dated to have formed between 2699 $\pm^{3}_{2}$ Ma and 2695 ± 2 Ma (Cattell et al., 1984; van Breemen et al., 2006).

2.2 Sedimentary Successor Basins

Postdating the seven volcanic episodes, are two distinct sedimentary successor basins (Mueller and Donaldson, 1992b; Mueller and Corcoran, 1998). The ≤ ~2690 to ≤2685 Ma Porcupine assemblage is the first episode of sedimentation following submarine volcanism. In the southern AGB, the Porcupine assemblage is composed of deep marine passive margin sediments, consisting of greywacke and mudstones (Rocheleau, 1980; Lajoie and Ludden, 1984; Stone, 1990; Born, 1995). Locally the Porcupine assemblage includes minor calc-alkaline volcanic rocks (e.g., Krist Formation; Ayer et al. 2002b; MacDonald and Piercy, 2018). Following the deposition of the Porcupine assemblage, the Timiskaming assemblage was deposited from ≤2679 – 2669 Ma. The Timiskaming assemblage is characterized by the subaerial deposition of clastic molasse-like sediment, likely deposited during a time of orogenesis and are largely alluvial-fluvial conglomerate-sandstones, with some turbidites (Thurston et al., 2008). The occurrences of Timiskaming assemblage sedimentation preserved today are concentrated around the two major east trending faults in the AGB (Cadillac-Larder Lake Fault Zone, Porcupine-Destor Fault Zone). The concentration of sediments in these long-lived structures is likely due to graben formation during deposition of the Timiskaming assemblage, where the grabens acted as sedimentary basins for the sediment to accumulate. During subsequent compressive stress regimes, strain was accommodated by thick skinned reverse faulting along the major breaks. The Timiskaming assemblage that is seen today was likely trapped in the footwall block of these faults and protected from subsequent erosion by the hanging wall material above it (Monecke et al., 2017).

2.3 Swayze Area

The study area for this project is a package of suspected BR and younger volcanics spanning the central Swayze and south-central Dore townships. The Swayze area is likely the southwest extent of the AGB (van Breemen et al., 2006), and is bound by the Kapuskasing Structural Zone to the west and intruded by the large Kenogamissi batholith to the east, separating it from the western Abitibi (Figure 3). The Swayze area is dominated by mafic to felsic volcanic rocks with local punctuations of ultramafic volcanic rocks and clastic sedimentary successor basins. In the western AGB, the BR conformably overlays the Tisdale volcanic episode (Mercier-Langevin et al. 2011). The most voluminous portion of the BR rocks in the Swayze area is a bimodal succession of submarine volcanic – volcaniclastic rocks. These bimodal groups usually range from basaltic-andesite to dacite - rhyodacite dominantly calc-alkaline with local tholeiitic members. The study area has been overprinted by an east trending, steeply dipping foliation defined by sericite and chlorite. Destruction of primary volcanic textures is the result of local (~50m wide) localized high strain zones that parallel foliation, showing both sinistral and dextral kinematic indicators with significant iron carbonate alteration. These strain zones primarily occur at the interface between the two bimodal groups described above. There is a large synformal structure oriented roughly west-east spanning across the Swayze and Dore townships (and possibly beyond), with possible parasitic isoclinal folds that further complicate the stratigraphic interpretation of the area.

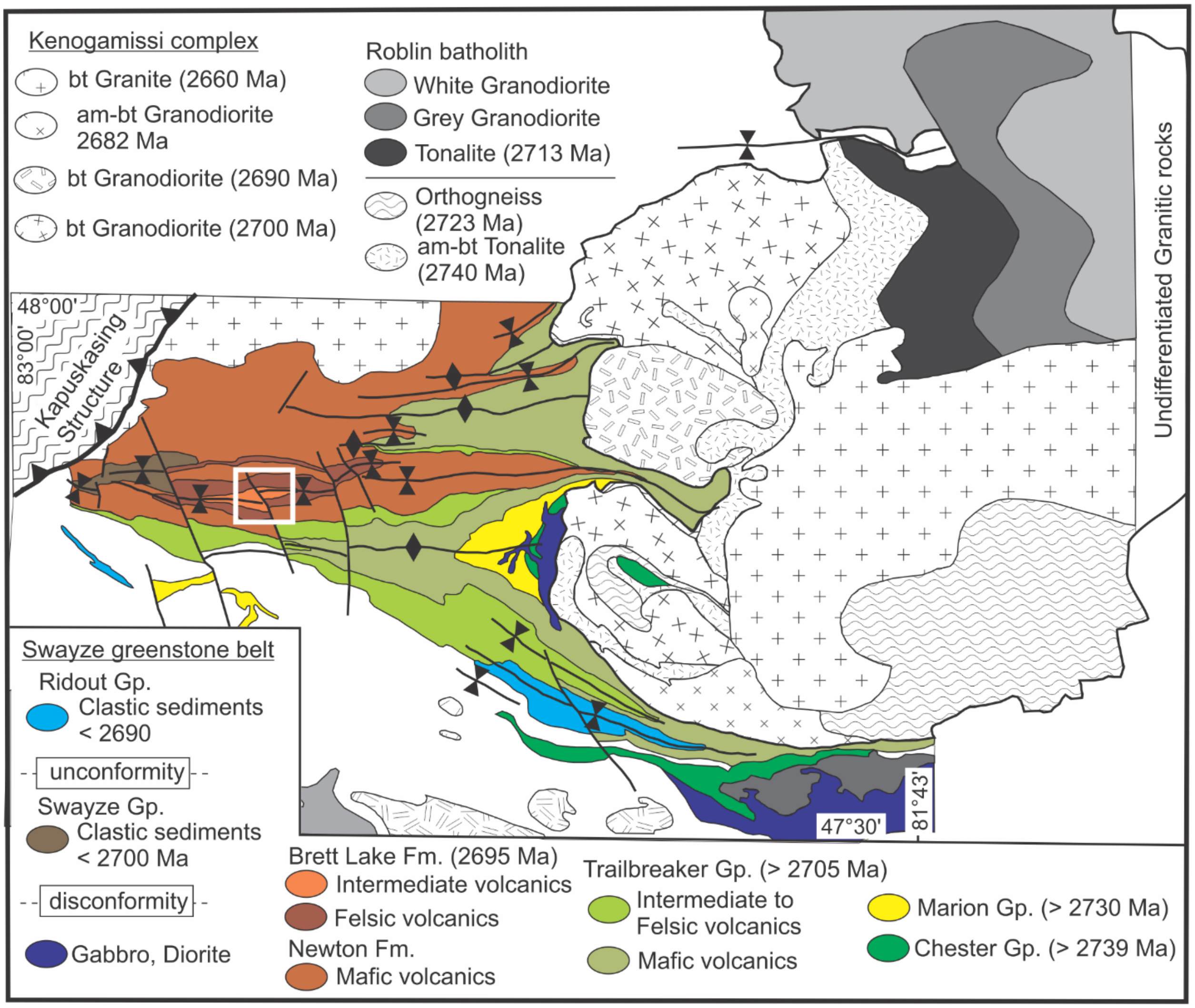

Figure 3: Map of the Swayze area showing a compilation of assemblage data based on mapping and geochronological data from Heather (1999) and Ayer et al. (2002b), with Kenogamissi complex internal contacts provided from mapping by Benn (2004). The study area location is indicated by a white box.

2.4 VMS deposits

Some of the most studied VMS deposits in world are found in BR rocks in the AGB and have been crucial in developing our understanding of Archean VMS systems. The BR in the AGB also hosts world class Au-rich VMS deposits (e.g., Horne, LaRonde-Penna, etc.), providing ample opportunity to study this style of VMS deposit. In general, VMS deposits consist of two ore components: a sulphide lens and a stockwork or stringer zone. The sulphide lenses are syngenetic, stratabound to locally discordant lens-shaped accumulations of massive to semi-massive sulphide that are usually hosted in volcanic rocks. These lenses are underlain by discordant stockworks of sulphide veins that are surrounded by alteration halos (Gibson et al., 2007; Dubé et al., 2007). These deposits form from the venting of metal laden hydrothermally circulated seawater at or near the seafloor. To produce such a deposit, several geological components need to be present. A shallow (3-10km), long lived (millions of years) heat source is necessary to produce and maintain a hydrothermal convection cell that can drive the ore forming system (Piercey, 2011). While it is possible that a single, large intrusion under favourable conditions can maintain a hydrothermal system for ~800kyrs (Cathles et al., 1997), they are usually the result of multiple pulses of intrusions. These are usually formed from the mafic-ultramafic underplating of thinned crust in an extensional environment. During underplating, crustal assimilation takes place which produces more evolved melts. The tectonic extension causes deeply penetrating (up to 10km) syntectonic-synvolcanic faults and fractures to form (Hart et al., 2004). These faults are crucial for increasing the structural permeability of the hanging wall rocks, which allows smaller, more felsic (typically tonalite-trondhjemite-granodiorite (TTG)) intrusions to ascend to higher levels; further increasing the geothermal gradient of the area (e.g., Mooshla Intrusive Complex, DBL, Galley and Lafrance, 2014; Flavarian Powell Intrusive Complex, Noranda, Gibson and Galley, 2007). Along these synvolcanic faults, evolved seawater is drawn down, heated by the increase in geothermal gradient caused by the intrusions, and then encouraged to migrate up through the overlying strata by convective forces. During this interaction with the overlying strata, the heated fluids leach metal ions from the rocks and are eventually vented to or near the seafloor near the spreading axis (Gibson et al., 2007). In terms of tectonic environment, there is a consensus that in order to emplace and maintain such a high-level heat source, an extensional environment, in the form of a mid-ocean ridge, volcanic arc, fore arc, back arc setting, or other volcanic subsidence structure is needed (Gibson et al., 2007). For example, in Noranda the Noranda Volcanic Complex (NVC) is thought to have formed as lavas and volcaniclastics filling in a submarine volcanic caldera. This caldera was floored by synvolcanic intrusions know as the Flavarian Powell Intrusive Complex (FPIC) (Gibson and Galley, 2007).

3.0 Methods

3.1 Field Mapping and Sampling

Mapping and sample collection took place between June and August 2022, as part of an Ontario Geological Survey (OGS) regional mapping project (NE-22-003), an initiative by the Mineral Exploration Research Center (MERC) and Metal Earth to understand the metallogenic evolution of the AGB. Geological mapping was conducted in the Swayze, Dore, and part of the Garnet townships in the southern Swayze area of the AGB. Information recorded included rock type, alteration, field relationships (contacts, etc.), primary textures, photographs, and structural measurements. Detailed outcropping mapping was conducted on specific outcrops to further understand the geological architecture of the area. For this study, 21 samples were taken, interpreted to be representative of the whole stratigraphy of the BR (upper and lower BR). Sampling avoided weathering, veining, and intense alteration. The amount of rock sampled ranged from 0.5 kg for representative geochemistry and petrography, to ~ 10 kg for zircon separates. In addition to representative rock samples from unmineralized outcrop, channel samples were also collected from a VMS-style massive sulphide lenses dominantly composed of pyrrhotite and pyrite in order to characterize the occurrence. From this VMS occurrence, ten samples were submitted for geochemistry and polished thin section preparation. Of these, eight samples were dominantly composed of massive sulphide and two were examples of the least altered rock at the occurrence, considered to represent the local host rock. Mapping data was recorded using Bedrock Pro on a Mesa 2 tablet and was uploaded onto an Arc GIS Pro project. This mapping data is being used for an ongoing PhD thesis and so it is not reported here.

3.2 Whole Rock Geochemistry

Portions of all 21 samples were sent for geochemical analysis to ALS Laboratories (Moncton, New Brunswick). Approximately 1 kg mass samples were pulverized in a jaw crusher such that 70% of the sample was reduced to < 2 mm fragment size. Further pulverization in a low Cr-steel bowl following riffle splitting of 250 g from this crushed material reduced grain size to 85% < 75 um. Aliquots of 0.1 to 2g (depending on method) from this pulverized material were analyzed by the following methods: (i) total carbon and sulfur by IR spectroscopy; (ii) lithium borate fusion followed four acid digestion and analysis of major, minor and trace elements (including super trace-level metals) by ICP-AES and ICP-MS. Detection limits and ranges (ppm unless otherwise indicated) for ALS ME-MS61L^{TM} package are as follows: Ag 0.002-100, Ce 0.01-500, Hf 0.004-500, Na 0.001%-10%, Sb 0.02-10000, Ti 0.001%-10%, Al 0.01%-50%, Co 0.005-10000, In 0.005-500, Nb 0.005-500, Sc 0.01-10000, Tl 0.002-10000, As 0.02-10000, Cr 0.3-10000, K 0.01%-10%, Ni 0.08-10000, Se 0.006-1000, U 0.01-10000, Ba 1-10000, Cs 0.01-500, La 0.005-10000, P 0.001%-1%, Sn 0.02-500, V 0.1-10000, Be 0.02-1000, Cu 0.02-10000, Li 0.2-10000, Pb 0.01-

10000, Sr 0.02-10000, W 0.008-10000, Bi 0.002-10000, Fe 0.002%-50%, Mg 0.01%-50%, Rb 0.02-10000, Ta 0.01-500, Y 0.01-500, Ca 0.01%-50%, Ga 0.05-10000, Mn 0.2-100000, Re 0.0004-50, Te 0.005-500, Zn 0.2-10000, Cd 0.005-1000, Ge 0.05-500, Mo 0.02-10000, S 0.01%-10%, Th 0.004-10000, Zr 0.1-500. Mineralized samples (n=10) were submitted separately and not all of the previously detailed methods were used, as priority was given to base, precious and accessory metals. The mineralized samples were analyzed using ALS' ME-OG46, Cu-OG46, and ME-MS41 procedures. The detection limits and ranges (ppm unless otherwise indicated) for ME-MS41 are as follows: Ag 0.01-100, Cs 0.05-500, Mo 0.05-10000, Sr 0.2-10000, Al 0.01-25%, Cu 0.2-10000, Na 0.01%-10%, Ta 0.01-500, As 0.1-10000, Fe 0.01%-50%, Nb 0.05-500, Te 0.01-500, Au* 0.02-25, Ga 0.05-10000, Ni 0.2-10000, Th 0.2-10000, B 10-10000, Ge 0.05-500, P 10-10000, Ti 0.005%-10%, Ba 10-10000 Hf 0.02-500, Pb 0.2-10000, Tl 0.02-10000, Be 0.05-1000, Hg 0.01-10000, Rb 0.1-10000, U 0.05-10000, Bi 0.01-10000, In 0.005-500, Re 0.001-50, V 1-10000, Ca 0.01%-25%, K 0.01%-10%, S 0.01%-10%, W 0.05-10000, Cd 0.01-1000, La 0.2-10000, Sb 0.05-10000, Y 0.05-500, Ce 0.02-500, Li 0.1-10000, Sc 0.1-10000, Zn 2-10000, Co 0.1-10000, Mg.01%-25%, Se 0.2-1000, Zr 0.5-500, Cr 1-10000, Mn 5-50000, Sn 0.2-500.

3.3 Petrography

Polished thin sections were prepared by Precision Petrographics (Vancouver, BC), to a thickness of 30 μm. Thin section petrography was carried out using Olympus BX41 and Nikon Eclipse 50i polarizing microscopes at Saint Mary's University. Major rock forming mineral phases in thin sections were identified via plane and cross polarized transmitted light. Mineralized sample petrography was performed using the same microscopes under reflected light.

3.4 Heavy mineral separation and mount preparation for zircon chemical analysis

Six of 21 samples were chosen, based on their position relative to the sub-economic VMS mineralization (above, below and stratigraphically equal to) and their propensity to host zircon (felsic composition, porphyritic texture, etc.), for zircon separation. Zircon separation and mounting, SEM-CL imaging of zircon mounts, and LA-ICPMS trace element analysis and U-Pb geochronology were all conducted at Boise State University's (BSU) Isotope Geology Laboratories according to their internal methods. Mineral separates were produced from ~10 kg samples (hand samples) at BSU. Following separation and picking of grains, the population of zircons from each sample was split into roughly equal proportions. Approximately half the grains were mounted in a non-annealed (unheated) state. The other half were dry annealed (heated) to 900°C and held at this temperature for 60 hours. This serves three purposes: (i) to improve the concordance of U-Pb geochronology dates (through enhancing the sensitivity of removal of Pb-loss affected domains during chemical abrasion); (ii) to enhance the CL luminescence response for imaging purposes; and (iii) to homogenize melt inclusions to a glass. The temperature of annealing was deemed to be sufficient to homogenize inclusions completely that were less than ~10-15 um in size for rhyolitic-trachytic-dacitic liquids. Of the 6 samples sent to BSU for zircon separation, 4 yielded enough zircons to be also analyzed by LA-ICP-MS (for trace elements and U-Pb dating), as well as Chemical Abrasion Isotope Dilution Thermal Ionization Mass Spectrometry (CA-ID-TIMS) U-Pb dating. Two archived pucks of mounted (non-annealed) zircons from rocks in the study area were obtained from the Geological Survey of Canada and sent to BSU for LA-ICP-MS and CA-ID-TIMS trace element analysis and U-Pb dating, respectively. Zircon SEM-CL imaging was conducted on a Hitachi TM 4000Plus using 20 nA current and 19 mm working distance. Following imaging, LA-ICPMS and CA-ID-TIMS geochronology occur at Boise State.

3.5 Laser ablation inductively coupled mass spectrometry (LA-ICP-MS)

Locations for LA-ICP-MS analyses were chosen using CL images of the annealed zircon grains. The CL images were used to identify xeno-, ante-, and autocrystic zones so that spots could be placed within each. Spots were chosen to avoid melt/mineral inclusions, as these showed different luminosities than the enclosing zircon. LA-ICP-MS spot locations were chosen to (i) compare trace element compositions of rim growth zones (autocrystic domains) and core growth zones (antecrystic domains) of zircon that may reflect changes in the geochemical evolution of magmas from which zircon grew; (ii) discriminate autocrystic and antecrystic domains from xenocrystic domains, providing an assessment of inheritance. These data and observations were also utilized to select grains for CA-ID-TIMS U-Pb dating and to avoid inheritance (using ^{206}Pb/^{238}U).

Zircon was analyzed by laser ablation inductively coupled plasma mass spectrometry (LA-ICPMS) using an iCAP RQ Quadrupole ICP-MS and Teledyne Photon Machines Analyte Excite+ 193 nm excimer laser ablation system with HelEx II Active two-volume ablation cell. In-house analytical protocols, standard materials, and data reduction software were used for acquisition and calibration of U-Pb dates and a suite of high field strength elements (HFSE) and rare earth elements (REE). Zircon was ablated with a laser spot of 15 µm wide using fluence and pulse rates of 2.5 J/cm^2 and 10 Hz, respectively, during a 25 second analysis (15 sec gas blank, 10 sec ablation) that excavated a pit ~8 µm deep. Ablated material was carried by a 0.25 L/min He gas stream in the inner cell and a 1.25 L/min He gas stream in the outer cell. Dwell times and other instrumental data are given in Table S1. Background count rates for each analyte were obtained prior to each spot analysis and subtracted from the raw count rate for each analyte. Ablations pits that appear to have intersected glass or mineral inclusions were identified based on Ti and P. U-Pb dates from these analyses are considered valid if the U-Pb ratios appear to have been unaffected by the inclusions. Analyses that appear contaminated by common Pb were rejected based on mass 204 being above baseline. For concentration calculations, background-subtracted count rates for each analyte were internally normalized to ^{29}Si and calibrated with respect to NIST SRM-610 and -612 glasses as the primary standards. Temperature was calculated from the Ti-in-zircon thermometer (Watson et al., 2006). Because there are no constraints on the activity of TiO_2, an average value in crustal rocks of 0.6 was used.

For U-Pb and ^{207}Pb/^{206}Pb dates, instrumental fractionation of the background-subtracted ratios was corrected and dates were calibrated with respect to interspersed measurements of zircon standards and reference materials. The primary standard FC1 zircon (Swanson-Hysell et al., 2021) was used to monitor time-dependent instrumental fractionation based on two analyses for every 14 analyses of unknown zircon. A secondary correction to the ^{206}Pb/^{238}U dates was made based on results from the zircon standards Plešovice zircon (337 Ma, Sláma et al., 2008) and 91500 (1065 Ma, Wiedenbeck et al., 1995), which were treated as unknowns and measured once for every 14 analyses of unknown zircon. These results (Table S3) showed a linear age bias of several percent that is related to the ^{206}Pb count rate. The secondary correction is thought to mitigate matrix-dependent variations due to contrasting compositions and ablation characteristics between the Plešovice zircon and other standards (and unknowns).

Radiogenic isotope ratio and age error propagation for all analyses includes uncertainty contributions from counting statistics and background subtraction. Errors without and with the standard calibration uncertainty are shown in the Table S2. This uncertainty is the local standard deviation of the polynomial fit to the interspersed primary standard measurements versus time for the time-dependent, relatively larger U/Pb fractionation factor, and the standard error of the mean of the consistently time-invariant and smaller ^{207}Pb/^{206}Pb fractionation factor. These uncertainties are given in Table S1. Age interpretations are based on ^{207}Pb/^{206}Pb dates. Analyses with discordance, defined as the relative difference between the ^{207}Pb/^{206}Pb and ^{206}Pb/^{238}U dates, outside of 10% were removed from Table S2. Errors are at 2σ.

3.6 Zircon SEM-BSE-EDS

The mounted zircon from the four samples collected for this project as well as the two archived GSC samples were examined under back scatter electron (BSE) imaging on a scanning electron microscope (SEM) at Saint Mary's University. This was done to search for melt and mineral inclusions exposed through polishing and to obtain BSE images of the individual zircon grains for study in an associated PhD project by Priyal Daya. Exposed inclusions were analysed using energy dispersive spectroscopy (EDS) on the SEM to obtain semiquantitative elemental abundances of the inclusions. Two types of BSE images were produced of each sample. Detailed slow scan speed images of individual melt and mineral inclusions and images of entire zircon grains using higher contrast to see variations zoning patterns that reflect fluctuations in trace elements.

3.7 Zircon U-Pb CA-ID-TIMS

High-precision chemical abrasion isotope dilution thermal ionization mass spectrometry (CA-ID-TIMS) was conducted at the Boise State University Isotope Geology Laboratory. U-Pb dates were obtained by CA-ID-TIMS analyses composed of single zircon grains (Data presented in Supplemental Materials Table 5; method modified after Mattinson, 2005). Zircon was removed from the epoxy mounts for dating based on CL images (e.g., lack of inherited cores, resorption surfaces, metamorphic overgrowths), LA-ICP-MS chemistry (e.g., magmatic REE patterns) and the attempt to better understand any differences in age between autocrystic and antecrystic domains, where possible.

Zircon was put into 3 ml Teflon PFA beakers and loaded into 300 μl Teflon PFA microcapsules. Fifteen microcapsules were placed in a large-capacity Parr vessel and the zircon partially dissolved in 120 μl of 29 M HF for 12 hours at 190°C. Zircon was returned to 3 ml Teflon PFA beakers, HF was removed, and zircon was immersed in 3.5 M HNO_3, ultrasonically cleaned for an hour, and fluxed on a hotplate at 80°C for an hour. The HNO_3 was removed and zircon was rinsed twice in ultrapure H_2O before being reloaded into the 300 μl Teflon PFA microcapsules (rinsed and fluxed in 6 M HCl during sonication and washing of the zircon) and spiked with the Boise State University mixed ^{233}U-^{235}U-^{205}Pb tracer solution (BSU-1B) or EARTHTIME mixed ^{233}U-^{235}U-^{202}Pb-^{205}Pb tracer solution (ET2535). Zircon was dissolved in Parr vessels in 120 μl of 29 M HF with a trace of 3.5 M HNO_3 at 220°C for 48 hours, dried to fluorides, and re-dissolved in 6 M HCl at 180°C overnight. U and Pb were separated from the zircon matrix using an HCl-based anion-exchange chromatographic procedure (Krogh, 1973), eluted together and dried with 2 μl of 0.05 N H_3PO_4.

Sample Pb and U were loaded on a single outgassed Re filament in 5 μl of a silica-gel/phosphoric acid mixture (Gerstenberger and Haase, 1997), and U and Pb isotopic measurements made on a GV Isoprobe-T multicollector thermal ionization mass spectrometer equipped with an ion-counting Daly detector. Pb isotopes were measured by peak-jumping all isotopes on the Daly detector for 160-240 cycles. Analyses spiked with BSU1B tracer solution were corrected for 0.18 ± 0.03%/a.m.u. (1σ) mass fractionation and analyses spiked with ET2535 tracer solution were corrected for mass fractionation using the known $^{202}Pb/^{205}Pb$ ratio of the tracer solution. Transitory isobaric interferences due to high-molecular weight organics, particularly on ^{204}Pb and ^{207}Pb, disappeared within approximately 60 cycles, while ionization efficiency averaged 10^4 cps/pg of each Pb isotope. Linearity (to $\geq 1.4 \times 10^6$ cps) and the associated deadtime correction of the Daly detector were monitored by repeated analyses of NBS982, and have been constant since installation. Uranium was analyzed as UO_2^+ ions in static Faraday mode on 10^{12} ohm resistors for 200-300 cycles, and corrected for isobaric interference of $^{233}U^{18}O^{16}O$ on $^{235}U^{16}O^{16}O$ with an $^{18}O/^{16}O$ of 0.00206. Ionization efficiency averaged 20 mV/ng of each U isotope. U mass fractionation was corrected using the known $^{233}U/^{235}U$ ratio of the tracer solution.

U-Pb dates and uncertainties were calculated using the algorithms of Schmitz and Schoene (2007), calibration of BSU-1B tracer solution of $^{235}U/^{205}Pb$ of 77.93, $^{233}U/^{235}U$ of 1.007066, and $^{205}Pb/^{204}Pb$ = 3491, calibration of ET2535 tracer solution (Condon et al., 2015) of $^{235}U/^{205}Pb$ = 100.233, $^{233}U/^{235}U$ = 0.99506, $^{205}Pb/^{204}Pb$ = 8474, and $^{202}Pb/^{205}Pb$ = 0.99924, U decay constants recommended by Jaffey et al. (1971), and $^{238}U/^{235}U$ of 137.818 (Hiess et al., 2012). $^{206}Pb/^{238}U$ ratios and dates were corrected for initial ^{230}Th disequilibrium using $D_{Th/U} = 0.20 \pm 0.05$ (1σ) and the algorithms of Crowley et al. (2007), resulting in an increase in the $^{206}Pb/^{238}U$ dates of ~0.09 Ma. All common Pb in analyses was attributed to laboratory blank and subtracted based on the measured laboratory Pb isotopic composition and associated uncertainty. U blanks are estimated at 0.013 pg.

Weighted mean $^{207}Pb/^{206}Pb$ dates are calculated from equivalent dates (probability of fit >0.05) using Isoplot 3.0 (Ludwig, 2003) with error at the 95% confidence interval. Error is computed as the internal standard deviation multiplied by the Student's t-distribution multiplier for a two-tailed 95% critical interval and n-1 degrees of freedom when the reduced chi-squared statistic, mean squared weighted deviation (MSWD) (Wendt and Carl, 1991), takes a value less than its expectation value plus its standard deviation at the same confidence interval, which is when MSWD is <1+2*sqrt[2/(n-1)]. This error is expanded via multiplication by the sqrt(MSWD) when the MSWD is $\geq 1+2*\mathrm{sqrt}[2/(n-1)]$ to accommodate unknown sources of over dispersion. Errors on the weighted mean dates are given as ± x / y, where x is the internal error based on analytical uncertainties only, including counting statistics, subtraction of tracer solution, and blank and initial common Pb subtraction, and y includes the ^{238}U decay constant uncertainty (Jaffey et al., 1971) propagated in quadrature. Internal errors should be considered when comparing our dates with other U-Pb dates. Errors including uncertainties in the ^{238}U decay constant should be considered when comparing our dates with those derived from other decay schemes (e.g., ^{40}Ar/^{39}Ar, ^{187}Re-^{187}Os). Errors on dates from individual analyses are 2σ.

3.8 Micro-XRF analysis of mineralized samples

Quantification of data for elemental abundances from the XRF data used standardless fundamental parameters (Barker et. al., 2021) to calculate concentrations from peak intensities. Micro-XRF geochemical maps for this study were produced on a Bruker Tornado µXRF scanner using a Rh X-ray tube with a spot size of 20 µm, 50 kV acceleration voltage and a 300 µA anode current at the Mineral Imaging and Analysis Laboratory at Saint Mary's University. Quantitative geochemical results were derived through the Bruker M4 software. For mineral identification, individual objects were manually selected from produced geochemical maps based on X-ray spectra, where new wt% values were generated based on the area selected. These objects wt% compositions were compared to known characteristics and elemental compositions of minerals allowing for best-match mineral classification. Findings from the µXRF were validated through petrographic microscopy.

4.0 Results

4.1 Field relationships

The field mapping conducted for this study aimed to develop a more detailed understanding of the distribution and character of suspected BR rocks in the Swayze area. A diverse range of rock types were identified within the study area, ranging from felsic to ultramafic in composition. Felsic rocks include fragmental and massive rhyodacite flows, felsic lapilli tuffs, lapilli stone and tuff breccias. Most of the rhyodacites and dacites had porphyritic texture, usually with phaneritic plagioclase phenocrysts, sometimes also with quartz eyes/phenocrysts.

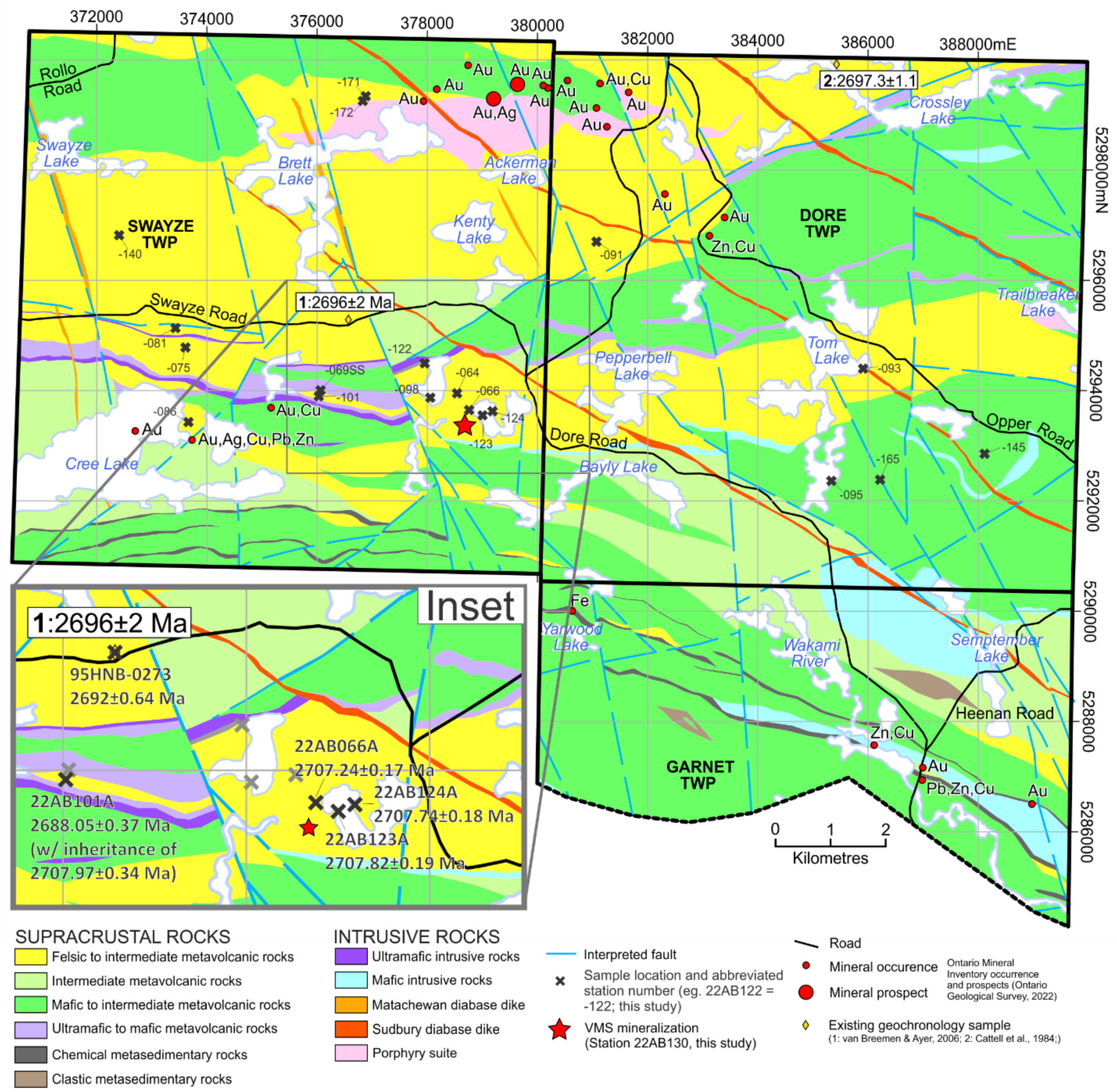

Figure 4: Lithological map of the study area showing the locations of samples taken for this study, previous U-Pb dates and the locations of previously reported mineral occurrences (including the VMS mineralization discussed in this study). Modified from Gemmell and Buyers (2022). Ontario Mineral Inventory (OMI) occurrences and prospects (Ontario Geological Survey, 2022) indicate documented primary commodities. Abbreviations used: Ag, silver; Au, gold; Cu, copper; Fe, iron; Pb, lead; VMS, volcanogenic massive sulphide; Zn, zinc. Location information provided as UTM co-ordinates using NAD83 in Zone 17.

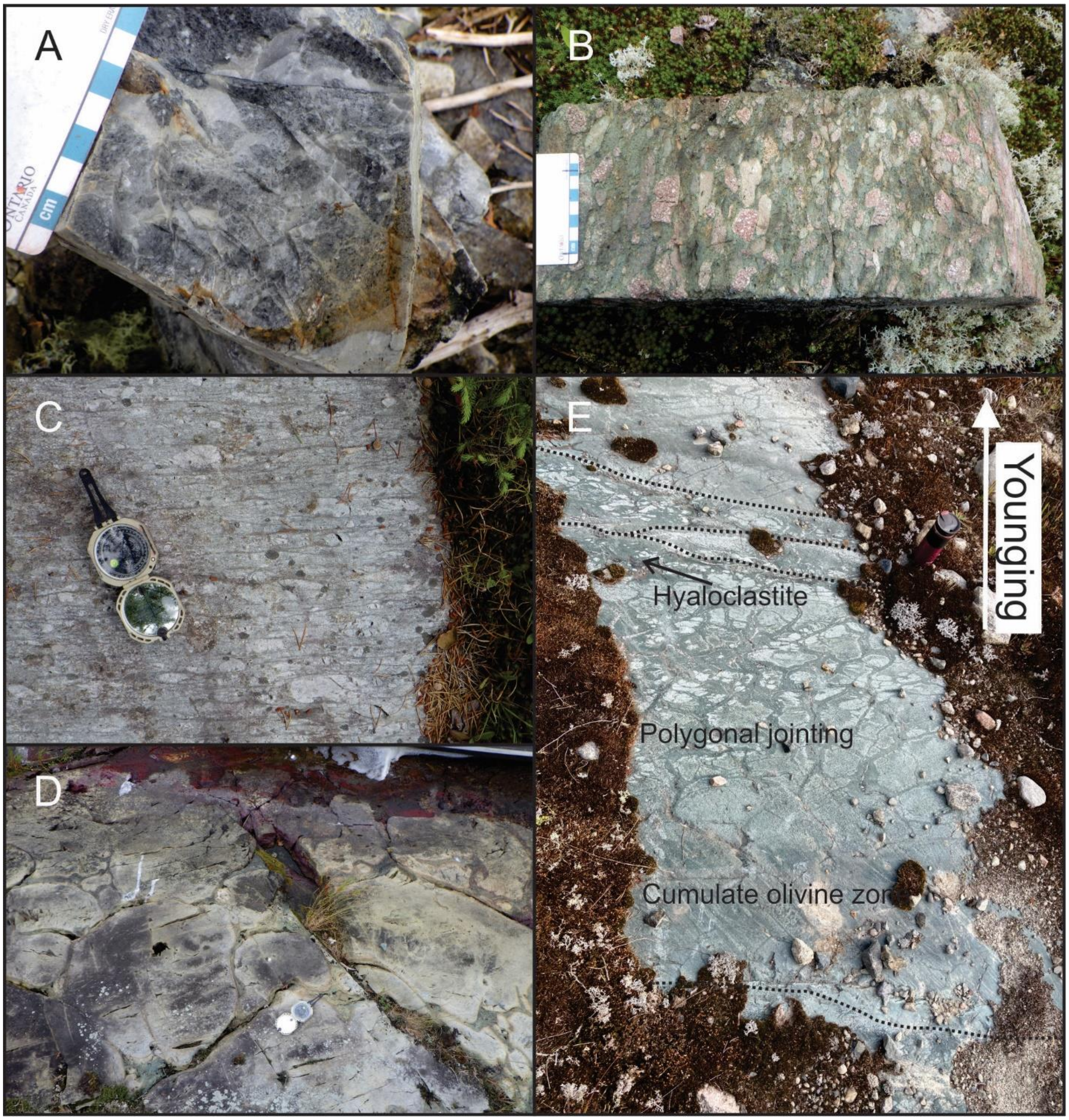

Figure 5: Photographs of select outcrops observed in the field. A) Fragmental, silicified rhyodacite (22AB098A). B) Andesitic heterolithic lapilli tuff to tuff breccia (22AB075A). C) Andesitic tuff breccia (22AB058A). D) Well preserved pillow basalt. Younging direction is towards the top of the page (22AB095A). E) Komatiite flows showing different facies. Dotted lines indicate interpreted tops/bottoms of flows. Coffee thermos to the right is approximately 25cm tall and 5 cm wide (22AB235SS).

Figure 5A exemplifies the texture and variable composition of many of the felsic volcaniclastic rocks mapped in the area surrounding the sub-economic VMS occurrence in the southern felsic package (Figure 4). The textures of the felsic to intermediate rocks, such as predominance of porphyritic texture, and lack of exposed contacts, made identifying intrusive or extrusive origin impossible at many outcrops. Intermediate rocks occurred mostly as fragmental flows, lapilli tuffs, and lapilli stone or tuff breccias. One easily distinguishable unit that was identified south of, and roughly parallel to, Swayze Road (Figure 4) was an intermediate lapilli tuff to tuff breccia with heterolithic clasts, characterized by distinct pink porphyritic lapilli and bomb sized components (Figure 5B). Large outcrops of monotonous monolithic intermediate tuff breccias were revealed north of Swayze Road (Figure 5C). Most of the mafic rocks encountered were in regions with little temporal control via U-Pb geochronology, and so their locations within the volcanic stratigraphy are purely relative. The mafic volcanic rocks were exclusively aphanitic and equigranular, and consisted of massive to pillowed lava flows; they are located within the green areas in Figure 4. Pillows selvages were often well preserved and allowed for confident younging directions to be identified from their morphology (Figure 5D and station -095 on Figure 4). Intrusive mafic rocks were encountered within the study area mostly in the south-central part of the Dore township (light blue, Figure 4); however, they were not sampled for this study. There was also a substantial amount of ultramafic volcanic rocks (komatiites) observed, some of which were not identified by previous mapping. The outcrops of komatiites occasionally preserved evidence of multiple flows with characteristic intra-flow vertical facies that allowed for younging directions/tops of flows to be interpreted from them (Figure 5E). Within, and proximal to, the mapping area there is a pattern of opposing younging directions and repetition of units that suggest a large syncline spans across the study area. The fold has axial traces striking approximately west and contain parasitic folds within their limbs.

4.2 Optical Petrography

Petrographic observations generally complimented and confirmed those made in the field. Felsic rocks dominantly show fragmental flow, volcanic breccia or pyroclastic textures, with the exception of sample 22AB101A (Figure 6B), which is a massive quartz-phyric rhyolite. Felsic fragmental flows are dominated by plagioclase and quartz, and their modal mineralogy suggests they are rhyodacitic to dacitic. Often, as seen in Figure 6A, the region in a sample interpreted to be the “clast” and the region interpreted to be the “matrix”, or groundmass, were of very similar composition. The distinction between them was made due to subtle textural differences between the two regions like the habit of the plagioclase phenocrysts, or the grainsize of the surrounding rock. However, the host-matrix boundary was often quite diffuse and the two regions appear to have thoroughly mixed together.

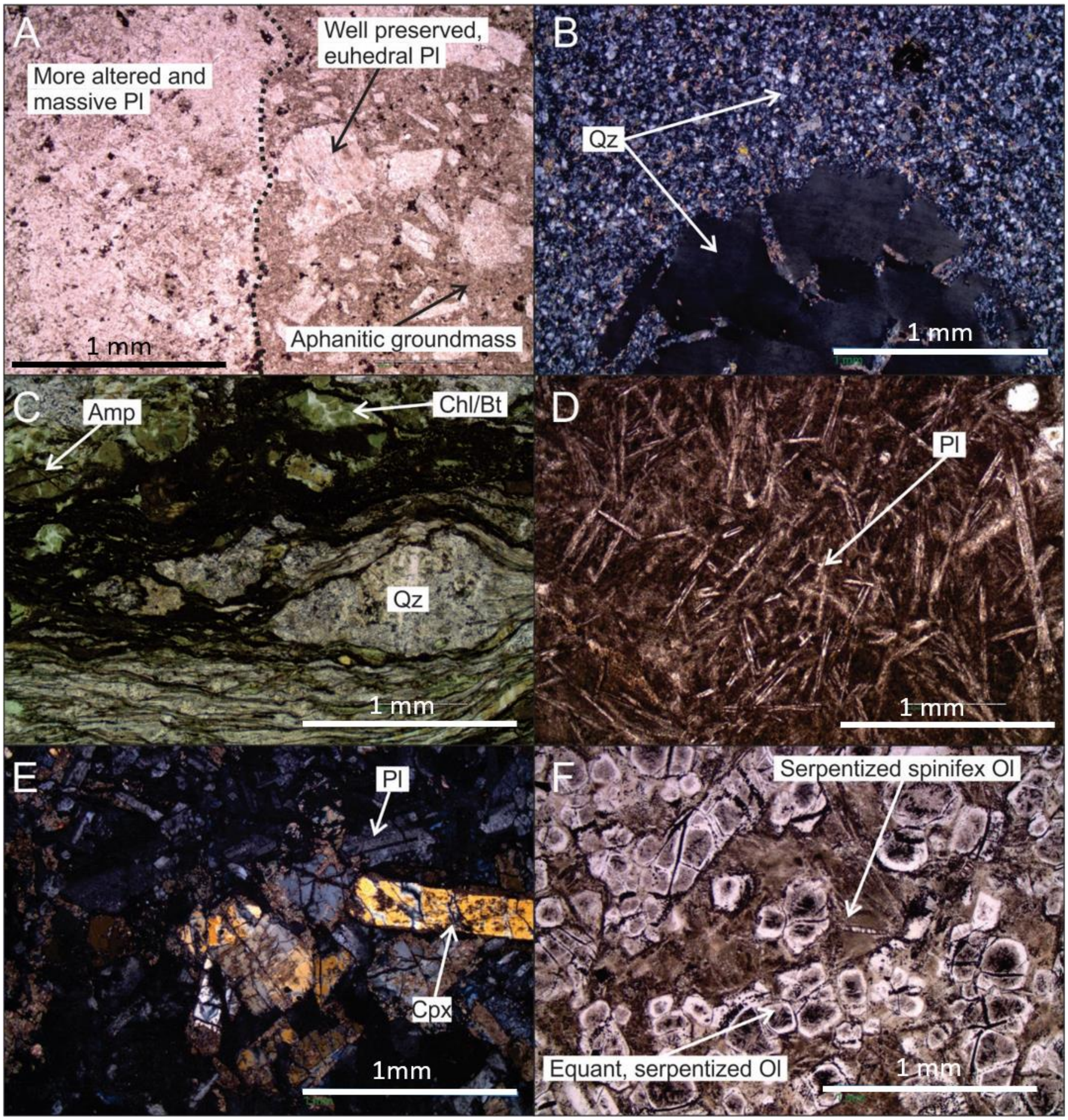
A
More altered and massive Pl
Well preserved, euhedral Pl
Aphanitic groundmass
1 mm
B
Qz
1 mm
C
Amp
Chl/Bt
Qz
1 mm
D
Pl
1 mm
E
Pl
Cpx
1mm
F
Serpentized spinifex Ol
Equant, serpentized Ol
1 mm

Figure 6 (previous page): Photomicrographs of selected samples under 4x magnification. A) Fragmental rhyodacite. "Clast" and "matrix" are roughly the same composition but have different textures (22AB098A). B) Massive Quartz-plagioclase-pyric rhyolite (22AB101A). C) Intermediate lapilli tuff-tuff breccia. Well developed bedding/foliation (22AB075A). D) Randomly oriented, acicular plagioclase crystals in a basalt (22AB095A). E) Basalt composed of well-formed plagioclase and clinopyroxene crystals (22AB145A). F) Komatiite sample from the base of a large flow. Equant olivine crystals occurring as glomerocrysts with spinifex textured olivine in between glomerocrysts. Nearly all olivine has been altered to serpentine (22AB069SS). Abbreviations used: Pl = plagioclase, Qz = quartz, Amp = amphibole, Chl = chlorite, Bt = biotite, Cpx = clinopyroxene, Ol = olivine (Whitney and Evans, 2010).

Intermediate rocks are characterized by a relatively lower proportion of quartz and a higher proportion of secondary chlorite/biotite and minor minerals like amphibole (Figure 6C). Intermediate tuffs show well defined foliation with quartz-plagioclase-rich lapilli occasionally becoming boudinaged (e.g., 22AB075A). Mafic intrusive rocks are dominated by plagioclase and clinopyroxene (Figure 6E), and often show subophitic-ophitic texture. Mafic volcanic rocks (e.g., 22AB095A; Figure 5D), sometimes show high undercooling textures like acicular plagioclase (Figure 6D). A komatiite sample taken for this study was obtained from the cumulate zone at the base of a flow (station -066SS, Figure 4). Equant olivine crystals dominate the rock, with spinifex textured olivine occurring in interstitial spaces between olivine glomerocrysts (Figure 6F). Nearly all of the olivine was altered to serpentine. All sampled lithologies are characterized by the alteration of primary mineral phases to chlorite and sericite. Late carbonate precipitation was also observed in most samples, usually occupying pore spaces between crystals. More detailed petrographic descriptions of each sample can be viewed in the Supplemental Materials (Table 3).

In thin section, accessory minerals like zircon and rutile were relatively rare. The zircon crystals able to be identified in thin section were between 200 μm and 400 μm in length and were usually hosted in quartz. (Figure 7A). Rutile crystals were rarely larger than ~25 μm and were dominantly hosted in quartz (Figure 7B).

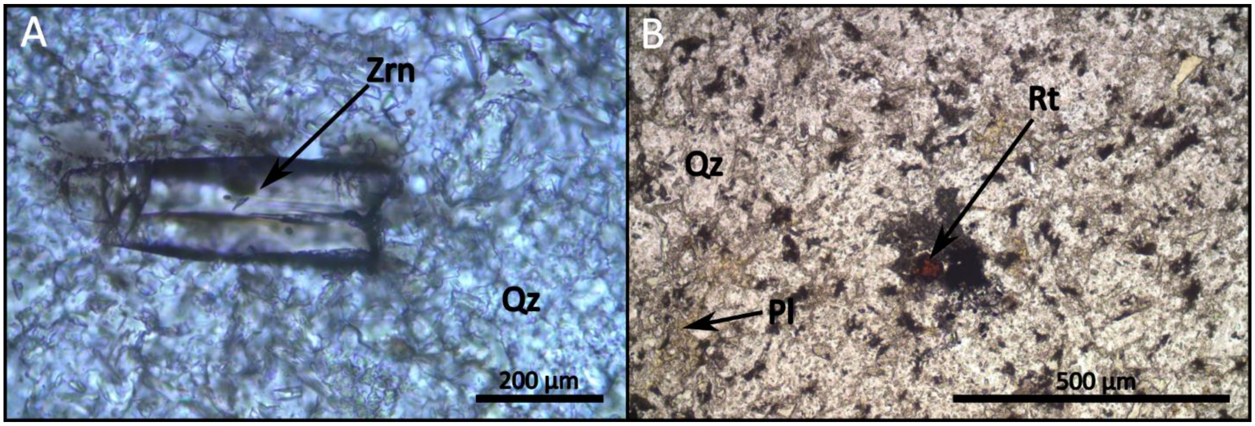

Figure 7: Accessory minerals seen under transmitted PPL. A) Zircon crystal hosted in fine grained quartz, under 40x magnification (22AB123A02). B) Rutile crystal hosted in quartz and plagioclase groundmass, under 4X magnification (22AB066A). Abbreviations used: Zrn = zircon, Qz = quartz, Rt = rutile, Pl = plagioclase.

4.3 Whole Rock Geochemistry

The whole rock geochemistry is generally consistent with the determinations of rock type in the field. The total alkali vs silica (TAS; Le Ma Maître et al., 1989) plot confirmed that most of the felsic rocks are dacitic in composition (Figure 8A). However, as Na, K, and SiO_2 are mobile during cooling and can be artificially skewed by weathering and low temperature alteration this diagram must be applied with caution. For example, it was suspicious that sample 22AB075A was plotting as a trachyandesite while the rest of the samples had much less total alkali metals, prompting different element proxies to rock type to be explored. Comparing elements that are not typically mobile (e.g. HFSE and REE), produced a more reliable categorization of the samples. This plot (Figure 8B; Winchester and Floyd, 1977), showed that all of the felsic rocks (called rhyolite or dacite based on field observations), were in fact rhyodacitic to dacitic in composition. The Nb/Y vs Zr/TiO_2 plot showed that sample 22AB075A plots as an andesite, not a trachyandesite.

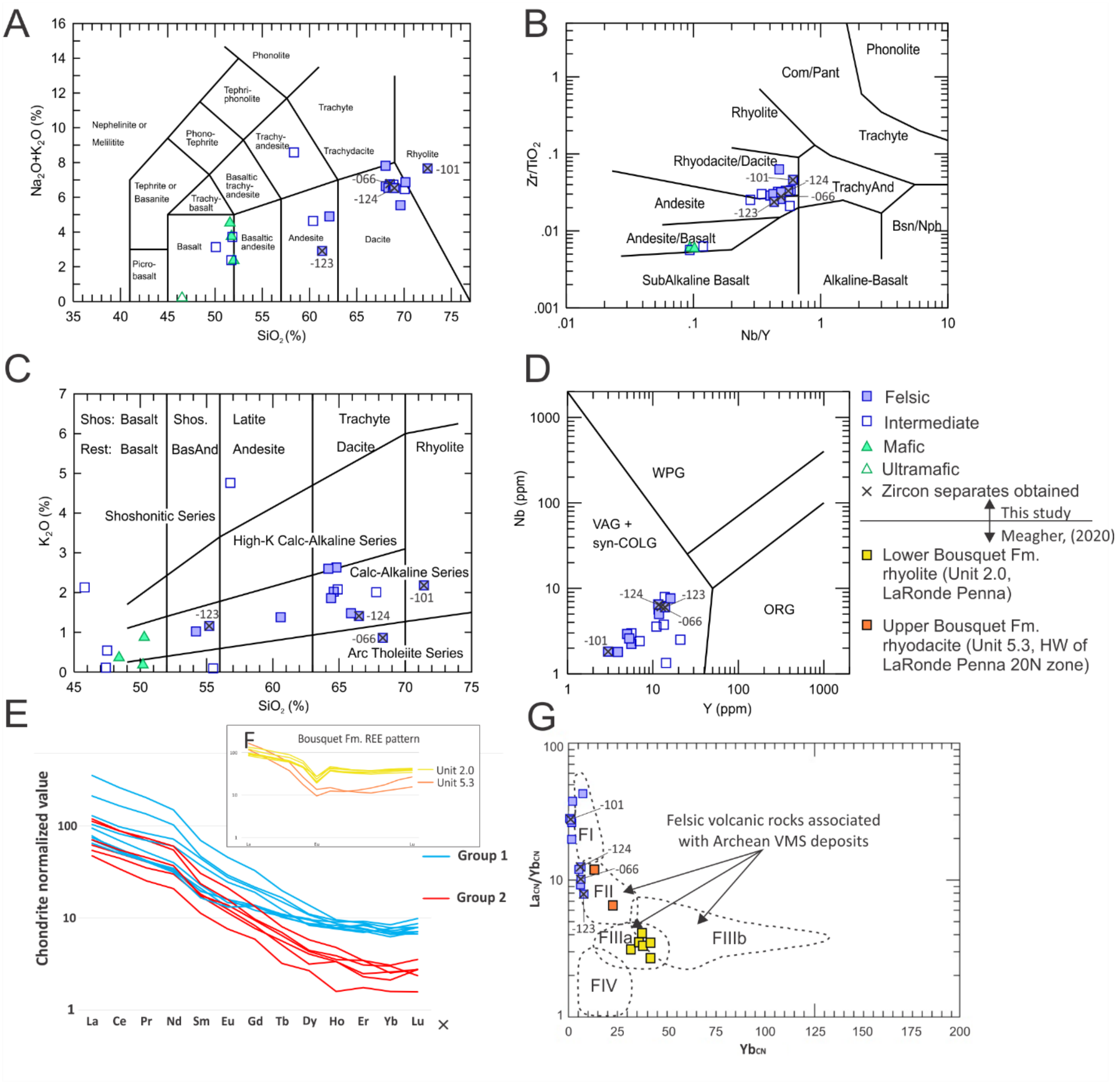
A
Na2O+K2O (%)
SiO2 (%)
Nephelinite or Melilitite
Tephrite or Basanite
Picro-basalt
Basalt
Phono-Tephrite
Tephri-phonolite
Phonolite
Trachy-basalt
Basaltic trachy-andesite
Basaltic andesite
Trachy-andesite
Andesite
Trachyte
Trachydacite
Dacite
Rhyolite
-101
-066
-124
-123
B
Zr/TiO2
Nb/Y
Phonolite
Com/Pant
Rhyolite
Trachyte
Rhyodacite/Dacite
TrachyAnd
Andesite
Andesite/Basalt
Bsn/Nph
SubAlkaline Basalt
Alkaline-Basalt
C
K2O (%)
SiO2 (%)
Shos: Basalt
Rest: Basalt
Shos.
BasAnd
Latite
Andesite
Trachyte
Dacite
Rhyolite
Shoshonitic Series
High-K Calc-Alkaline Series
Calc-Alkaline Series
Arc Tholeiite Series
D
Nb (ppm)
Y (ppm)
WPG
VAG + syn-COLG
ORG
Felsic
Intermediate
Mafic
Ultramafic
Zircon separates obtained
This study
Meagher, (2020)
Lower Bousquet Fm. rhyolite (Unit 2.0, LaRonde Penna)
Upper Bousquet Fm. rhyodacite (Unit 5.3, HW of LaRonde Penna 20N zone)
E
Chondrite normalized value
La Ce Pr Nd Sm Eu Gd Tb Dy Ho Er Yb Lu
Group 1
Group 2
F
Bousquet Fm. REE pattern
Unit 2.0
Unit 5.3
G
LaCN/YbCN
YbCN
Felsic volcanic rocks associated with Archean VMS deposits
FI
FII
FIIIa
FIIIb
FIV

Figure 8 (previous page): Geochemical plots produced from data obtained during this study, with reference geochemistry of productive VMS regions shown as yellow and orange squares from Meagher (2020). Legend showing the composition of the rocks as determined in the field and which samples zircon separates were obtained from. A) SiO_2% vs total alkali metals (Na_2O + K_2O%) (TAS) plot showing all samples taken for this study and their location within geochemical composition fields defined by Le Maître et al. (1989). B) Nb/Y vs Zr/TiO_2 plot with compositional fields from Winchester and Floyd (1977), showing all samples taken for this study. C) SiO_2% vs K_2O% showing the alkalinity and level of evolution of all samples taken for this study. Fields defined by Peccerillo and Taylor (1976). D) Y (ppm) vs Nb (ppm) granite discrimination diagram with the felsic and intermediate samples taken for this study plotted. Boundaries provided by and diagram developed by Pearce et al. (1984). E) Spider plot showing all samples REE contents (normalized to carbonaceous chondrite values provided by Sun and McDonough 1989). Two groupings of samples emerged, denoted as Group 1 and Group 2 and symbolized in blue and red, respectively. F) (Fig. E inset) REE spider plots of reference data of samples taken from two rhyolites from the LaRonde-Penna Au-rich VMS deposit (see legend for details) Normalized to same values as Fig. E. G) Yb_{CN} vs La_{CN}/Yb_{CN} VMS-associated rhyolite discrimination plot of all felsic volcanic rocks sampled for this study and reference material from aforementioned rhyolites; normalization values from Sun and McDonough 1989. Discrimination fields shown by dotted lines were defined by Hart et al. (2004) after Lesher et al. (1986).

Most of the samples plot within the calc-alkaline series, except 22AB075A that plots within the shoshonitic series (Figure 8C; Peccerillo and Taylor 1976). Felsic samples all plot within the volcanic arc granite and syn-collisional granite field on a tectonic setting discrimination plot (Figure 8D; Pearce et al. 1984). The chondrite-normalized rare earth element (REE) patterns seen in the felsic and selected intermediate rocks is shown in Figure 8E. Two groupings with varying levels of HREE depletion and LREE concentration emerged from this plot and are detailed in Table 2. There is a significant amount of spread and overlap in each group's LREE concentrations; however, in general Group 1 has higher LREE concentrations. Group 1 has La_{CN} values ranging from 64 to 351, while Group 2 has La_{CN} values ranging from 47 to 118. Group 1 has higher HREE concentrations; both group's range of values between samples are relatively small. Group 1 has Lu_{CN} values ranging from 6.7 to 9.8, while Group 2 has Lu_{CN} values ranging from 1.6 to 3.5. Group 1 and Group 2 have very similar La_{CN}/Lu_{CN} ratios, at 13.7 and 13.9, respectively. All samples lack Eu-anomaly and are strongly depleted in heavy REE (HREE), creating steep negative slopes (LREE>HREE).

Table 2: Selected felsic and intermediate samples belonging to each REE pattern group.

Sample	Group	LA-ICP-MS & CA-ID-TIMS	Rock Type (Winchester and Floyd 1977)	Alkalinity (Peccerillo and Taylor 1976
22AB066A	1	x	Rhyodacite/dacite	Arc tholeiite, dacite
22AB075A	1		Andesite	Latite, andesite
22AB081A	1		Andesite-Rhyodacite/dacite	Arc-tholeiite, basaltic andesite
22AB081B	2		Rhyodacite/dacite	Calc-alkaline, dacite
22AB086A	1		Rhyodacite/dacite	High-K calc-alkaline, dacite
22AB091A	2		Rhyodacite/dacite	Calc-alkaline, dacite
22AB093A	1		Rhyodacite/dacite	Calc-alkaline, basalt
22AB098A	1		Rhyodacite/dacite	Calc-alkaline, andesite
22AB101A	2	x	Rhyodacite/dacite	Calc-alkaline, rhyolite
22AB123A	1	x	Rhyodacite/dacite	Calc-alkaline, basaltic andesite
22AB124A	1	x	Rhyodacite/dacite	Calc-alkaline, dacite
22AB134A	2		Rhyodacite/dacite	Calc-alkaline, dacite
22AB135A	2		Rhyodacite/dacite	Calc-alkaline, dacite
22AB140A	1		Andesite/Basalt	Shoshonitic basalt
22AB171A	2		Rhyodacite/dacite	High-K calc-alkaline, dacite

4.4 VMS Mineralization

A sub-economic VMS occurrence was identified and added to the Ontario Mineral Inventory (OMI) in 2017 the OGS. The exposed area of massive sulphide has an apparent lateral extent of approximately 35 m and a width of approximately 10 m. The occurrence is dominantly comprised of massive to semi-massive pyrrhotite with variable disseminated euhedral pyrite. It contains regions that show preserved wall rock fragments with progressive replacement by sulphide mineralization. The host rock is a fragmental-brecciated, porphyritic rhyodacite. The top 5-10 cm of exposed rock is weathered to hematite and hydrous iron oxide minerals (i.e., goethite; Figure 9A).

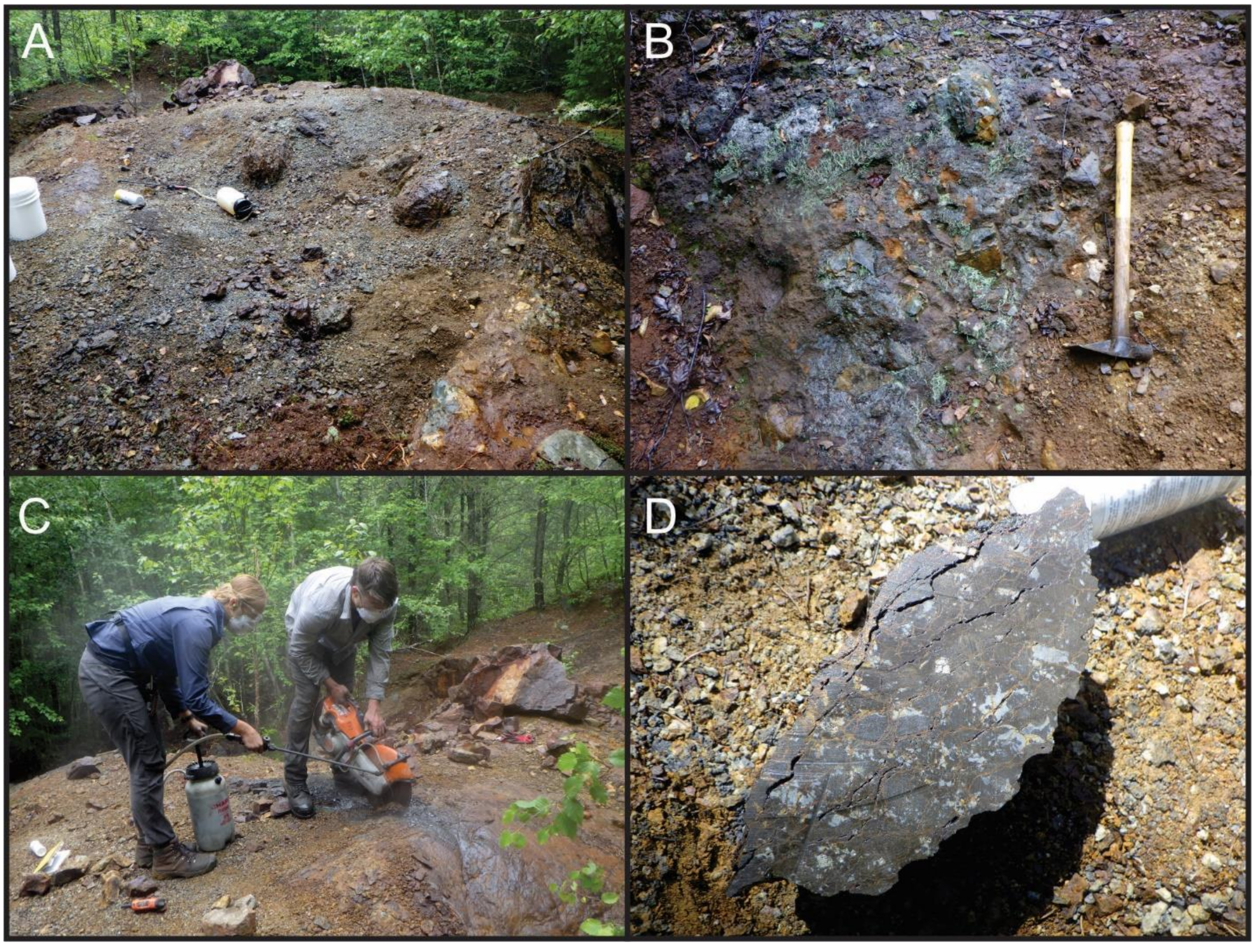

Figure 9: Photos taken in the field of the sub-economic VMS occurrence by the author during sampling (2022). A) Overview of the appearance of the massive sulphide occurrence at surface. Typical 20 gal bucket to the left of image for scale. B) Gossanous veneer composed of regolithic clasts cemented by iron (hydro)oxides. Geo-tool handle is approximately 50 cm. C) The author (right) and field assistant Emilia Butty (left) taking a channel sample of massive sulphide. D) Offcut of massive sulphide sample showing typical appearance of pyrrhotite-dominated mineralized material. Bug repellent in the top-right of the image is approximately 15 cm long.

There are areas within the clearing where sulphide minerals are absent and the host rock has been altered to a light-coloured beige-grey at the surface; likely dominated by sericite and quartz (Figure 10B). The eastern clearing has a blast pit with a length, width and depth of approximately 5 m x 5 m x 1.5 m from exploration activity in the 1980's. Near the base of the pit the massive sulphide abruptly changes to relatively fresh, unmineralized and massive host rock. Around the edges of the clearing, a gossanous veneer covers the massive sulphide and is composed of fragments of rock cemented together by iron oxides (Figure 9B).

A total of 27 variably mineralized channel samples were taken at the occurrence. These sample locations were chosen to capture lateral and (interpreted) vertical textural and chemical variations across the occurrence. Ten of these samples were sent for geochemistry and thin section preparation. They include: (i) three samples that represent a stratigraphic cross section through the lens (22AB130A03, -05, 08), (ii) two of host rock (one from the blast pit (22AB130A16), one from the edge of the occurrence (22AB130A01)), (iii) two dominated by pyrite (22AB130A23, -24), and three others dominated by pyrrhotite spread laterally across the occurrence (22AB130A10, -20, -27) (See figure 10A for sample locations).

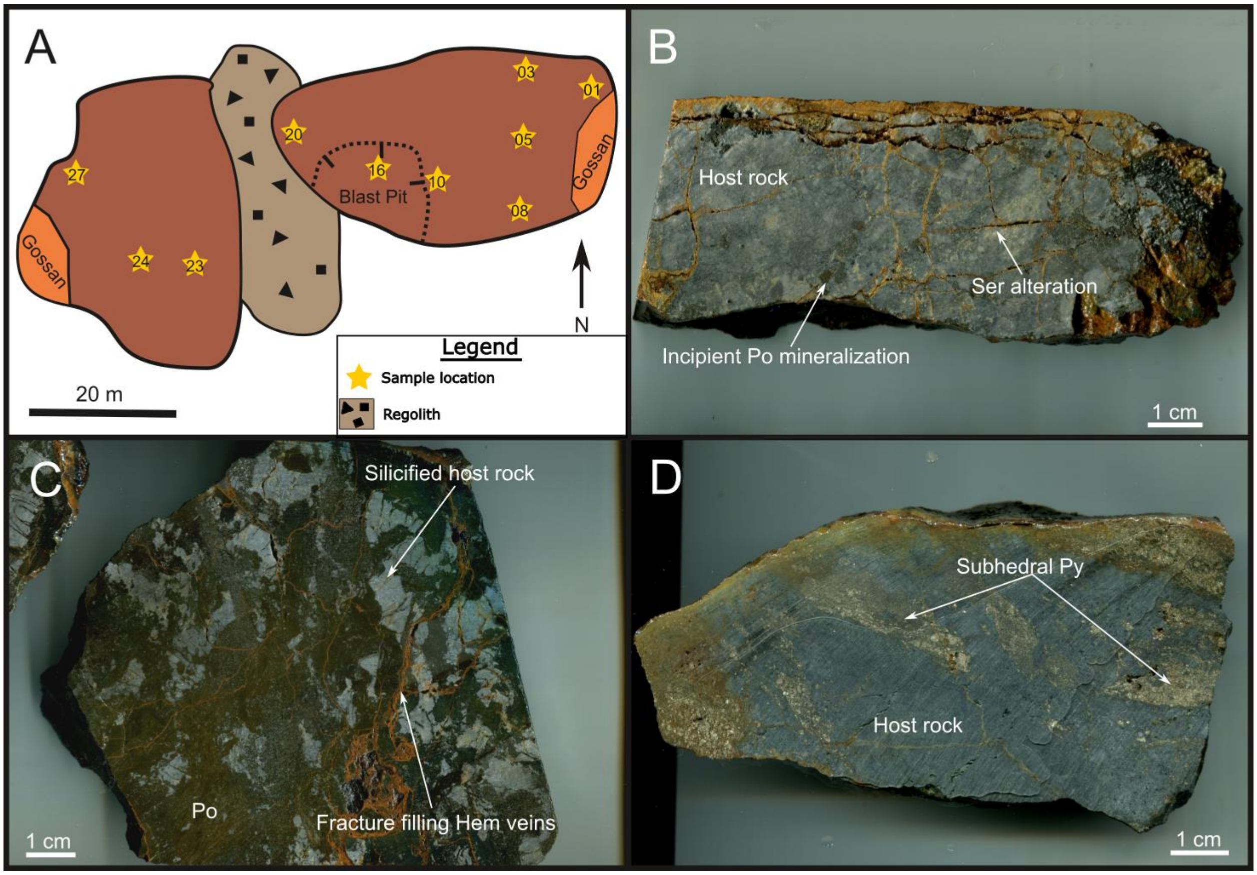

Figure 10: A) Diagram of the massive sulphide clearing showing sample locations as yellow stars and sample number suffix (e.g., 22AB130A05 = 05). B) Sample showing incipient pyrrhotite mineralization within well preserved host rock (22AB130A01). C) Example of pyrrhotite-dominated massive sulphide deposited within brecciated, silicified host rock (22AB130A05). D) Pyrite-dominated sample preserving host rock (22AB130A23). Abbreviations used: Po = pyrrhotite, Ser = sericite, Hem = hematite, Py = pyrite.

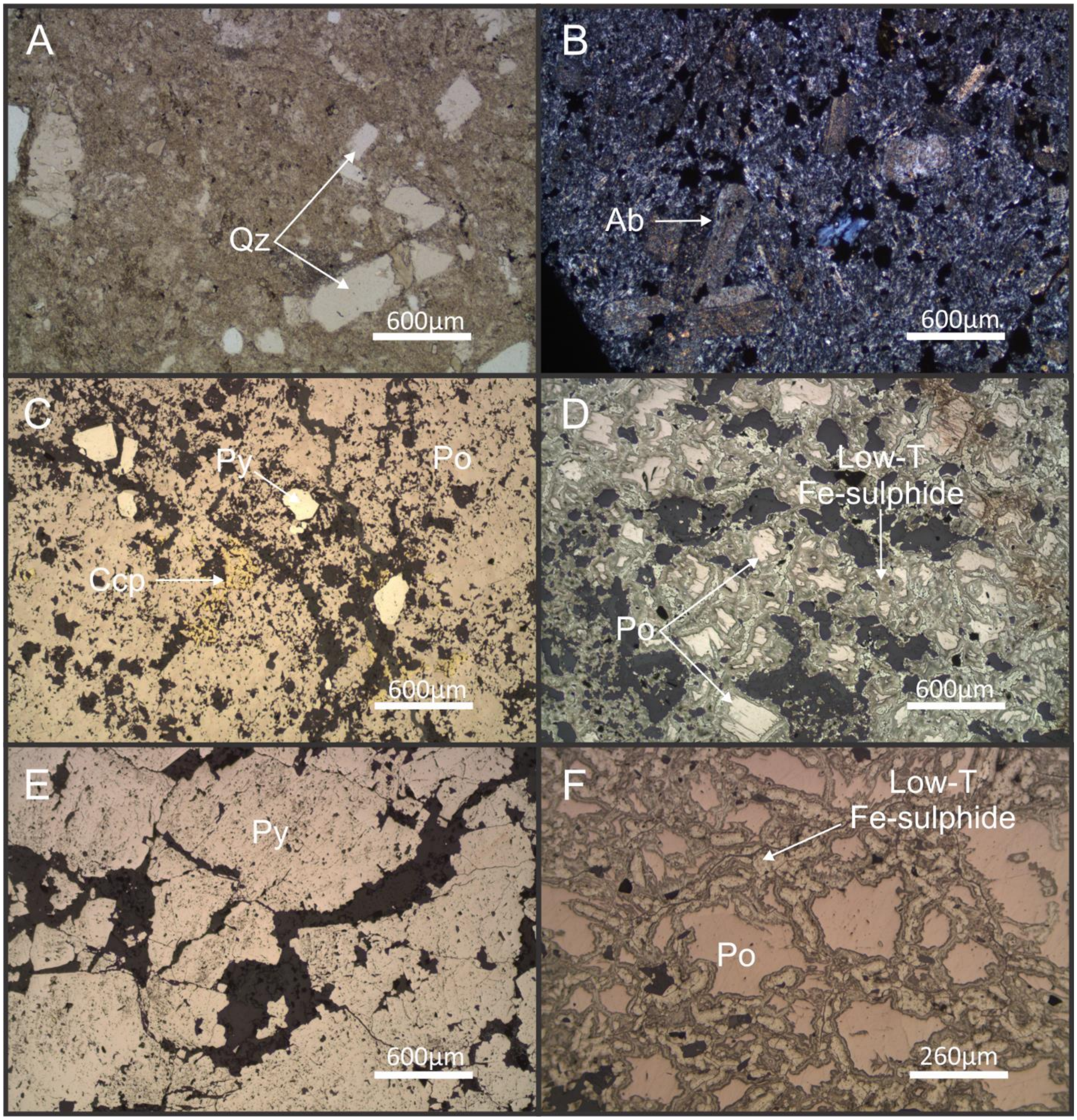

Figure 11: Photomicrographs of mineralized samples from station 22AB130. A) Transmitted PPL image under 4x magnification of host rock sample 22AB130A16. B) Transmitted XPL image under 4x magnification of host rock sample 22AB130A01. C) Reflected light PPL image under 4x magnification of pyrrhotite-dominated sample 22AB130A03 showing disseminated pyrite and minor chalcopyrite phase. D) Reflected PPL image under 4x magnification of pyrrhotite-dominated sample 22AB130A08 showing unknown secondary Fe-sulphide mineral. E) Reflected PPL image under 4x magnification of massive, pyrite-dominated sample 22AB130A24. F) Reflected PPL image under 10x magnification showing texture of the secondary unknown Fe-sulphide mineral being produced from pyrrhotite (22AB130A27). Abbreviations used: Py = pyrite, Po = pyrrhotite, Ccp = chalcopyrite, Ab = albite.

The thin section of 22AB016 (Figure 11A) was composed of irregular shaped quartz phenocrysts in a fine-grained quartz-albite groundmass. Sample 22AB130A01 is similar, but has albite phenocrysts and is more sericitized (Figure 11B). Both of these samples of host rock are fragmental rocks, so it is possible that the thin sections were taken from slightly different regions within the same rhyodacitic flow. Sample 22AB130A03 (Figure 11C), is dominated by pyrrhotite showing massive replacement textures. Less abundant phases of subhedral pyrite occurs within the pyrrhotite dominated areas, and small inclusions of chalcopyrite were observed within the pyrrhotite. Sample 22AB130A24 (Figure 11E) is an example of the massive, blocky texture seen in areas dominated by pyrite. Most of the samples consisted of massive pyrrhotite with occasional disseminated pyrite (Figures 11E, 11F). Pyrrhotite appears to have nearly replaced all the host rock in these samples. In many areas it was sub-sequentially altered to an unknown, pale beige-brown, low temperature iron sulphide. Sphalerite was difficult to positively identify as instances of it were small and rare, however, the geochemistry of the samples suggest that it is present (Table 4a in Supplemental Materials). Small (≤1 mm) veins of suspected iron oxides cut through previous textures in all massive sulphide samples and have colloform texture when viewed in reflected, cross-polarized light.

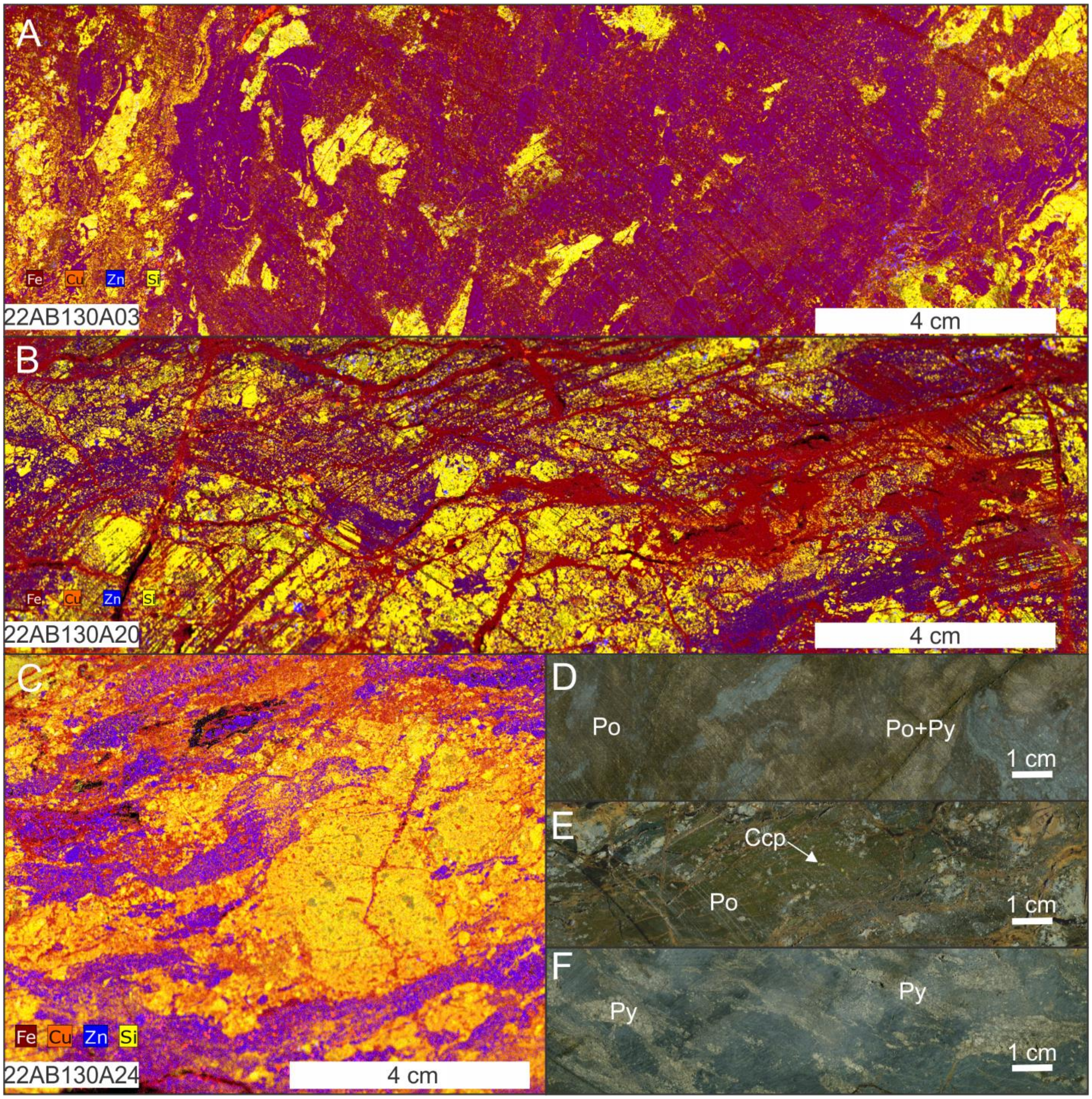

Figure 12: Mineralized samples from sub-economic VMS occurrence (22AB130). Images A, B, and C are µXRF false colour elemental maps with the colours representing each element shown in the bottom left. Images D, E, and F are scans of the mineralized samples. A) Sample 22AB130A03. B) Sample 22AB130A20. C) 22AB130A24. D) Sample 22AB130A03. E) Sample 22AB130A20. F) 22AB130A24. Abbreviations used: Po = pyrrhotite, Py = pyrite, Ccp = chalcopyrite.

The mineralized sample's relatively barren whole rock geochemistry supports the lack of ore minerals identified in thin section. Cu concentrations ranged from 77.8 ppm to 651 ppm, with a mean of 286.58 ppm. Zn ranged from 53 ppm to 2300 ppm, with a mean of 375.9 ppm. Surprisingly, the highest Zn contents (2300 ppm) were found in the host rock sample 22AB130A16, although no Zn-sulphide minerals could be identified in thin section. Not including this sample, the highest Zn content is only 365 ppm, giving a mean Zn-content in the samples of 162.1 ppm. Pb contents ranged from 2.7 ppm to 24.7 ppm, with a mean of 14.01 ppm. The concentration of Au was at or below the detection limit for all samples (Au detection limit: 0.02 ppm). Silver concentration ranged from 0.67 ppm to 5.04 ppm with a mean of 2.69 ppm.

4.5 Zircon Textural Interpretations

The samples taken for this study that were sent for zircon separation were chosen in a way so that their age might effectively provide a date for the VMS occurrence, as well as to obtain absolute ages for a part of the study area with little temporal control, from previous studies. Images of the four samples taken for this study are shown below (Figure 13).

CL images of annealed and non-annealed zircons allow observations of growth zoning patterns to be made. The textural characteristics of zircon can be used to aid in the determination of whether a zircon was inherited from an older rock or different magmatic system; or grew in the magma chamber which produced the rock it is hosted in (Corfu et al., 2003). Two types of inherited zircon which may record vastly different U-Pb ages and trace element chemistries are restitic and xenocrystic zircon. Restitic zircon are crystals which grew in the deep crustal magma source region and were not destroyed during their ascent with the magma (Jeon and Williams, 2018). Xenocrystic zircon are crystals derived from the assimilation of wall rock material into the magmatic plumbing system (Kemp et al., 2005; Johnson, 1989). Discrimination between these two types of inherited crystals is beyond the scope of this study. However, identification of inherited whole crystal or zircon cores is made based on CL textures and LA-ICP-MS trace element analyses. Inherited zircon can be expected to show different textural characteristics and trace element concentrations than zircon genetically related to the melt/rock they are found in. Antecrystic zircon or antecrystic zones, are crystals/zones which grew before the final crystallization phase but are still part of the same magmatic system (Smithies et al., 2015). They can often be identified by instances of resorption or interruption to the concentric zones before and after them.

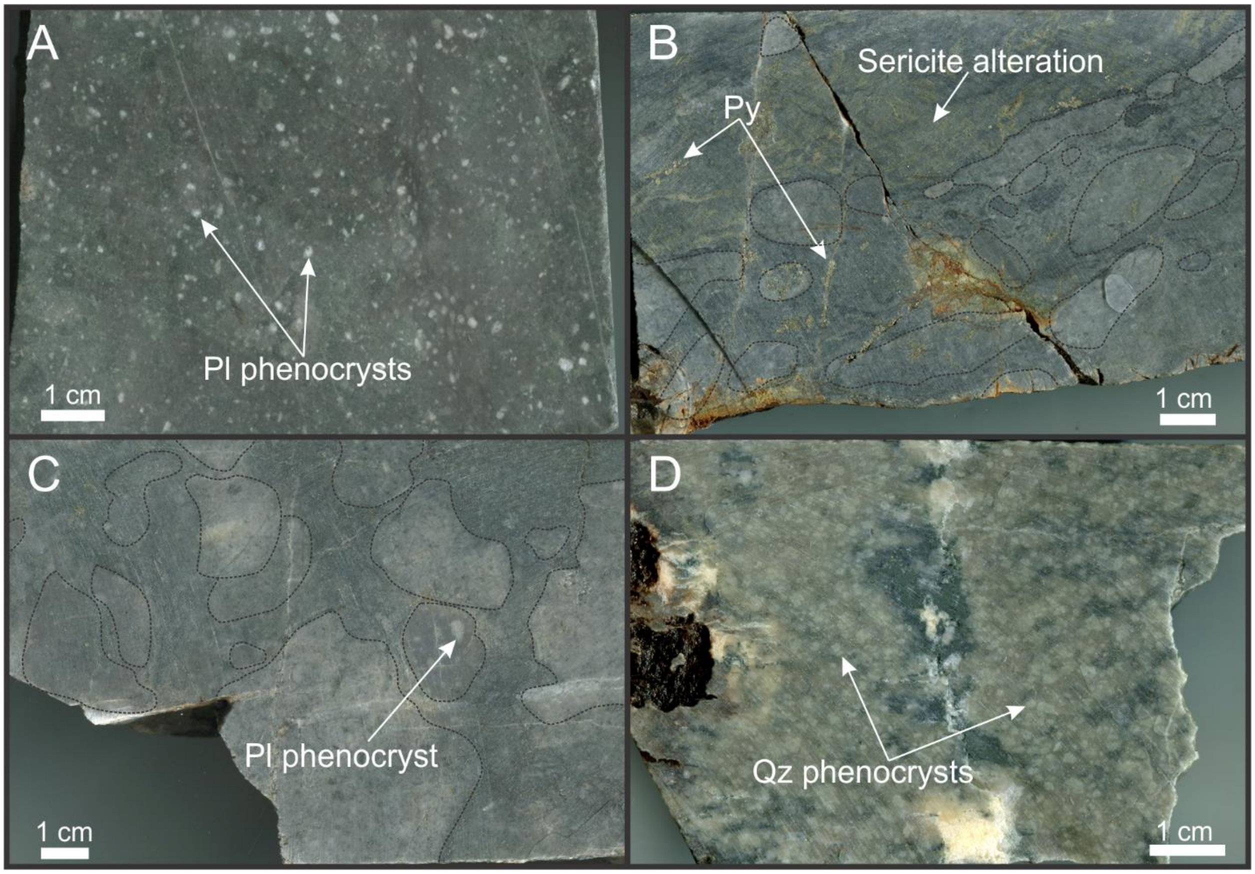

Figure 13: Scans of the rocks from which zircon separates were obtained for this study. Dotted lines highlight interpreted fragments A) Sample 22AB066A. B) Sample 22AB123A. C) Sample 22AB124A. D) Sample 22AB101A. Abbreviations used: Pl = plagioclase, Py = pyrite, Qz = quartz.

Autocrystic zircon or zones of zircon are those which grew in the final crystallization phase of the magmatic body that produced the resulting rock. They are characterized by uninterrupted growth and regular zoning patterns.

Zircon from samples 22AB066A, 22AB123A, 22AB124A all show oscillatory zoning throughout their growth history, usually with one or two antecrystic domains between the core and final autocrystic rim (Figures 14A, C, D). Zircon from sample 22AB101A contains a variety of different luminosities between individual crystals (Figure 14B). Faint oscillatory zoning is characteristic of most core regions, as well as making up the entirety of some grains. However, some crystals have a low-luminescent, irregular, massive to sector zoning overgrowth on the rim of the zircon. This is a first indication that the zircon population in this rock is of heterogenous origin. Sample 93HNB-206B (outside of the study area and scope of the study), contains examples of much brighter (CL) core domains that are likely inherited and originated from an older magmatic system (Figure 14E). Zircon from sample 95HNB-273 (a previously dated tuff, Figure 4 geochronology location 1), show luminescent, oscillatory growth zoning with one to two antecrystic zones, similar to that seen in samples 22AB066A, 22AB123A, and 22AB124A. Although the zircon crystals are generally smaller. Many of the zircon in all samples contain inclusions within them that were exposed (by polishing), to the surface and imaged for a future melt inclusion study.

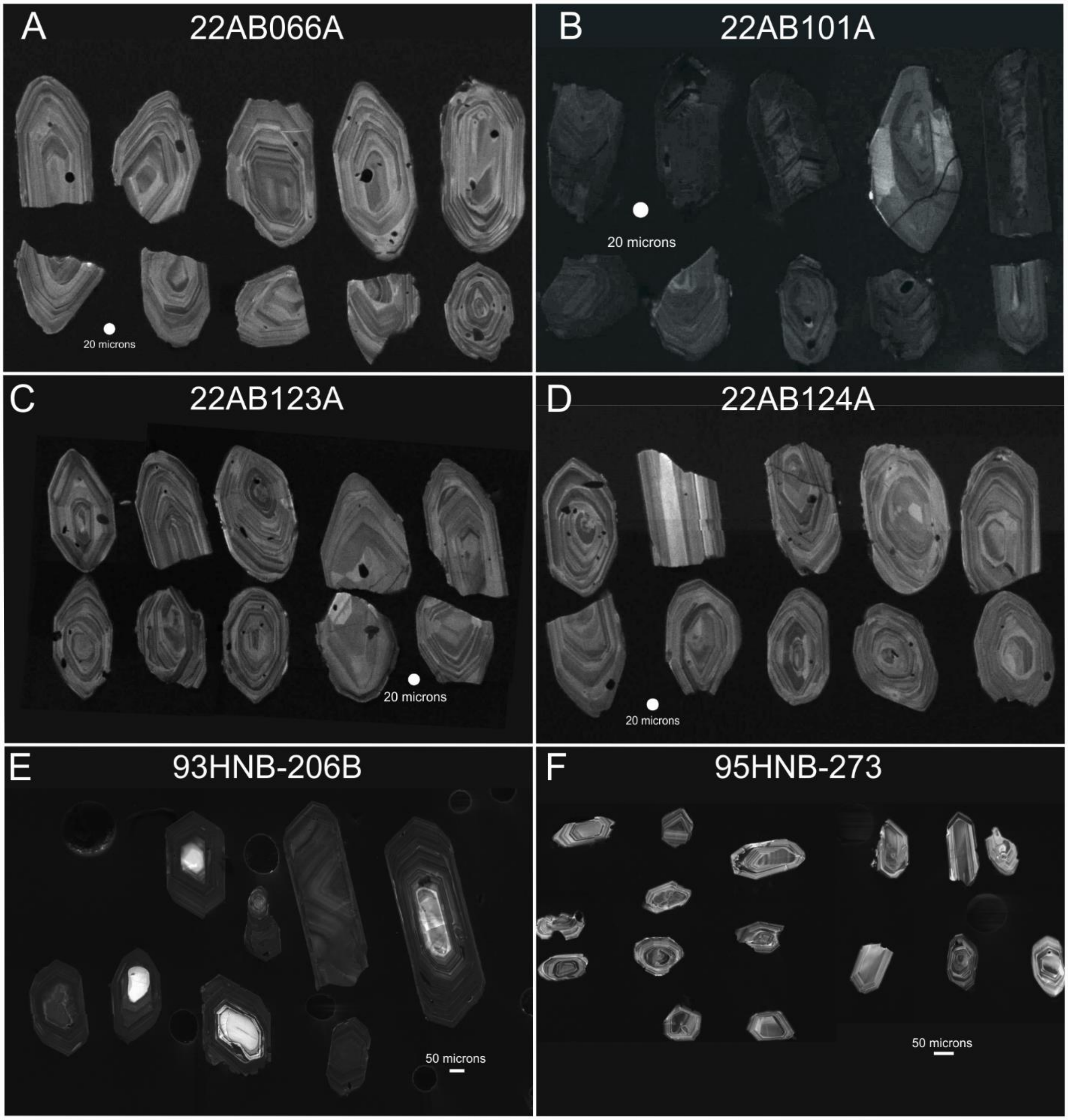

Figure 14: CL images of portions of the annealed mounted zircons from each sample in this study (except 93HNB-206B). Sample locations can be seen in Figure 4. A) Zircon obtained from sample 22AB066A, which is a fragmental-autoclastic dacite-andesite flow. B) Zircon obtained from sample 22AB101A, which is a massive Qz-phyric rhyolite. C) Zircon obtained from sample 22AB123A, which is a fragmental rhyodacite-dacite flow/volcaniclastic. D) Zircon obtained from sample 22AB124A, which is a fragmental rhyodacite-dacite flow/volcaniclastic. E) Zircon obtained from outside the study area from sample 93HNB-206B, which is a quartz-feldspar porphyry. F) Zircon obtained from sample 95HNB-273, which is a felsic ash-crystal tuff. Previously reported geochronology data and descriptions of samples 93HNB-206B and 95HNB-273 can be referenced in van Breemen et al. (2006).

4.6 Zircon Trace Element Data

Zircon from five samples within the study area were obtained and their chemistry analyzed for trace elements by LA-ICP-MS. Three of these samples were taken in close proximity to each other and are located in the southern felsic volcanic package near the sub-economic VMS (Figure 4: -066, -123, and -124). These samples all came from rocks that showed REE patterns in Group 1 (Figure 8E). They were all obtained from fragmental felsic-intermediate flows/volcaniclastic rocks (Figure 13A, B, C). One sample was obtained from a massive Qz-phyric rhyolite within a fault block that has little temporal control (Figure 4: -101; Figure 6B; Figure 13D). This samples whole rock REE geochemistry placed it in Group 2 (Figure 8E). The last sample of zircon was obtained from a felsic tuff by previous workers (Heather, 2001; with further analyses in van Breemen et al., 2006), located in the northern felsic volcanic package (Figure 4, geochron location 1). Other rocks sampled for this study near where this sample was taken exhibited REE patterns of Group 2. For reference to rhyolites associated with VMS, trace element data from zircon obtained from rhyolites of the tholeiitic Lower Bousquet Formation (Unit 2.0) and calc-alkaline Upper Bousquet Formation (Unit 5.3) will be plotted alongside our data (unpublished data, Daya, 2023).

Interpretations from the CL images of the zircon in samples 22AB066A, 22AB123A, 22AB124A, and 95HNB-273 (Figure 14A, C, D, and F), and accompanying U-Pb geochronology (CA-ID-TIMS and LA-ICP-MS, Supplemental Material Tables 5 and 6) indicates a lack of inheritance in the studied zircon fractions. The interpretation of CL images and U-Pb geochronology of sample 22AB101A indicate that inheritance is likely. Analyses in the following plots are grouped based on the textural domains recognized in CL images and assigned to each individual spot analysis (i.e., all antecrystic domains are grouped and all autocrystic domains are grouped). Overall, there is overlap between antecrystic and autocrystic domains. This is not surprising since zircon grains would have been growing at different stages, and thus, antecrystic and autocrystic domains should not show a sharp boundary compositionally. However, as we will discuss further, distinct elemental groupings can be identified in 22AB101A.

The plots showing $(Yb/Gd)_{CN}$ vs. $(Sm/Nd)_{CN}$ (Figure 15) of samples with whole rocks chemistries falling in Group 1 (Figure 15B, C, D) all fall along the expected fractionation trend of magma crystallizing along with the accessory minerals titanite and apatite. That is, increasing Yb/Gd with decreasing Sm/Ce through time. Overall, this group of samples antecryst-autocryst analyses preserve a trend distinct and in between that observed in the two Bousquet rhyolites zircon populations. The analyses have a more abrupt increase in Yb/Gd and show less of an asymptotic character than those of Unit 5.3's zircon. Between autocrystic and antecrystic domains in sample 22AB066 (Figure 15B), a loose grouping of autocryst analyses overlap with those of zircon from the tholeiitic Unit 2.0 in the DBL mining camp. The whole rock composition of this sample plots within the arc tholeiite series as well (Figure 8C). Sample 22AB124 also shows a similar, but more tight, vertical grouping of autocryst analyses around a $(Sm/Ce)_{CN}$ ratio of 1, overlapping with Unit 2.0 of the Bousquet Formation. In general, although there is reversals and some samples showing this behaviour more clearly, autocrysts from these samples have a higher ratio of Yb/Gd and lower Sm/Ce than those of antecrysts.

Sample 22AB101A, contains the only zircon directly tied to whole rock geochemistry of Group 2 rocks. However, it is also the only sample which appears to contain zircon of heterogeneous origin. It suffers from a lack of successful analyses, but tends to show a steeper but more diffuse fractionation trend between antecrysts and autocrysts (Figure 15A). Its analyses cluster around the overlapping region of Unit 2.0 and Unit 5.3 data points. It contains a grouping of analyses that have distinctly different chemistries to those seen in the Group 1 samples, occurring around a

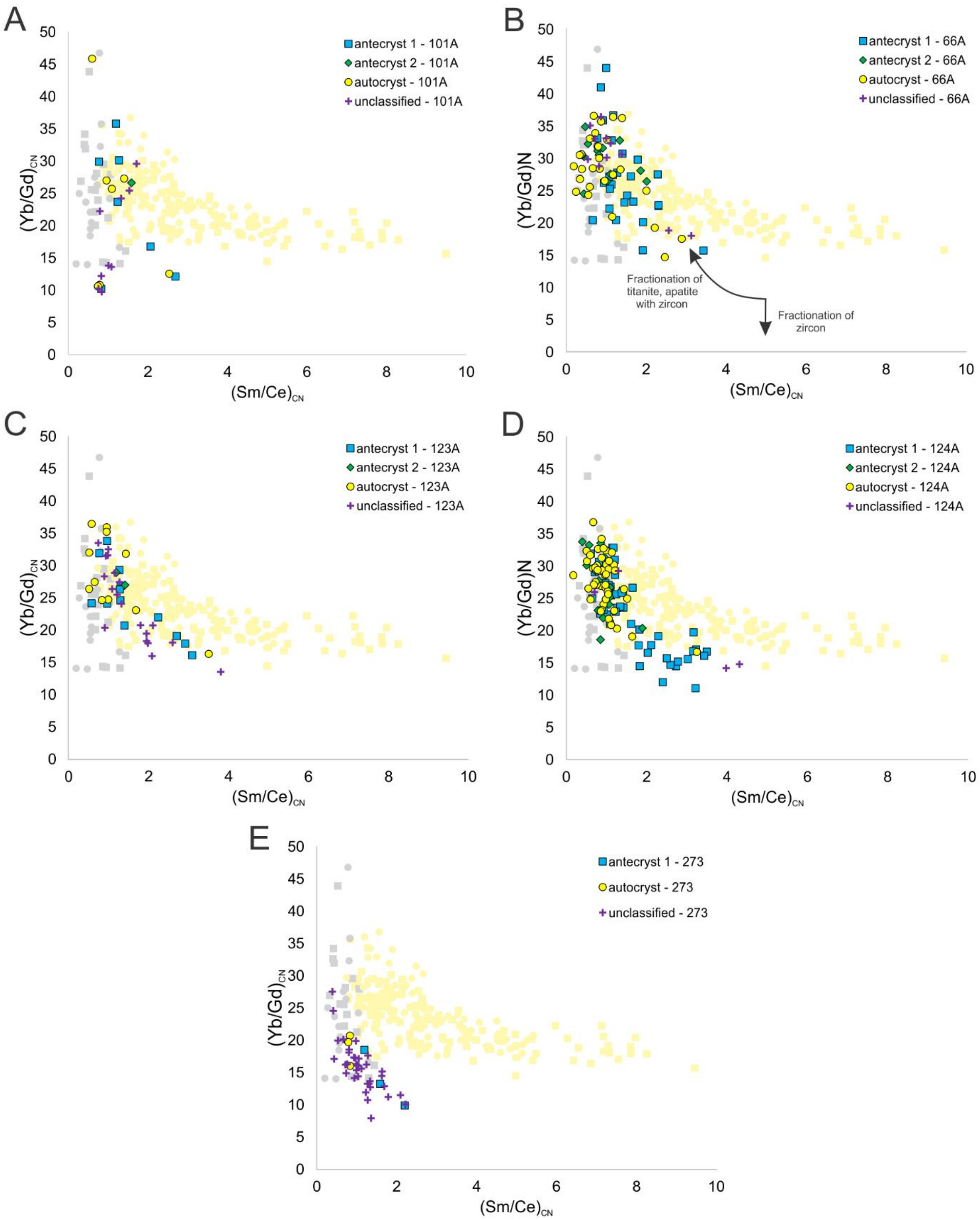
A
(Yb/Gd)CN
(Sm/Ce)CN
■ antecryst 1 - 101A
◆ antecryst 2 - 101A
○ autocryst - 101A
+ unclassified - 101A
B
(Yb/Gd)N
(Sm/Ce)CN
■ antecryst 1 - 66A
◆ antecryst 2 - 66A
○ autocryst - 66A
+ unclassified - 66A
Fractionation of titanite, apatite with zircon
Fractionation of zircon
C
(Yb/Gd)CN
(Sm/Ce)CN
■ antecryst 1 - 123A
◆ antecryst 2 - 123A
○ autocryst - 123A
+ unclassified - 123A
D
(Yb/Gd)N
(Sm/Ce)CN
■ antecryst 1 - 124A
◆ antecryst 2 - 124A
○ autocryst - 124A
+ unclassified - 124A
E
(Yb/Gd)CN
(Sm/Ce)CN
■ antecryst 1 - 273
○ autocryst - 273
+ unclassified - 273
0
5
10
15
20
25
30
35
40
45
50
0
2
4
6
8
10

Figure 15 (previous page): Plots of chondrite-normalized Yb/Gd ratio vs. chondrite-normalized Sm/Ce ratio. Inset arrows show general trends expected for zircon fractionation only and co-crystallization of titanite and/or apatite with zircon. Signified in the inset legends are zircons from samples of felsic volcanic rocks taken for this study (Swayze Area), as well as reference data of zircon of the Lower Bousquet (Unit 2.0, grey) and Upper Bousquet (Unit 5.3, pale-yellow) rhyolitic-rhyodacitic lithologies in the Doyon-Bousquet-LaRonde mining district (unpublished data, Daya, 2023). A) Sample 22AB101A. B) Sample 22AB066A. C) Sample 22AB123A. D) Sample 22AB124A. E) Sample 95HNB-0273.

$(Sm/Ce)_{CN}$ value of 1 and between 10 and 15 $(Yb/Gd)_{CN}$. This grouping does not coincide with the expected trend of zircon trace element evolution during crystallization with the aforementioned accessory minerals. It may be indicative of zones that grew during conditions where zircon was the main accessory mineral controlling the trace element concentration in the melt (removing Yb and concentrating Gd in the remaining melt). This grouping of analyses was all taken from within the dark irregular overgrowth zones shown in Figure 15E. Sample 95HNB-273 is interpreted to be within the northern felsic package containing Group 2 felsic to intermediate rocks. The trace element trend observed is nearly linear with no asymptotic behaviour and is steeper than that observed in the Unit 5.3 zircon (Figure 15E). It shows some similarity in slope to that of the Group 1 zircon, however it is apparently translated to the left and is occurs over a smaller $(Yb/Gd)_{CN}$ window. It should be noted that these analyses nearly overlap with the previously described grouping in sample 22AB101A.

Plots involving $(Th/U)_{CN}$ vs $(Yb/Gd)_{CN}$ (Figure 16) show two distinct trends observed in this studies' samples. The plots of Group 1 zircon overlap with those of Unit 5.3 from the Bousquet Formation (Figure 16B, C, D). The expected trend between antecrystic core (antecryst 1) and autocrystic rim in terms of Th/U and Yb/Gd in zircon is shown in the inset arrows in Figure 16B. Theses analyses generally show the expected trace element signatures of zircon co-crystalizing with titanite and apatite. Titanite and apatite's removal of Th and dominant control over the Yb/Gd ratio in the melt overpowers that of zircon. Sample 22AB124A demonstrates the expected trend exceptionally (Figure 16D). Sample 22AB101A had a similar Th/U vs Yb/Gd trend to that seen in the Group 1 samples (Figure 16A). The trend is defined by 15 analyses, although the antecryst

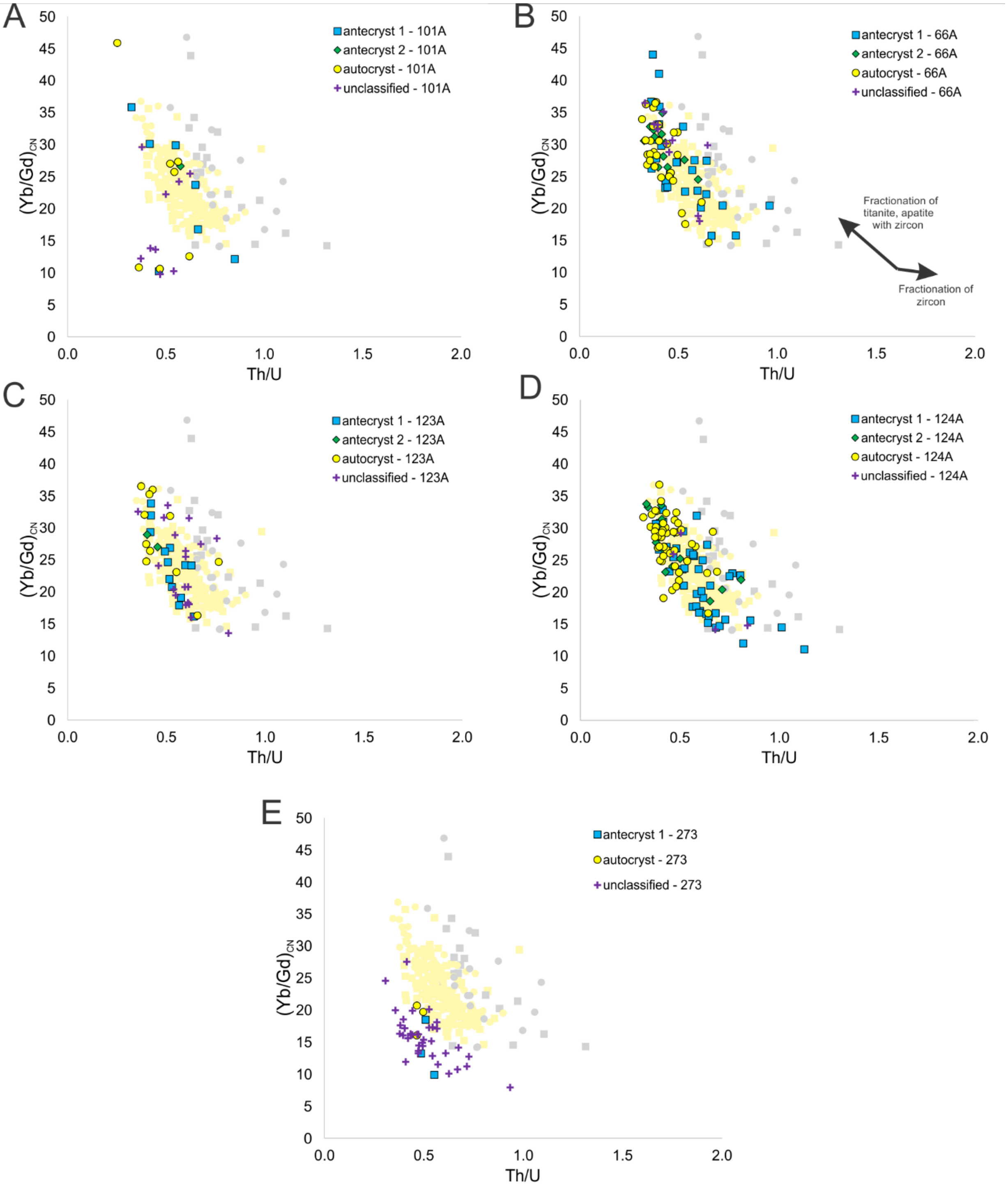
A
antecryst 1 - 101A
antecryst 2 - 101A
autocryst - 101A
unclassified - 101A
B
antecryst 1 - 66A
antecryst 2 - 66A
autocryst - 66A
unclassified - 66A
Fractionation of titanite, apatite with zircon
Fractionation of zircon
C
antecryst 1 - 123A
antecryst 2 - 123A
autocryst - 123A
unclassified - 123A
D
antecryst 1 - 124A
antecryst 2 - 124A
autocryst - 124A
unclassified - 124A
E
antecryst 1 - 273
autocryst - 273
unclassified - 273
(Yb/Gd)CN
0
5
10
15
20
25
30
35
40
45
50
Th/U
0.0
0.5
1.0
1.5
2.0

Figure 16 (Previous Page): Plot of chondrite normalized Yb/Gd vs. Th/U. Inset shows same trends as in Figure 15. Signified in the inset legends are zircons from samples of felsic volcanic rocks taken for this study (Swayze Area), as well as reference data of zircon of the Lower Bousquet (Unit 2.0, grey) and Upper Bousquet (Unit 5.3, pale-yellow) rhyolitic-rhyodacitic lithologies in the Doyon-Bousquet-LaRonde mining district (unpublished data, Daya, 2023). A) Sample 22AB101A. B) Sample 22AB066A. C) Sample 22AB123A. D) Sample 22AB124A. E) Sample 95HNB-0273.

autocryst relationship was less clear. It also preserved the same grouping observed in Figure 15A. These analyses again came from the darker regions seen in the CL images, while the ones showing the same trend as the Group 1 rocks are from the more luminescent and oscillatory zones. This further reinforces the notion that these different growth zones likely represent major differences in the chemistry of coexisting magma at different stages of growth, and indicate that the antecrystic zones may be inherited. Analyses from sample 95HNB-273 (Figure 16E) show a vastly different trace element character than those in the Group 1 samples. They are characterized by having a more linear pattern, overall a smaller Yb/Gd ratio and apparently capturing a shorter/less dramatic fractionation trend. The trend shown by these analyses overlaps with the grouping of dark zone analyses seen in sample 22AB101A in Figure 16A.

The plots involving Hf (ppm) vs Ti (ppm) in Figure 17 show the complex nature of the samples taken for this study, as well sample 93HNB-206B which is an example of zircon with an obviously inherited/xenocrystic core (Figure 14E; Figure 17E). Group 1 samples (Figure 17A, C, D) frequently show evidence of the expected trace element trend of zircon crystallizing from a cooling magma chamber, followed by a reversal of the trend and then a resumption of normal cooling behaviour. Not all paired analyses show this whole story, however they all tell part of it. Since the zircon population is interpreted to be of homogeneous origin, individual analyses capture snapshots of chemical and interpreted physical conditions from a variety of different times and possibly locations within the magma chamber. These interruptions in the expected trend of temperature (Ti) and chemical evolution (Hf) in crystallizing zircon can be caused by several processes, however the most likely is that the magma chamber was replenished with hotter, less evolved magma. Sample 22AB101A had less paired analyses so the trend and Ti range are less confident (Figure 17B). Nonetheless we can observe that its points define less of an obvious trend and have a more stochastic distribution.

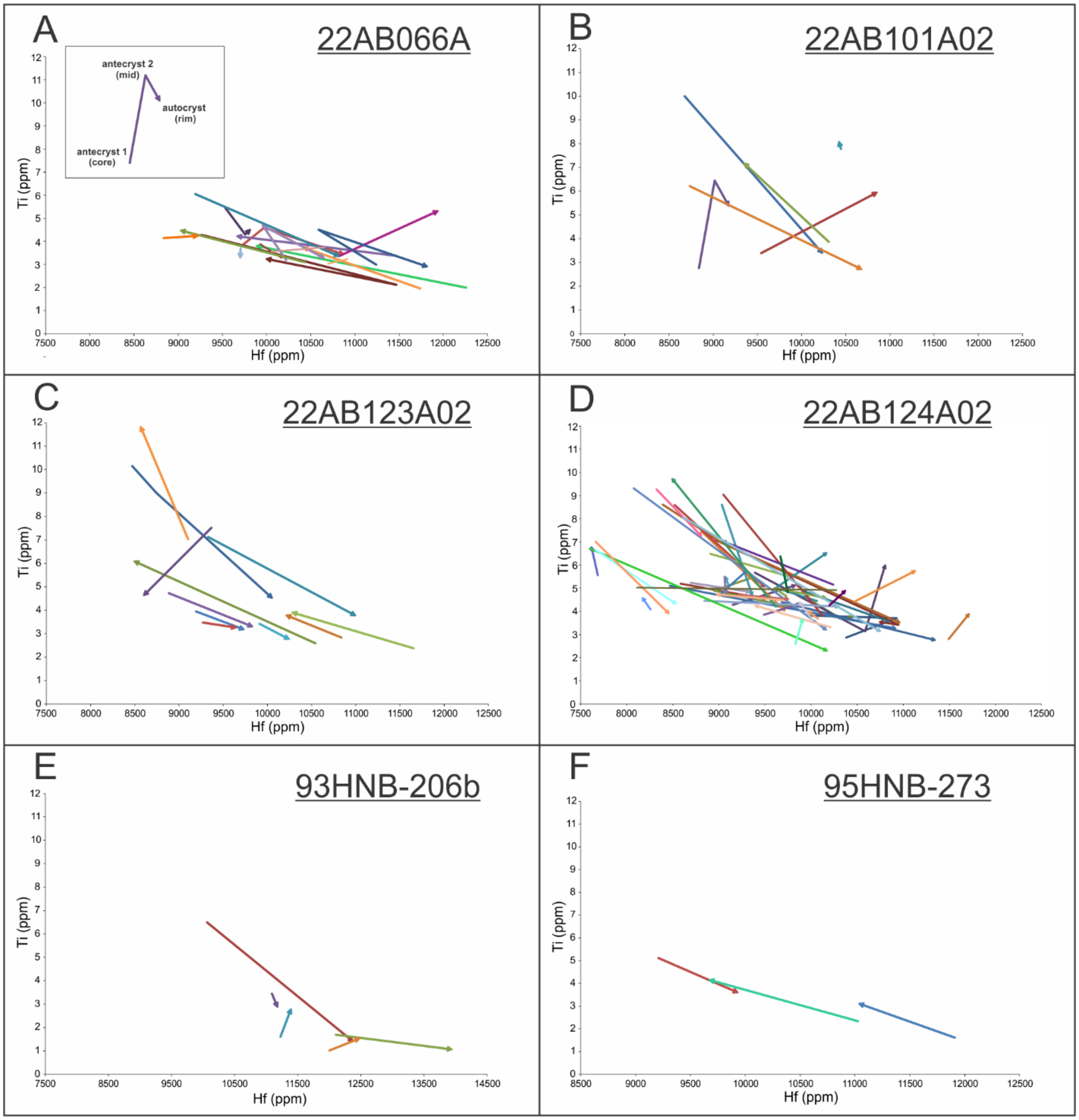

Figure 17: Hf (ppm) vs Ti (ppm) plots for all paired analyses (zircon crystals where two or more analyses were obtained from them). Inset image showing what different nodes on the lines represent. Sample 93HNB-206B is shown to give an example of the character of zircon with inherited cores.

4.7 Zircon U-Pb CA-ID-TIMS Geochronology

Late in this study's progression, zircon CA-ID-TIMS dates began becoming available from BSU Isotope Geology Laboratory. The full data sets can be viewed in Supplemental Materials Table 5. The calculated zircon ^{207}Pb/^{206}Pb dates were deemed more reliable given the age of the rocks and the likelihood of uranium or lead loss. It should be noted that although sample 93HNB-206 was analyzed for this study, it is outside of the study area and will not be discussed. Samples without a weighted mean had more than one distinct zircon population.

Sample 95HNB-0273 is a zircon mount obtained from the GSC, taken from an ash to crystal tuff. The outcrop where this sample was taken is within the northern felsic volcanic package, proximal to where the Group 2 samples were taken. Zircon from this sample were previously analyzed using mechanical abrasion ID-TIMS and returned a weighted mean age of 2696 ± 2 Ma (van Breemen et al., 2006; Figure 4, geochronology location 1). For this study, the five zircon selected returned a CA-ID-TIMS ^{207}Pb/^{206}Pb weighted mean date of 2692.46 ± 0.64 Ma.

Sample 22AB066A was taken from an outcrop in the southern felsic volcanic package, near the sub-economic VMS (Figure 4). Its whole rock geochemistry places it within the Group 1 REE pattern, and it is a plagioclase-pyric fragmental dacite. The five zircon selected for this study yield a weighted mean CA-TIMS ^{207}Pb/^{206}Pb date of 2707.24 ± 0.17 Ma.

Sample 22AB101A02 was taken from a massive quartz-phyric rhyolite/sub-volcanic intrusion that is in contact with a komatiite. The outcrop is in a fault bounded area with little temporal constraints. Based on whole rock geochemistry, it falls into Group 2. Six zircon were dated and yielded CA-ID-TIMS ^{207}Pb/^{206}Pb ages ranging from 2707.97 ± 0.34 to 2688.05 ± 0.37 Ma. The older ages likely came from inherited zircon from the underlying Tisdale assemblage (2710 – 2704 Ma), while the younger population represents the age of intrusion.

Sample 22AB123A02 is from a plagioclase-phyric fragmental dacite located in the southern felsic volcanic package, near the sub-economic VMS (Figure 4). Its whole rock geochemistry places it in Group 1. Five zircon returned a weighted mean CA-ID-TIMS ^{207}Pb/^{206}Pb age of 2707.82 ± 0.19 Ma.

Sample 22AB124A02 is from a plagioclase-phyric fragmental dacite located in the southern felsic volcanic package, near the sub-economic VMS (Figure 4). Its whole rock geochemistry places it into Group 1. Five zircon returned a weighted mean CA-TIMS ^{207}Pb/^{206}Pb date of 2707.74 ± 0.18

Five grains from 93HNB-206B yield CA-TIMS ^{207}Pb/^{206}Pb dates of 2718.55 ± 0.31 to 2686.87 ± 0.31 Ma.

5.0 Discussion

The goal of this study is to characterize the volcanic rocks in the Swayze Area in order to confidently place them into the chronostratigraphic context of the rest of AGB and comment on the areas VMS potential. Both the northern and southern felsic volcanic packages in which this studies' sampling was concentrated were previously identified and mapped as belonging to the BR (2704 - 2695 Ma). The volcanic environment that deposited the BR rocks elsewhere in the AGB may have been one of the most productive ancient VMS-forming systems on the planet, and therefore understanding its geographic distribution and systematics is of paramount importance. However, after utilizing high-resolution CL images of annealed zircon grains and the thoughtful selection of zircon for U-Pb CA-ID-TIMS dating, it has been found that neither of these felsic volcanic successions in the study area contain BR-aged zircon. Despite containing smoke, in the form of a sub-economic VMS occurrence, the rocks in this area share virtually no similarity to BR rocks associated with productive VMS settings elsewhere in the AGB. Nonetheless, a summary of the geochemical, petrographic, and macroscopic character of the rocks encountered in this area is provided below. Furthermore, it will be shown that the trace element component in zircon hosted in volcanic rocks can be used to fingerprint, distinguish between and correlate chronostratigraphic assemblages in the study area.

5.1 Zircon Trace Element Concentrations

Trace element concentrations in zircon track the coexisting magma's evolution (e.g., Claiborne et al., 2006; Lee et al., 2017; Lee et al., 2020) and can be used to interpret events of magma recharge, crystal fractionation, and contamination. Notably, zircon chemistry is strongly influenced by the crystallization of coeval accessory minerals (e.g., titanite, apatite), that exert control on trace element abundances due to high mineral-melt partition coefficients for select elements (e.g., Sm, Ce, Yb, Gd, Th, U). As these accessory phases grow, changes in magma composition are recorded by coeval zircon (e.g., Prowatke and Klemme, 2005, 2006; Claiborne et al., 2010; Large et al., 2018). Furthermore, trace elements such as Ti and Hf in zircon can track the evolution of the magma chamber by providing proxies for temperature and incompatible element saturation in the melt. Ti will substitute for Zr in zircon's structure more readily at higher crystallization temperatures. It's concentration in zircon can be used to identify instances of magma recharge while the magma chamber is within the zircon saturation temperature, as well as periods of expected cooling trends. Hf is incompatible in most major mineral phases and therefore, will concentrate in the residual melt as the magma chamber cools. However, it will substitute for Zr in zircons structure so its abundance in zircon crystals should increase as the system evolves.

5.2 Group 1

The rocks sampled belonging to Group 1 are characterized by their variable, but generally higher, La_{CN} values and their less HREE depleted values, than Group 2 (Table 2). They are generally found to the south of those of Group 2 and occur in two main horizons, separated from each other by a displaced faulted block of the overlying volcanic stratigraphy. On the western side of Swayze Township there are three samples included in Group 1: 22AB081A, 22AB075A and 22AB086A (see Figure 4, but note station -081 is located on a contact and includes two lithologies). The felsic to intermediate package running from the south eastern extent of Swayze Township, where there is a cluster of stations and the VMS occurrence, and extending east (connecting Pepperbell Lake and Tom Lake), encloses the rest of the Group 1 samples. The samples taken from the area surrounding the VMS occurrence all contain macroscopic textures commensurate with those of fragmental lava flows and volcaniclastic rocks. They range in composition from rhyodacitic-dacitic (Figure 8B) and are mostly calc-alkaline, except for 22AB066A which is tholeiitic. These groupings (Groups 1 and 2), were first identified when plotting the chondrite normalized REE of the samples. Group 1 has a less HREE depleted profile than that of Group 2 with no overlap; which made categorization of samples into these - at first arbitrary – groups, easy. Sample 22AB093A, a dacite located further east of this cluster on the shore of Tom Lake, also contained the same REE pattern and degree of HREE depletion. In the western region containing Group 1 samples, the rocks identified were mostly felsic to intermediate tuffs, however, they still contained the same characteristic REE pattern. The petrography reinforces the macroscopic textures seen in the field and in hand sample (Supplemental materials: Table 3), as well as the modal mineralogy of rocks with those compositions.

Upon mounting, annealing, and CL imaging the zircon from the three Group 1 samples, it was clear that they showed evidence of relatively consistent growth throughout their crystallization, with short lived insubstantial instances of resorption textures. They are large, bright, relatively unfractured and showed no indication of containing inherited cores (Figure 14A, C, D). The zircon trace element data obtained by LA-ICP-MS from antecrystic and autocrystic zones within the three samples' zircon show very similar fraction trends to each other. The Sm/Ce vs Yb/Gd trend in the three samples diverges from that of the Bousquet Formation rhyolites at low Yb/Gd values, however, they overlap with the Unit 2.0 tholeiitic rhyolite in their later growth zones (Figure 15B, C, D). The Th/U vs Yb/Gd contents of the Group 1 samples all appear to preserve the same/equivalent fractionation trends, and are similar to those seen in Unit 5.3 calc-alkaline rhyolite (Figure 16B, C, D).

Finally, the zircon U-Pb CA-ID-TIMS dates for all grains of all three Group 1 samples fall healthily within the 2710 – 2704 Ma window of the Tisdale assemblage (Table 1).

5.3 Group 2

The rocks belonging to Group 2 (Table 2) generally occur north of Swayze Road, with two exceptions. Sample 22AB101A and 22AB081B are both located south of the road. Also, it should be noted that samples 22AB134A and 22AB135A are located just outside of the western extent of the Swayze Township and are not included in Figure 4 (exact locations can be found in Supplemental Materials: Table 1). Rocks within Group 2 range from lapilli tuffs to massive flows and have compositions from rhyolitic to andesitic (Figure 8B). They are all calc-alkaline and are extremely depleted in HREE, even more so than Group 1. There is more variability in the absolute HREE depletion in these samples, however the relative REE pattern remained consistent (Figure 8E).

Zircon separates of sufficient quantity and quality were only obtained for one Group 2 sample taken for this study (Sample 22AB101A; Figure 14B). However, the reanalysis of zircon from a sample taken within the felsic package hosting the rest of the Group 2 samples was able to be supplemented so that the datasets were close to equal in size (Sample 95HNB-273; Figure 14F). The CL images of sample 95HNB-273 paint the picture of a zircon growing under relatively consistent magmatic conditions, similar in texture to that seen in the Group 1 samples. They are relatively small, but are well formed and contain few fractures and imperfections. The smaller size of these zircon limited the amount of paired (antecryst and autocryst) analyses that could be done on single grains. On the other hand, sample 22AB101A contains very dark zircon with evidently severe disruptions to the zircon's concentric growth pattern. The inner zones have faint oscillatory zoning, while the outer less luminescent zones are irregular and the growth seems to have occurred very quickly or with no noticeable fluctuation of cathode illuminescent trace elements. The significant difference in overall CL texture and trace element abundance between the inner and outer zones of these zircon indicate that the cores are likely inherited and crystallized under much different conditions than the rims.

The zircon trace element analyses conducted using LA-ICP-MS support the interpretations made using CL images. Sample 95HNB-0273 shows Sm/Ce and Th/U vs Yb/Gd trends that are internally consistent and unique from those observed in the Group 1 samples (Figure15E; Figure 16E). There is very little similarity in them to those in the referenced Bousquet zircon samples. Although few coupled analyses could be done between core and rim of the same zircon, the analyses still define a fractionation history of zircon crystallizing under the chemical influence of titanite and apatite. In general, they represent a shorter fractionation history than those seen in the Group 1 samples. Zircon from sample 22AB101A have a more complex distribution of Sm/Ce and Th/U vs Yb/Gd values between different crystals (Figure 15A; Figure 16A). A loosely defined trend, with a trajectory similar to that seen in Group 1 samples, is the first component of these analyses. Another group of analyses show a relatively tight spread with no discernable trajectory, but which intersect/overlap with those from sample 95HNB-0273. These two components are unlikely to have developed from within a single magma chamber and do not appear to preserve the same fractionation trend. It is also interesting to note that the analyses that show a tight grouping, overlapping with those of 95HNB-0273, are all from the later dark overgrowth regions in the zircon.

The Group 2 samples yielded much different U-Pb CA-ID-TIMS dates than those of Group 1. The analysis of five grains from 95HNB-0273 yielded a weighted mean date of 2692.46 ± 0.64 Ma. This is significantly younger than the previously reported 2696 ± 2 Ma (van Breemen et al., 2006) U-Pb date for these zircon. This places the rock outside of the 2704 – 2695 Ma BR age range, and into the younger ~2690 – 2680 Ma Porcupine assemblage. This discrepancy in age is likely because the previous dating did not utilize chemical abrasion to remove metamict domains of the zircon that were likely contaminated with common lead, which shifted the calculated age older. Sample 22AB101A had a more complex distribution of U-Pb dates (Supplemental Materials: Table 5). These dates showed two distinct populations within the sample; one that is Tisdale aged and one that is Porcupine aged. One of the analyses gave a calculated age of 2702.89 ± 0.28 Ma. However, the CL image of this grain shows that it contains an inherited core zone, with a distinctly darker zone grown over top of it. This leads us to believe that this is a mixed analysis, containing a significantly older core and younger rim, who’s U-Pb concentrations returns an intermediate age when calculated. The overall age of eruption for this rock is interpreted to the younger, Porcupine assemblage age around 2689 Ma, with inheritance from the older Tisdale assemblage.

5.4 VMS Viability

The strong depletion of HREE's seen in both groups (Figure 8E) is interpreted to indicate that the two groups parental magmas both emanated from deep lithospheric levels within the garnet stability field. However, their source regions likely contained different amounts of garnet in the residual material from which the partial melts were derived, which is why the degree to which the HREE's are depleted is different between the groups. The Y content (x-axis; Figure 8D) of the rocks is also a proxy for the depth at which the parental melt was derived (lower Y, deeper melting). Negative Eu-anomalies are characteristic of rocks that formed from a melt that was produced in a low-pressure environment where plagioclase was stable and/or from which plagioclase fractionated. This is because of the strong compatibility of Eu^{2+} in the plagioclase structure over that of a corresponding melt. An example of the REE pattern of felsic volcanics associated with ore zones of the LaRonde-Penna VMS deposits (Meagher, 2020) are shown in an inset image (Figure 8F) in order to illustrate the dramatic differences between the patterns present in those and this study. Felsic volcanics in this study and data from rhyolites associated with LaRonde-Penna VMS deposit were plotted on the rhyolite discrimination plot developed by Hart (2004) after Lesher 1986 (Figure 8G). Archean rhyolites with trace element values that fall into the FII, FIIIa, and FIIIb fields have been shown to be associated with VMS deposits, whereas FI rhyolites have virtually no association to VMS deposits. As alluded to previously, Yb content in rhyolites is largely controlled by garnet's stability in the source region. At deeper lithospheric levels, garnet is stable and will cause a coexisting melt to be depleted in Yb. At shallower depths, outside of the garnet stability field, the melt will inherit more of the Yb available in the system. Since shallow magmatic sources have been strongly associated with rhyolites hosting and proximal to VMS deposits (Galley et al., 2007), Yb depletion in contemporary rhyolites is typically antithetical to VMS formation (Hart et al., 2004). Group 1 and Group 2 shown in Figure 8E present themselves in Figure 7G as the grouping of points that fall into the FI and FII fields, respectively.

The absolute metal abundances of the mineralized samples from the VMS occurrence in the study area fall outside the range of typical economic VMS ore. Comparing ore metal ratios of this VMS occurrence with the Deloro to Blake River aged Shunsby VMS deposit, shows that the relative metal abundances are dissimilar (Figure 18A). When compared to ore from the Blake River aged LaRonde-Penna deposit, it can also be seen that little similarity exists. The relative proportions of base to precious metals in the samples taken for this study were heavily skewed towards Ag, whereas reference samples from previously mentioned (and more significantly mineralized areas) were not so heavily skewed (Figure 18B).

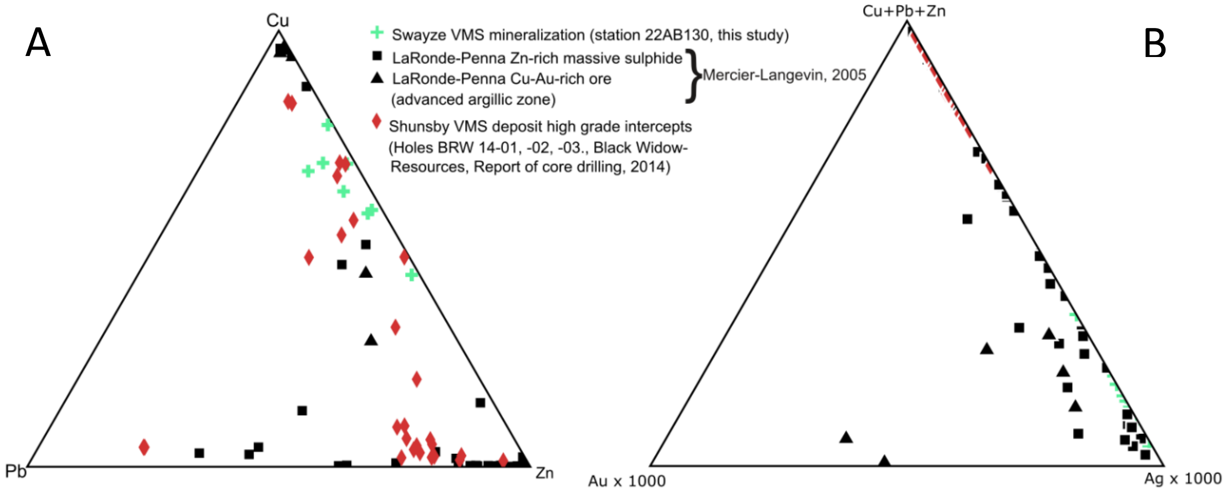

Figure 18: Relative ore mineral abundances of mineralized samples from station 22AB130 taken for this study compared to those of the Shunsby VMS occurrence/deposit in the Swayze area and Zn and Cu-rich ore from the LaRonde-Penna VMS in the eastern AGB. A) Ternary plot showing relative abundances of Cu, Zn, and Pb in mineralized samples from four different VMS localities. B) Ternary plot showing the relative abundances of base metals (Cu+Zn+Pb) in ppm vs Au ppm vs Ag ppm. Note Au and Ag values have had a magnification factor of 1000 applied to them.

Neither of the two groups encountered in the study area show any geochemical resemblance to those of the BR, besides their superficial shared rhyodacitic composition. This means that they are the products of very different volcanic and tectonic environments. Moreover, although these rocks were likely formed under extensional settings like most of the AGB, no notable structures have been identified to indicate that they were genetically related to an anomalous subsidence structure such as a caldera which are present in other productive regions (e.g., Noranda Cauldron). Even without the confirming U-Pb ages placing these rocks outside of the BR, the preponderance of evidence against these rocks being produced in environments which produce VMS deposits in the Archean is ample. VMS deposits require high level magmatic heat sources, while our rocks had signatures of being produced by a deep source. Furthermore, the Tisdale and Porcupine assemblages have not been identified elsewhere in the AGB as assemblages associated with significant VMS mineralization, so it is no wonder that there is not any here.

5.5 Technical Synergy

The techniques used for this study indicated to us early on that the rocks sampled exhibit bimodal signatures of a variety of parameters. The suite of techniques used complimented each other and allowed for many of the samples to be able to be confidently grouped, as well as allowing for inferences to be made about each group. These two groups of samples show different degrees of HREE depletion, different zircon growth zoning patterns, different zircon trace elements, different zircon U-Pb dates and are located in different geographic areas. It is our contention that this suite of techniques allowed the rocks of two different assemblages to be identified as such without the need for absolute dating. Of course, the absolute dating was necessary to place them into the chronostratigraphic context of the rest of the AGB, but it is interesting that the discrimination between two assemblages in close proximity to each other can be done prior to U-Pb dating.

6.0 Conclusions

This study found that these two felsic volcanic packages in the study area, previously thought to belong to the BR, in fact comprise the assemblages that temporally flank the BR. The southern succession of dominantly fragmental felsic volcanic rocks, with occasional intermediate to mafic volcanic components, are dominantly of Tisdale age. The northern succession of felsic to intermediate flows and pyroclastics is an example of contemporaneous volcanism to the dominantly sedimentary, Porcupine assemblage. Prior to the precise zircon U-Pb CA-ID-TIMS dating that placed them in largely barren volcanic assemblages, the discriminations made using REE patterns, inferred magmatic sources, and dissimilar zircon trace elements to those of felsic volcanics in productive regions, made their association with VMS' unlikely. This study highlights the importance of using chemical abrasion during zircon U-Pb ID-TIMS dating of Archean rocks. It also shows that careful interpretation of CL images of zircon prior to further work is crucial in order to properly interpret the data.

6.1 Recommendations for Future Work

- Reanalyze other zircon taken from the lateral extents of these felsic packages which were previously dated as BR
- Compare the zircon trace element chemistry of this study to those of zircon from known Tisdale and Porcupine assemblages to evaluate if this could be a useful tool for long distance correlation
- Compare zircon-hosted SMI from this area to those in more productive VMS settings (associated PhD thesis)

References

Ayer, J. A., Amelin, Y., Corfu, F., Kamo, S. L., Ketchum, J., Kwok, K. & Trowell, N. 2002a. Evolution of the southern Abitibi greenstone belt based on U-Pb geochronology: autochthonous volcanic construction followed by plutonism, regional deformation and sedimentation. Precambrian Research115, 63–95.

Ayer, J. A., Ketchum, J. W. F. & Trowell, N. F. 2002b. New geochronological and neodymium isotopic results from the Abitibi greenstone belt, with emphasis on the timing and the tectonic implications of Neoarchean sedimentation and volcan-ism. Summary of field work and other activities. Ontario Geological Survey, Open File Report 6100, pp. 5.1–5.16.

Ayer, J.A., Thurston, P.C., Bateman, R., Dubé, B., Gibson, H.L., Hamilton, M.A., Hathway,B., Hocker, S.M., Houlé, M.G., Hudak, G., Ispolatov, V.O., Lafrance, B., Lesher, C.M.,MacDonald, P.J., Péloquin, A.S., Piercey, S.J., Reed, L.E. and Thompson, P.H. 2005. Overview of results from the Greenstone Architecture Project: Discover Abitibi Initiative; Ontario Geological Survey, Open File Report 6154, 146p.

Camiré, G.E., and Burg, J.P., 1993, Late Archaean thrusting in the northwestern Pontiac subprovince, Canadian Shield: Precambrian Research, v. 61, p. 51–66.

Bateman, R., Ayer, J.A., and Dubé, B., 2008, The Timmins-Porcupine gold camp, Ontario: Anatomy of an Archean greenstone belt and ontogeny of gold mineralization: Economic Geology, v. 103, p. 1285–1308.

Bedeaux, P., Pilote, P., Daigneault, R., and Rafini, S., 2017, Synthesis of the structural evolution and associated gold mineralization of the Cadillac fault, Abitibi, Canada: Ore Geology Reviews, v. 82, p. 49–69.

Bennett, G., Dressler, B.O., and Robertson, J.A., 1991, The Huronian Supergroup and associated intrusive rocks, in Thurston, P.C., Williams, H.R., Sutcliffe, R.H., and Stott, G.M., eds., Geology of Ontario: Ontario Geological Survey Special Volume 4, Part 1, p. 549–591.

Benn, K., and Moyen, J.F., 2008, The Late Archean Abitibi-Opatica terrane, Superior province: A modified oceanic plateau: Geological Society of America Special Paper, v. 440, p. 173–197.

Bleeker, W., 2012, Lode gold deposits in ancient deformed and metamorphosed terranes: The role of extension in the formation of Timiskaming basins and large gold deposits, Abitibi greenstone belt—a discussion: Ontario Geological Survey Open File Report 6280, p. 47-1–47-12.

——2015, Synorogenic gold mineralization in granite-greenstone terranes: The deep connection between extension, major faults, synorogenic clastic basins, magmatism, thrust inversion, and long-term preservation: Geological Survey of Canada Open File 7852, p. 25–47.

Born, P., 1995, A sedimentary basin analysis of the Abitibi greenstone belt in the Timmins area, northern Ontario, Canada: Unpublished Ph.D. thesis, Ottawa, Ontario, Canada, Carleton University, 489 p.

Burns, J. G., 2014, REPORT OF CORE DRILLING APRIL – MAY, 2014 ON THE SHUNSBY VMS Cu-Zn PROJECT CUNNINGHAM TOWNSHIP NORTH CENTRAL, ONTARIO. Black Widow Resources Inc.

Camiré, G.E., and Burg, J.P., 1993, Late Archaean thrusting in the northwestern Pontiac subprovince, Canadian Shield: Precambrian Research, v. 61, p. 51–66.

Cathles, L. M., 1981, Fluid flow and genesis of hydrothermal ore deposits.

Cathles, L. M., Erendi, A. H. J., & Barrie, T. J. E. G., 1997, How long can a hydrothermal system be sustained by a single intrusive event?. Economic Geology, 92(7-8), 766-771.

Cattell, A., Krogh, T.E., and Arndt, N.T., 1984, Conflicting Sm-Nd whole-rock and U-Pb zircon ages for Archean lavas from Newton Township, Abitibi belt, Ontario: Earth and Planetary Science Letters, v. 70, p. 280–290.

Condon D.J., Schoene B., McLean N.M., Bowring S.A., Parrish R, 2015, Metrology and traceability of U-Pb isotope dilution geochronology (EARTHTIME Tracer Calibration Part I): Geochimica et Cosmochimica Acta, v. 164, p. 464-480.

Corfu, F., Hanchar, J. M., Hoskin, P. W., Kinny, P., & Hoskin, P. W. O., 2003, Zircon. Mineralogical Society of America and Geochemical Society, Reviews in Mineralogy and Geochemistry.

Crowley, J.L., Schoene, B., Bowring, S.A., 2007, U-Pb dating of in the Bishop Tuff at the millennial scale: Geology, v. 35, p. 1123-1126.

Daigneault, R., Mueller, W.U., and Chown, E.H., 2002, Oblique Archean subduction: Accretion and exhumation of an oceanic arc during dextral transpression, Southern Volcanic Zone, Abitibi subprovince, Canada: Precambrian Research, v. 115, p. 261–290. ——2004, Abitibi greenstone belt plate tectonics: The diachronous history of arc development, accretion and collision: Developments in Precambrian Geology, v. 12, p. 88–103.

Dimroth, E., Imreh, L., Rocheleau, M., and Goulet, N., 1982, Evolution of the south-central part of the Archean Abitibi belt, Quebec. Part 1: Stratigraphy and paleogeographic model: Canadian Journal of Earth Sciences, v.19, p. 1729–1758.

Dimroth, E., Imreh, L., Goulet, N., and Rocheleau, M., 1983, Evolution of the south-central segment o f the Archean Abitibi belt, Quebec. Part III: Plutonic and metamorphic evolution and geotectonic model: Canadian Journal of Earth Sciences, v. 20, p. 1374–1388.

Dinel, E., Fowler, A.D., Ayer, J., Still, A., Tylee, K., and Barr, E., 2008b, Lithogeochemical and stratigraphic controls on gold mineralization within the metavolcanic rocks of the Hoyle Pond mine, Timmins, Ontario: Economic Geology, v. 103, p. 1341–1363.

Dubé, B. and Mercier-Langevin, P. 2020, Gold Deposits of the Archean Abitibi Greenstone Belt, Canada: Special Publications in Economic Geology, v. 23, p. 669-708.

Franklin, J.M., Gibson, H.L., Jonasson, I.R., and Galley, A.G., 2005, Volcanogenic massive sulfide deposits: Economic Geology 100th Anniversary Volume, p. 523–560.

Galley, A.G., Hannington, M.D., and Jonasson, I.R., 2007, Volcanogenic massive sulphide deposits, in Goodfellow, W.D., ed., Mineral deposits of Canada: A synthesis of major deposit-types, district metallogeny, the evolution of geological provinces, and exploration methods: Mineral Deposits Division, Geological Association of Canada, Mineral Deposits Division Special Publication no. 5, p. 141–161.

Galley, A.G., and Lafrance, B., 2014, Setting and evolution of the Archean synvolcanic Mooshla intrusive complex, Doyon-Bousquet-LaRonde mining camp, Abitibi greenstone belt: Emplacement history, petrogenesis, and implications for Au metallogenesis: Economic Geology, v. 109, p. 205–229.

Gemmell, T.P. and Buyers, A. 2022. Preliminary Geology and Mineral Potential of Dore and Swayze Townships and Part of Garnet Township, Swayze Area, Abitibi Greenstone Belt; in Summary of Field Work and Other Activities, 2022, Ontario Geological Survey, Open File Report 6390, p.6-1 to 6-11.

Gibson, H., and Galley, A., 2007, Volcanogenic massive sulphide deposits of the Archean, Noranda district, Québec, in Goodfellow, W.D., ed., Mineral deposits of Canada: A synthesis of major deposit-types, district metallogeny, the evolution of geological provinces, and exploration methods: Mineral Deposits Division, Geological Association of Canada, Special Publication no. 5, p. 533–552.

Gibson, H., Allen, R. L., Riverin, G. and Lane, T. E. (2007). The VMS Model: Advances and Application to Exploration Targeting.

Gerstenberger, H., Haase, G., 1997, A highly effective emitter substance for mass spectrometric Pb isotope ratio determinations: Chemical Geology, v. 136, p. 309-312.

“Government of Canada.” Canada.ca, / Gouvernement Du Canada, 18 Aug. 2022, https://www.canada.ca/en/campaign/critical-minerals-in-canada/critical-minerals-an-opportunity-for-canada.html.

Hannington, M.D., Gemmell, T., and Monecke, T., 2017, The Kidd Creek volcanogenic massive sulfide deposit—-An update: Reviews in Economic Geology, v. 19, p. 81–102.

Hart, T. R., Gibson, H. L., and Lesher, C. M., 2004, TRACE ELEMENT GEOCHEMISTRY AND PETROGENESIS OF FELSIC VOLCANIC ROCKS ASSOCIATED WITH VOLCANOGENIC MASSIVE Cu-Zn-Pb SULFIDE DEPOSITS. Economic Geology, 99, p. 10003-1013.

Heather, K.B., and Shore, G.T., 1999, Geology, Swayze greenstone belt, Ontario: Geological Survey of Canada Open File 3384a, scale 1:50,000.

Heather, K.B., 2001, The geological evolution of the Archean Swayze greenstone belt, Superior province, Canada: Unpublished Ph.D. thesis, Staffordshire, U.K., Keele University, 370 p.

Herzig PM, Hannington MD, Arribas A Jr, 1998, Sulfur isotopic composition of hydrothermal precipitates from the Lau back-arc: implications for magmatic contributions to seafloor hydrothermal systems. Miner Deposita 33:226–237

Hiess, J., Condon, D.J., McLean, N., Noble, S. R., 2012, 238U/235U systematics in terrestrial uranium-bearing minerals: Science, v. 335, p. 1610-1614.

Jackson, S.L., and Fyon, J.A., 1991, The western Abitibi subprovince in Ontario, in Thurston, P.C., Williams, H.R., Sutcliffe, R.H., and Stott, G.M., eds., Geology of Ontario: Ontario Geological Survey Special Volume 4, Part 1, p. 405–482.

Jackson, S.L., Fyon, J.A., and Corfu, F., 1994, Review of Archean supracrustal assemblages of the southern Abitibi greenstone belt in Ontario, Canada: Products of micro-plate interaction within a large-scale plate-tectonic setting: Precambrian Research, v. 65, p. 183–205.

Jaffey, A.H., Flynn, K.F., Glendenin, L.E., Bentley, W.C., Essling, A.M., 1971, Precision measurements of half-lives and specific activities of 235U and 238U: Physical Review C, v. 4, p. 1889-1906.

Jeon, H., & Williams, I. S., 2018, Trace inheritance—Clarifying the zircon O-Hf isotopic fingerprint of I-type granite sources: Implications for the restite model. Chemical Geology, 476, p. 456-468.

Johnson, C. M., 1989, Isotopic zonations in silicic magma chambers. Geology, 17(12), p. 1136-1139.

Kemp, A. I. S., Whitehouse, M. J., Hawkesworth, C. J., & Alarcon, M. K., 2005, A zircon U-Pb study of metaluminous (I-type) granites of the Lachlan Fold Belt, southeastern Australia: implications for the high/low temperature classification and magma differentiation processes. Contributions to Mineralogy and Petrology, 150, p. 230-249.

Krogh, T.E., 1973, A low contamination method for hydrothermal decomposition of and extraction of U and Pb for isotopic age determination: Geochimica et Cosmochimica Acta v. 37, p. 485-494.

Lajoie, J., and Ludden, J., 1984, Petrology of the Archean Pontiac and Kewagama sediments and implications for the stratigraphy of the southern Abitibi belt: Canadian Journal of Earth Sciences, v. 21, p. 1305–1314.

Le Maitre, R.W. (1989) A Classification of Igneous Rocks and Glossary Terms. 2nd Edition, Blackwell Scientific Publications, Oxford, 193.
Ludwig, K.R., 2003, User's Manual for Isoplot 3.00. Berkeley Geochronology Center: Berkeley, CA, 70 p.

Mason, R., and Melnik, N., 1986, The anatomy of an Archean gold system - The McIntyre-Hollinger complex at Timmins, Ontario, Canada [ext. abs.]: Gold '86: An International Symposium on the Geology of Gold Deposits, Toronto, Canada, 1986, Proceedings Volume, p. 40–55.

Mattinson, J.M., 2005, U-Pb chemical abrasion ("CA-TIMS") method: combined annealing and multi-step partial dissolution analysis for improved precision and accuracy of ages: Chemical Geology, v. 220, p. 47-66.

McDonald, P. J., and Piercey, S., 2018, Geology, Lithogeochemistry and Petrogenesis of Intrusions Associated with Gold Mineralization within the Timmins-Porcupine Gold Camp, Canada. Canadian Journal of Earth Sciences 56 (4).

McNicoll, V., Goutier, J., Dubé, B., Mercier-Langevin, P., Ross, P.S., Dion, C., Monecke, T., Legault, M., Percival, J., and Gibson, H., 2014, U-Pb geochronology of the Blake River Group, Abitibi greenstone belt, Quebec, and implications for base metal exploration: Economic Geology, v. 109, p. 27–59.

Meagher, D. J., 2020, A melt inclusion study of rhyolitic volcanics in the Bousquet Formation, Doyon-Bousquet-LaRonde district, Abitibi Subprovince, Québec: Insight into Archean magmatic processes: Unpublished MSc. thesis, Halifax, Nova Scotia, Canada, Saint Mary's University.

Mercier-Langevin, P., Hannington, M.D., Dubé, B., and Bécu, V., 2010c, The gold content of volcanogenic massive sulphide deposits. Mineralium Deposita, In press. DOI 10.1007/s00126-010-0300-0.

Mercier-Langevin, P., Goutier, J., Ross, P. S., McNicoll, V., Monecke, T., Dion, C., ... & Galley, A. (2011). The Blake River Group of the Abitibi greenstone belt and its unique VMS and gold-rich VMS endowment. Geological Survey of Canada, Open File, 6869, 61.

Mercier-Langevin, P., Dubé, B., Blanchet, F., Pitre, D., & Laberge, A., 2017, The LaRonde Penna Au-rich volcanogenic massive sulfide deposit.

Monecke, T., Mercier-Langevin, P., Dubé, B., and Frieman, B., 2017a, Geology of the Abitibi greenstone belt: Reviews in Economic Geology, v. 19, p. 7–49.

Monecke, T., Gibson, H., and Goutier, J., 2017, Volcanogenic massive sulfide deposits of the Noranda camp: Reviews in Economic Geology, v. 19, p. 169–223.

Mueller, W., and Donaldson, J.A., 1992a, A felsic dike swarm formed under the sea: the Archean Hunter Mine Group, south-central Abitibi belt, Quebec, Canada: Bulletin of Volcanology, v. 54, p. 602–610. ——1992b, Development of sedimentary basins in the Archean Abitibi belt, Canada: An overview: Canadian Journal of Earth Sciences, v. 29, p. 2249–2265.

Pearce, J. A., Harris, N. B. W., and Tindle, A. G., 1984, Trace element discrimination diagrams for the tectonic interpretation of granitic rocks. Journul of Petrology, 25, p. 956-983.

Peccerillo, A., Taylor, S.R. Geochemistry of eocene calc-alkaline volcanic rocks from the Kastamonu area, Northern Turkey. Contr. Mineral. and Petrol. 58, 63–81 (1976). https://doi.org/10.1007/BF00384745

Percival, J.A., Green, A.G., Milkereit, B., Cook, F.A., Geis, W., and West, G.F., 1989, Seismic reflection profiles across deep continental crust exposed in the Kapuskasing uplift structure: Nature, v. 342, p. 416–420.

Percival, J.A., and West, G.F., 1994, The Kapuskasing uplift: A geological and geophysical synthesis: Canadian Journal of Earth Sciences, v. 31, p. 1256–1286.

Piercey, S. J. (2011). The setting, style, and role of magmatism in the formation of volcanogenic massive sulfide deposits. Mineralium Deposita, 46, 449-471.

Rocheleau, M., 1980, Stratigraphie et sédimentologie de l'Archéen dans la région de Rouyn, Abitibi, Québec: Unpublished Ph.D. thesis, Montreal, Quebec, Canada, Université de Montréal, 313 p.

Scott, C.R., Mueller, W.U., and Pilote, P., 2002, Physical volcanology, stratigraphy and lithogeochemistry of an Archean volcanic arc: Evolution from plume-related volcanism to arc rifting of SE Abitibi greenstone belt, Vald'Or, Canada: Precambrian Research, v. 115, p. 223–260.

Schaltegger, U., Ovtcharova, M., Gaynor, S.P., Schoene, B., Wotzlaw, J-F., Davies, J.F.H.L., Farina, F., Breber, N.D., Szymanowski, D., and Chelle-Michou, C., 2021, Long-term repeatability and interlaboratory reproducibility of high-precision ID-TIMS U-Pb geochronology: Journal of Analytical Atomic Spectrometry, v. 36, p. 1466-1477.

Schmitz, M.D., Schoene, B., 2007, Derivation of isotope ratios, errors and error correlations for U-Pb geochronology using 205Pb-235U-(233U)-spiked isotope dilution thermal ionization mass spectrometric data: Geochemistry, Geophysics, Geosystems (G3), v. 8, Q08006, doi:10.1029/2006GC001492.

Sláma, J., Košler, J., Condon, D.J., Crowley, J.L., Gerdes, A., Hanchar, J.M., Horstwood, M.S.A., Morris, G.A., Nasdala, L., Norberg, N., Schaltegger, U., Schoene, B., Tubrett, M.N., and Whitehorse, M.J., 2008, Plešovice zircon-a new natural reference material for U-Pb and Hf isotopic microanalysis: Chemical Geology, v. 249, p. 1-35.

Smithies, R. H., Howard, H. M., Kirkland, C. L., Korhonen, F. J., Medlin, C. C., Maier, W. D., ... & Wingate, M. T. D., 2015, Piggy-back supervolcanoes—long-lived, voluminous, juvenile rhyolite volcanism in Mesoproterozoic central Australia. Journal of Petrology, 56(4), p. 735-763.

Stone, W.E., 1990, Archean volcanism and sedimentation in the Bousquet gold district, Abitibi greenstone belt, Quebec: Implications for stratigraphy and gold concentration: Geological Society of America Bulletin, v. 102, p. 147–158.

Sun, S. and McDonough, W.F. (1989) Chemical and Isotopic Systematics of Oceanic Basalts: Implications for Mantle Composition and Processes. Geological Society, London, Special Publications, 42, 313-345. https://doi.org/10.1144/GSL.SP.1989.042.01.19.

van Breemen, O., Heather, K.B., and Ayer, J.A., 2006: U-Pb geochronology of the Neoarchean Swayzesector of the southern Abitibi greenstone belt; Geological Survey of Canada, Current Research 2006-F1,32 p.

Thurston, P.C., Ayer, J.A., Goutier, J., and Hamilton, M.A., 2008, Depositional gaps in Abitibi greenstone belt stratigraphy: A key to exploration for syngenetic mineralization: Economic Geology, v. 103, p. 1097–1134.

Wendt, I., and Carl, C., 1991, The statistical distribution of the mean square weighted deviation: Chemical Geology, v. 86, p. 275–285.

Wiedenbeck, M., Hanchar, J.M., Peck, W.H., Sylvester, P., Valley, J., Whitehouse, M., Kronz, A., Morishita, Y., Nasdala, L., 2004, Further characterisation of the 91500 zircon crystal: Geostandards and Geoanalytical Research, v. 28, p. 9-39.

Winchester, J.A. and Floyd, P.A. (1977) Geochemical Discrimination of Different Magma Series and Their Differentiation Product Using Immobile Elements. Chemical Geology, 20, 325-343. http://dx.doi.org/10.1016/0009-2541(77)90057-2.

Young, G.M., and Nesbitt, H.W., 1985, The Gowganda Formation in the southern part of the Huronian outcrop belt, Ontario, Canada: Stratigraphy, depositional environments and regional tectonic significance: Precambrian Research, v. 29, p. 265–301.

Young, G.M., Long, D.G.F., Fedo, C.M., and Nesbitt, H.W., 2001, Paleoproterozoic Huronian basin: Product of a Wilson cycle punctuated by glaciations and a meteorite impact: Sedimentary Geology, v. 141–142, p. 233–254.

Table 1: Sample list, characteristics, and analyses done on samples taken in study area (Figure 3).

				Analysis					Location (UTM zone 17)	
Sample	**Eruptive mechanism, composition (field)**	**Suspected voclanic assemblage, confidence**	**Mineralization**	**Whole rock geochemistry**	**Petrography**	**Zircon separates obtained**	**LA-ICP-MS trace elements**	**CA-ID-TIMS**	**Easting**	**Northing**
22AB064A	Dyke, gabbro/diabase	Matachewan dyke swarm, high	Barren	x	x				378447	5293789
22AB066A	Fragmental flow, dacitic	Tisdale, high	Disseminated pyrite (trace)	x	x	x	x	x	378728	5293573
22AB069SS	Massive flow, komatiitic	Porcupine, very low	Barren	x	x				375949	5294027
22AB075A	Tuff breccia, andesitic	Porcupine, medium	Barren	x	x				373300	5294652
22AB081A	Massive flow, andesitic	Porcupine, medium	Barren	x	x				373070	5295162
22AB081B	Massive flow, dacitic	Porcupine, medium	Barren	x	x				373070	5295162
22AB086A	Lapilli tuff, rhyodacitic	Porcupine, medium	Barren	x	x				373634	5293456
22AB091A	Massive flow, dacitic	Porcupine, medium	Barren	x	x				381325	5296630
22AB093A	Massive flow, dacitic	Tisdale, low	Barren	x	x				385933	5294373
22AB095A02	Pillowed flow, basaltic	Tisdale, very low	Barren	x	x				385256	5292294
22AB098A02	Fragmental flow, rhyodacitic	Tisdale, very low	Barren	x	x				378040	5293879
22AB101A02	Massive flow, rhyolitic	Porcupine, very low	Barren	x	x	x	x	x	375919	5293983
22AB122A02	Massive flow, andesitic	Tisdale, low	Barren	x	x				377455	5294189
22AB123A02	Fragmental flow, dacitic	Tisdale, high	Disseminated pyrite (2%)	x	x	x	x	x	379025	5293563
22AB124A02	Fragmental flow, rhyodacitic	Tisdale, high	Disseminated pyrite (trace)	x	x	x	x	x	379122	5293636
22AB134A02	Massive flow, andesitic	Porcupine, medium	Barren	x	x				370204	5296531
22AB135A02	Massive flow, basaltic	Porcupine, medium	Barren	x	x				370339	5296412
22AB140A02	Massive flow, andesitic	Porcupine, medium	Barren	x	x				371879	5297141
22AB145A02	Massive flow, basaltic	Tisdale, very low	Barren	x	x				388139	5293319
22AB165A02	Massive flow, andesitic	Tisdale, very low	Barren	x	x				386150	5292457
22AB171A02	Massive flow, rhyodacitic	Porcupine, medium	Barren	x	x				376567	5299425
22AB172A02	Tuff, dacitic	Porcupine, medium	Barren	x	x				376556	5299342
93HNB-206B*	Qz-fsp-porphyry intrusion	Porcupine, high	Barren			x	x	x	375257	5286520
95HNB-0273**	Ash tuff, rhyolitic	Porcupine, high	Barren			x	x	x	376536	5293019

*Obtained from Previously reported date in van Breeman et al., 2006, three grains returning an age of 2699 ± 2.8 Ma.

**Previously dated by Heather, 1997 and reported by van Breemen et al., 2006. Six grains returning an age of 2696 ± 2 Ma.

Table 2: Whole Rock Geochemistry of Swayze Area Volcancis (Swayze, Dore, and Garnet townships), Abitibi Greenstone Belt.

	22AB064A	**22AB066A**	**22AB069SS**	**22AB075A**	**22AB081A**	**22AB081B**	**22AB086A**	**22AB091A**	**22AB093A**	**22AB095A02**	**22AB098A02**	**22AB101A02**	**22AB122A02**	**22AB123A02**	**22AB124A02**	**22AB134A02**	**22AB135A02**	**22AB140A02**	**22AB145A02**	**22AB165A02**	**22AB171A02**	**22AB172A02**
	Gabbro - Subalkaline	Rhyodacite - Tholeiitic	Komatiite	Andesite - Latite	Andesite - Tholeiitic	Dacite - Calc-alkaline	Dacite - Calc-alkaline	Dacite - Calc-alkaline	Andesite - Calc-alkaline	Basalt - Tholeiitic	Rhyodacite - Calc-alkaline	Rhyolite - Calc-alkaline	Basaltic andesite - Tholeiitic	Dacite-andesite - Calc-alakaline	Dacite - Calc-alkaline	Dacite - Calc-alkaline	Rhyodacite - Calc-alkaline	Basaltic andesite - Shoshonitic	Basalt - Calc-alkaline	Basalt - Calc-alkaline	Rhyodacite - High-K calc-alkaline	Dacite - Calc-alkaline
Major Oxides (%)																						
SiO2	50.3	68.3	41.7	56.8	55.5	67.8	64.8	64.6	54.2	50.2	60.6	71.4	47.4	55.2	66.5	64.9	65.9	45.8	48.4	47.5	64.2	64.4
Al2O3	12.3	15.8	5.95	13.6	12.8	14.85	16	15.1	12.85	14.65	14.25	15.4	14.1	12.95	16.1	14.95	13.9	15.7	15.55	14.25	14.75	15.75
Fe2O3	17.35	3.4	10.3	5.34	7.03	3.45	3.24	3.77	5.74	11.75	3.24	2	13.25	10.9	4.32	3.41	2.8	10.45	11.6	11.45	2.85	2.81
CaO	7.79	3.4	3.48	7.87	6.2	2.44	2.11	3.09	7.3	10.6	2.61	1.45	7.73	5.9	1.34	2.78	3.12	6.8	5.86	10.9	3.78	3.36
MgO	3.92	1.7	28.3	5.13	5.68	1.79	1.3	1.58	2.84	7.26	2.01	0.6	7.06	2.49	1.6	1.6	1.59	6.11	8.39	7.98	1.34	1.02
Na2O	2.77	5.87	0.05	3.59	4.17	4.25	4.81	4.16	3.25	2.1	4.53	5.37	2.07	1.46	4.88	4.26	4.97	1.15	3.88	2.43	2.51	4.26
K2O	0.87	0.86	0.13	4.76	0.09	2.01	2.63	2.02	1.02	0.18	1.38	2.18	0.11	1.16	1.41	2.08	1.48	2.13	0.36	0.54	2.6	1.86
Cr2O3	0.002	0.011	0.306	0.04	0.04	0.007	0.004	0.006	0.009	0.039	0.008	0.002	0.016	0.005	0.009	0.005	0.008	0.032	0.041	0.062	0.005	0.002
TiO2	3.03	0.56	0.29	0.42	0.7	0.36	0.38	0.39	0.44	0.7	0.55	0.22	0.97	0.53	0.52	0.39	0.33	0.78	0.68	0.62	0.32	0.3
MnO	0.2	0.04	0.15	0.1	0.1	0.04	0.05	0.05	0.1	0.21	0.04	0.02	0.19	0.32	0.04	0.04	0.04	0.09	0.18	0.19	0.04	0.04
P2O5	0.41	0.11	0.01	0.22	0.31	0.1	0.24	0.13	0.1	0.04	0.13	0.05	0.07	0.17	0.11	0.15	0.09	0.35	0.04	0.04	0.1	0.07
SrO	0.03	0.03	<0.01	0.13	0.09	0.03	0.02	0.04	0.02	0.02	0.03	0.04	0.02	0.01	0.02	0.02	0.03	0.02	0.01	0.01	0.03	0.03
BaO	0.03	0.03	<0.01	0.23	0.12	0.05	0.09	0.06	0.02	0.01	0.04	0.08	0.01	0.03	0.04	0.06	0.06	0.04	0.01	0.01	0.05	0.04
Total	101.41	101.91	99.9	101.34	100.27	101.88	99.19	100.75	99.74	101.56	93.19	101.07	99.21	96.62	99.35	99.82	99.9	98.83	100.28	98.32	98.57	98.55
Ore and accessory metals (ppm)																						
Ag	0.047	0.072	0.015	0.069	0.027	0.033	0.049	<0.002	0.054	0.035	0.044	0.017	0.027	0.673	0.103	0.003	0.018	0.022	0.034	0.095	0.011	0.03
As	2.3	1.4	0.3	1.5	1.4	0.3	7.1	1.2	3.2	0.7	9.2	0.2	1.6	8.1	11.1	0.3	0.9	0.7	1.4	0.3	21.7	4.5
Bi	0.02	0.09	<0.01	0.25	0.06	0.04	0.08	0.02	0.05	0.01	0.04	0.04	<0.01	4.13	0.47	0.02	0.04	0.03	<0.01	0.01	0.03	0.07
Cd	0.145	0.042	0.034	0.062	0.063	0.051	0.041	0.054	0.106	0.105	0.016	0.021	0.041	0.123	0.367	0.048	0.03	0.074	0.085	0.097	0.057	0.045
Co	45.4	16.65	85.1	23.6	29.3	9.87	7.33	10.75	18.5	46.2	15.75	4.51	46.6	20.9	21.7	9.93	8.99	38.5	44.4	47.9	8.82	7.55
Cu	51.3	38.7	16.4	35.1	16.85	6.48	23.6	6.69	27.5	113.5	33.8	6.45	88.6	254	59.4	2.89	23	26.1	137.5	164.5	5.62	13.95
Hg	0.006	<0.005	0.008	0.01	<0.005	<0.005	0.013	0.005	0.021	0.031	0.006	0.005	<0.005	0.057	0.054	<0.005	<0.005	<0.005	0.006	0.037	<0.005	<0.005
In	0.029	0.012	0.023	0.009	0.033	0.006	0.005	0.015	0.025	0.006	0.012	<0.005	0.022	0.036	0.017	0.008	0.013	0.013	0.012	0.007	0.01	0.013
Mo	1.03	0.81	0.06	1.53	0.15	0.17	0.08	0.26	0.54	0.2	0.17	0.09	0.11	28.2	6.55	0.19	0.35	0.15	0.11	0.12	0.43	0.15
Ni	28.9	40.6	1555	129	93.5	27.7	13.9	32.6	61.6	112.5	42.9	4.78	90.3	40.4	49	25.3	27.1	64.7	104.5	118	31.6	12.65
Pb	3.49	4.25	0.85	21.5	6.69	4.26	7.15	6.47	2.58	1.12	2.49	5.01	2.08	28.3	5.93	6.82	7.28	3.43	0.71	0.66	2.86	3.72
Sb	0.11	<0.05	<0.05	0.25	0.05	0.06	0.25	0.23	0.1	<0.05	0.16	0.06	0.22	0.56	0.31	0.06	0.19	0.07	0.07	<0.05	0.06	0.12
Se	0.2	0.2	0.2	<0.2	<0.2	<0.2	<0.2	<0.2	<0.2	0.2	<0.2	<0.2	0.3	1.8	0.6	<0.2	<0.2	<0.2	0.4	0.3	<0.2	<0.2
Sn	2.1	1	<0.5	0.5	1	0.5	0.6	<0.5	0.7	<0.5	0.9	<0.5	<0.5	0.9	1	<0.5	<0.5	1.2	<0.5	<0.5	<0.5	<0.5
Te	<0.01	0.01	0.01	0.01	<0.01	<0.01	0.02	<0.01	<0.01	0.01	0.01	<0.01	0.01	1.64	0.1	<0.01	<0.01	0.01	0.03	0.06	<0.01	0.01
Tl	0.02	0.02	0.14	0.05	<0.02	0.02	0.05	0.02	0.03	<0.02	0.02	0.04	<0.02	0.02	0.02	0.02	0.02	0.02	<0.02	0.02	0.03	0.03
W	1.2	1.2	<0.5	1	<0.5	<0.5	2.7	0.5	<0.5	<0.5	2.7	2.2	0.5	4.9	3.4	<0.5	<0.5	1.3	<0.5	<0.5	<0.5	<0.5
Zn	147.5	74.7	71.9	57.6	81.6	64.2	57.3	68.9	59.7	77.9	70.9	48.2	102	207	205	56.9	40.9	172.5	81.2	78.9	33.1	59.9
Th	4.48	2.88	0.07	3.56	9.11	2.03	13.5	3.79	2.05	0.27	2.6	2.75	0.34	3.12	3.45	3.77	1.57	3.64	0.19	0.21	1.62	1.38
U	1.72	0.79	<0.05	1.12	2.33	0.62	3	0.9	0.65	0.1	0.76	0.99	0.07	0.6	0.88	1.03	0.47	1.12	<0.05	<0.05	0.51	0.4
REEs (ppm)																						
La	25.6	17.6	0.8	30.5	49.9	16.7	83.3	28.1	15.3	2.7	18.4	11.2	3.9	16.6	22.3	26.5	12.8	24.5	2.2	2.1	14.6	11.2
Ce	54.5	34.5	1.9	59.7	101	33.5	159	54.3	30.8	6.8	32.1	20.9	9.5	32.5	42.4	53.9	27.3	50.1	5.9	5.5	30.6	20.8
Pr	7.35	3.99	0.34	7.86	12.75	4.3	19.15	6.63	3.88	1.1	3.9	2.4	1.5	3.94	4.93	7.01	3.32	6.57	1	0.91	3.86	2.48
Nd	33.8	15.6	1.5	33.4	47.7	17.2	69.4	25.5	14.6	5.5	14.9	9.7	7.2	16.1	18.6	28	14	28.1	5.1	4.5	15.6	9.3
Sm	8.1	3.21	0.67	6.77	7.14	2.69	10.6	3.6	2.53	1.83	3.01	1.72	2.46	2.98	3.5	4.66	2.63	5.7	1.56	1.58	2.78	1.68
Eu	2.24	0.76	0.23	1.6	1.69	0.8	2.64	0.92	0.76	0.6	0.92	0.44	0.78	0.92	0.85	1.23	0.66	1.42	0.56	0.52	0.72	0.68
Gd	7.88	2.76	0.89	4.24	4.44	1.94	6.71	1.99	2.76	2.39	2.49	1.21	3	2.82	2.77	2.74	1.58	3.9	2.08	1.94	1.7	1.31
Tb	1.15	0.41	0.16	0.56	0.62	0.24	0.74	0.26	0.38	0.4	0.39	0.12	0.52	0.41	0.4	0.3	0.21	0.46	0.36	0.38	0.19	0.19
Dy	6.81	2.48	1.06	2.74	2.79	1.1	3.49	1.13	2.2	2.75	2.16	0.68	3.51	2.42	2.42	1.47	1.03	2.11	2.4	2.41	0.8	0.92
Ho	1.38	0.44	0.25	0.49	0.53	0.2	0.54	0.22	0.47	0.68	0.44	0.09	0.85	0.51	0.44	0.27	0.19	0.43	0.56	0.55	0.19	0.19
Er	3.69	1.4	0.6	1.27	1.46	0.57	1.46	0.51	1.24	1.87	1.19	0.29	2.29	1.52	1.37	0.57	0.41	1.15	1.42	1.69	0.38	0.56
Tm	0.51	0.15	0.09	0.2	0.19	0.06	0.18	0.06	0.18	0.26	0.16	0.04	0.31	0.2	0.18	0.08	0.07	0.18	0.26	0.24	0.06	0.06
Yb	3.39	1.19	0.73	1.13	1.13	0.43	1.33	0.51	1.14	1.97	1.06	0.27	2.2	1.43	1.23	0.52	0.44	1.3	1.76	1.61	0.36	0.35
Y	36.6	12.5	6.3	13.4	13.8	5.6	16.1	5.6	11.8	16	11.7	3	21	13.9	11.6	7	5.3	11	14.3	14.3	3.9	5
Lu	0.51	0.18	0.12	0.17	0.18	0.07	0.2	0.06	0.2	0.27	0.18	0.04	0.38	0.25	0.2	0.09	0.07	0.22	0.3	0.23	0.07	0.06
HFSEs (ppm)																						
Zr	190	161	18	106	147	119	239	112	132	42	143	101	61	126	172	117	105	92	40	35	103	101
Hf	4.92	3.92	0.51	2.75	3.92	3.07	5.68	2.79	3	1.09	3.39	2.77	1.63	3.08	3.99	2.86	2.73	2.31	1.14	0.94	2.74	2.4
Nb	23.3	6.11	0.49	3.76	7.91	2.98	7.62	2.24	5	1.5	5.65	1.82	2.51	6	6.48	2.41	2.59	3.57	1.46	1.34	1.8	2.92
Ta	1.4	0.5	<0.1	0.2	0.6	0.2	0.4	0.1	0.3	0.1	0.4	0.1	0.1	0.4	0.6	0.1	0.2	0.2	0.1	0.1	0.1	0.2
LILEs (ppm)																						
Li	18.6	12.3	14.2	6.4	70.5	19.2	4.4	12.1	25.1	13	24.3	8.5	34.2	59.7	20.8	21.4	9.2	128.5	30.1	11.7	16.6	26.9
Cs	0.46	1.7	4.9	0.76	0.23	2.14	3.27	1.48	0.46	0.26	1.51	1.38	0.33	2.27	1.68	2.69	1.77	2.31	1.08	0.85	1.45	1.47
Rb	21.1	27.7	11.6	57.9	2.3	46.2	75.3	48.8	25.3	6.3	39.5	55.6	2.8	37.2	42.2	51.7	38.9	52.8	10.5	19.4	56.2	43.4
Sr	239	287	12.2	1105	767	212	186	309	176.5	164.5	234	387	167	149.5	212	178	235	169.5	112	133.5	245	278
Ba	288	328	16	2170	1075	437	866	577	196	136	354	782	49.8	262	396	577	575	386	104.5	50.9	469	392
Other (ppm)																						
Cr	18	82	2220	288	283	52	27	42	58	283	55	11	117	35	65	36	60	229	297	438	40	18
Ga	21.2	18.7	6.6	15.3	18	20.3	21.5	19.8	15.8	14.5	17.8	23	16.4	17.6	21.7	20.3	17.9	22.9	14.4	13.3	18.8	19.1
Ge	1.5	0.9	1.1	1	1.1	0.9	1.1	0.8	0.6	1.5	0.9	0.8	1.3	1.1	0.8	0.9	0.8	1.2	1.3	1.4	0.9	0.8
Sc	37.7	10.4	21.1	14.35	18.35	6.74	5.54	7.03	13.35	41.5	10.95	2.8	36.9	18.45	14.65	6.74	7.53	28.4	45.4	49.9	5.28	5.11
Re	0.001	<0.001	<0.001	<0.001	<0.001	<0.001	<0.001	<0.001	<0.001	0.001	<0.001	<0.001	<0.001	0.002	<0.001	<0.001	<0.001	<0.001	<0.001	0.001	<0.001	<0.001
V	483	87	117	190	152	58	68	73	94	286	227	27	306	100	99	66	58	224	278	271	52	41

Abbreviations: REE=rare earth elements; HFSE=high field strength elements, LILE=large ion lithophile elements

Table 3: Volcanic rock petrographic notes, interpretations, and photos (Swayze, Dore, and Garnet townships, Abitibi Greenstone Belt; Figures 3 & 4).

Sample	Mineral 1:	Notes (Habit, alteration etc):	Modal %:	Mineral 2	Notes (Habit, alteration etc):	Modal %:	Mineral 3	Notes (Habit, alteration etc):	Modal %:	Mineral 4	Notes (Habit, alteration etc):	Modal %:	Mineral 5	Notes (Habit, alteration etc):	Modal %:	Mineral 6	Notes (Habit, alteration etc):	Modal %:	Rock Type	Comments	Photos
22AB064A	Plagioclase	Brownish grey (PPL), Quite altered, lathey larger crystals than the rest (up to 2500 microns), penetration twins, albite twins. Some forming skinny acicular crystals, high undercooling.	50	Clinopyroxene	Medium-light brown (PPL), second order colours, some blocky and well formed, other irregular and anhedral. Inclined extinction. Seems to be the dominant mineral altering to chlorite	25	Quartz	Occurs interstitially producing granoblastic texture with other qz grains. Commonly near/associated with calcite. Appears to have grown in some sort secondary porosity that developed post lithification.	5	Calcite	Forms large monocrystalline masses filling in interstitial spaces like Qz. Good cleavage, high order colours	<5	Hornblende	Rare small euhedral crystals, lighter brown than Cpx. 60/140 crystals. Observerd crystals are no altered.	1	Chlorite	Anhedral, alteration/metamorphic product of cpx	15	Gabbro	Relatively fine grained gabbro or medium grained basalt. Porosity created by dissolution not mechanical. Maybe just related to retrograde metamorphism/uplift.	
22AB066A	Quartz	Zone 1: cryptocrystalline-fine grained (75 microns) forming the groundmass with glass. Zone 2: also probably forming the groundmass, and also occurs as occasional large anhedral crystals (possibly fractured).	50-60	Plagioclase	Zone 1: Plagioclase is quite altered (pictured below, I cant remember what its called). Mostly anhedral. 500 microns-700 microns. Albite twinning. Zone 2: Plagioclase is more euhedral and less altered. More abundant pheocrysts.	35	?	Seems like an alteration product. Pleochroic, colourless-grey. 3rd-4th order interference colours. Patchy-wormy, intergrown with plag.	5	Chlorite	Patchy, might be occuring along fractures.	5							Plagioclase-phyric fragmental dacite	Composed of two main textures. One of the zones is likely a fragment hosted in the other but it is not immediately clear which is which. Zone 1 has **moslty** larger and more altered pl phenocrysts, and a less glassy groundmass. Zone 2 still has large pl phenos, but has a large contingent of smaller, euhedral, and less altered pl phenos. In some areas of zone 2 the groundmass might be entirely pl + aphanitic qz. Zone 2 might have less qz than zone 1, but it is hard to tell because it is more aphanitic. In some areas the divide between zones is clear and others the boundary is more diffuse.	
22AB069SS	Olivine	In most places this is completely replaced to serpentine. 4-7 sided equant blocks. Straight cracks running through cummulate crystals are filled with an opaque mineral. In between cummulate olivine spinifex textured olivine forms radiating-subparallel arrays or randomly oriented pockets. Often intergrown.	100																Komatiite	Cumulate of euhedral olivine crystals that have altered to serpentine and some chlorite. Interstitial spinifex textured similarily altered olivine	
22AB075A	Biotite	Believe it is high Mg biotite. Weakly pleochroic, Cream coloured to pale green. Oriented with Z/Y axis perpendicular to stage. Second to low third order interference colours. About 50% of it has altered to chlorite and sericite. Occurs as pinching and swelling, anastomosing splintery lathes that bend around more resistant phases (i.e.kfs/qz).	30	Amphibole	Well formed euhedral crystals. High relief. Strongly pleochroic, pale yellowish brown to dark green/olive. Good cleavage. First order interference colours. Carlsbad twinning. Tends to occur near biotite but is more resistant to alteration than biotite.	3	Calcite	Variety of grain sizes, often appears as small grains cementing larger calcite crystals together. Often occurs in strain shaows of kfs crystals/possibly quartz. Occurs within fractured kfs crystals. Likely a late component.	17	Quartz	occurs as vfg groundmass and thin bands in between biotite crystals.	50							Andesitic tuff breccia-lapilli tuff	Strong foliation. Strain shadows around quartz-rich lapilli. Unclear how much qz there is due to grainsize, but I think there is quite a lot.	
22AB081A	Chlorite/biotite	Weakly aligned with other grains. Light green to pale yellow.	20	Plagioclase	Well formed euhedral - subhedral crystals, often with smaller calcite crystals rimming them. Albite twinning.	40	Quartz		30										Dacite-andesite	On the felsic end of andesite or possibly dacite. Chlorite/biotite defines a weak foliation. Slide not perferctly flat.	
22AB081B	Plagioclase	Forms large (up to 1800 microns) heavily sericitized (Maybe 50-60%) pheoncrysts. Sometimes occurs in aggregates. Also occurs as the groundmass as ~125 micron irregular aggregates of smaller crystals.	70	Quartz	Small crystals in the groundmass and filling interstitial spaces. Also in fractures as reprecipitated qz or later veining.	20	Calcite	Occures in fractures with quartz	10										Plagioclase-phyric fragmental dacite	Dominated by plagioclase and quartz, heavily sericitized. Plag-phyric dacite, I think it is a fragmental flow.	
22AB086A	Quartz	Lapillis are dominated by quartz crystals (50-100 microns) dissorderly arranged. Sometimes surrounding plag crystals. Sometimes appears recrystallized with granoblastic texture possibly in pore spaces post eruption.	75	Plagioclase	Mostly equant and often fractured. Commonly occurs as monomineralic aggregates. Surprisinly weakly altered.	20	Muscovite	Forms large (up to 2500 micron) phenocrysts. Sericite and chlorite alteration occuring along cleavage planes.	5										Rhyodacitic lapilli tuff-crystal tuff	Sericitized felsic lapilli tuff with significant crystal components in places. Don't see ksp so on the dacitic side of things. Sericite concentrated along margins of lapillis. Local chlorite and ankerite alteration/flooding.	
22AB091A	Quartz	Occurs as the groundmass (with plag) and occasional qz eyes	40	Plagioclase	Phenocrysts. Individual crystals up to 2500 microns, aggregates larger.	50	Lithic fragment or musc			Calcite and sericite	Sericite is pervasive, calcite patchy. Both occur along fractures.	10							Plagioclase-phyric fragmental dacite	Sericitized fragmental plag-phyric dacite. Dominated by quartz and plag with small randomly oriented sericite peppered throughout.	
22AB093A	Quartz	Quartz eyes and as small crystals in the groundmass. Hard to tell how much is in the groundmass.	~15	Plagioclase	Dominates the rock. Cryptocrystalline in the groundmass and also forms heavily sericitized and calcite-replaced phenocrysts	70	calcite		15										Fragmental andesite	Fragmental dacite-andesite? Hard to tell how much qz there it. I am assuming that the groundmass is mostly plag as it is not as white and clear as the qz phenos, but that could just be because it is vfg and has been masked by the sericite alteration. EDIT: Fragmental andesite after looking at chemistry (54wt% SIO2)	
22AB095A02	Plagioclase	Essentially all of the rock. Acicular haystack of randomly oriented crystals. Cannnot tell what it is altering to, something with higher first order interference colours. Maybe just chlorite looking weird.	90																Basalt	Basalt, I guess! Might plot as an anorthosite actually. Strange "spinifex-like" plagioclase crystals. Almost entirley altered to/replaced by chlorite	
22AB098A02	Plagioclase	well formed euhdral crystals	45	Quartz	occurs as finegrained matrix	50													Fragmental dacite	Fragmental volcanic composed to two slightly different lithologies, I think. The one I believe is acting as the "matrix" is dominated by pl phenocrysts and has a higher portion of glass in the matrix . The "clast" is still dominated by Pl I believe, and has less glass. Both would probably be on the qz poor side of dacite.	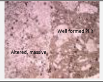
22AB101A02	Quartz	Makes up the majority of the groundmass (~50 microns) and occurs as phenocrysts/qz eyes (up to 2500micron).	70	Plagioclase	Mainly occurs as large ~1500 mircon phenocrysts. Sometimes as aggregates.	30													Rhyolite	Relatively massive/unfractured comparaed to other samples. Qz-pl-phyric Dacite-rhyolite. No Kfs. Probably a subvolcanic intrusion, we leaned on the side of intrusive in the field. Moderate sericite alteration, little to no chlorite. Rhyolite.	
22AB122A02	k-feldspar	Large (~2000 microns) interlocking crystals and smaller ~500 micron crystals making up most of the rock.	50	cpx	blocky masses, brown-beige in ppl. Second order pink green yellow in xpl. High relief.	20	Quartz	mainly occurs as veins associated with calcite. Also as small inclusions in ksp.	20	calcite	occurs as veins	10							Andesite	Dominated by ksp and cpx. Some qz grain inclusions in ksp as well as in interstitial spaces. Maybe a qz trachyte mineralogically? Late qz-calcite veins which seem to control chlorite alteration of nearby material.	
22AB123A02	Plagioclase	Interpreted to be pl but not sure. No fresh crystals present just places where the crystal has been dissolved and qz has reprecipitated in its cast or sericite.	30	quartz	aphanitic groundmass and phenocrysts	60													Fragmental dacite-andesite	Weak foliation. Fragmental andesite(?) or very altered intm lapilli tuff? plagioclase phenocrysts have been replaced by fg qz or altered to chl and ser. Qz eyes still preserved. Many euhedral pyrite grains.	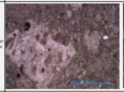 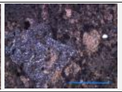
22AB124A02	Plagioclase	forms large (1900 micron) to smaller (125 micron) phenocrysts. Angular and fractured looking to euhedral. Variably sericitized . In some fragments pl may also form a significant component of the groundmass.	30	Quartz	Makes up the fg groundmass of all fragments. Fragments can be differentiated by coarseness of qz groundmass and amount of pl phenos	60													Fragmental dacite	Fragmental, possibly autoclastic dacite. Some fragments might be considered andesitic, but it is hard if the groundmass if pl or qz. Maybe the product of a fractionated magma chamber that erupted and phases of similar density stayed together but were ultimatley incorporated into the same rock. Chlorite flooding/alteration has replaced part of the groundmass and left surprisingly unaltered pl phenos.	
22AB134A02	Quartz	Groundmass material along with what is not calcite and sericite.	50	Plagioclase	Some remnant phenocrysts still show albite twinning. Heavily sericitized.	20													Plagioclase-phyric dacite	Heavily sericitized, relativley equigranular and massive. Alteration is clouding much of the original mineralogy, but qz is a major phase so I would lean towards dacite rather than andesite. Some remnant pl phenocrysts. Pl-phyric massive dacite flow.	
22AB135A02	Quartz	Groundmass of all fragments (finer grained) as well as interfragment material (coarser grained).	55	Plagioclase	Large ~2600micron to smaller ~150micron phenocrysts.	45													Rhyodacitic lapilli tuff	Fragments are the same or very close lithology as each other, seperated by qz rich matrix. Rhyodacitic	
22AB140A02	Plagioclase	Very difficult to identify primary mineralogy. Definelty plag present	40	Biotite	altered to chlorite completely	15	aphanitic sericized groundmass	too altered and fg to identify	45										Basalt	Severly altered by ser, chl and cal. Possibly fragmental? Or just calcite progressivley replacing regions creating islands of non-calcite material. Some equant unknown phenocrysts growth zoning. Low SiO2 , definetly basalt	
22AB145A02	Plagioclase	Interlocking randombly oriented grains avg around 600 microns.	75	Cpx	Euhedral, some crystals zoned as below (might be cool to SEM) less abundant that plag. Carlsbad twinning.	25													Basalt	Massive, relativley fresh samples. Definelty basalt or subvolcanic equivalent. SAMPLE IS NOT CONSISTENT THICKNESS. Cpx shows first order colours in center of slide and second order on the outside.	
22AB165A02	Plagioclase	Forms phenocrysts as well as likely the groundmass material. Hard to positively identify but a couple preserved crystals still show twinning. Most crystals are serverly sericite and calcite altered.	80	quartz	surprising amount of qz phenocryts for how low the SiO2 content is . Fractured/cupped to rounded phenocrysts max 750 microns, moslty smaller than pl phenos	20													Andesite	Very sericitized, massive, pl-qz-phyric. Andesite. Almost seems like an anorthosite with qz forming late	
22AB171A02	Quartz	I suspect it is making up most of the groundmass. Also occurs as small quartz eyes (100 microns).	20 identifiable, although I suspect it is much higher but vfg in the groundmass and unidentifiable.	Plagioclase	Elongate pheocrysts alligned with one another up to 2000 microns long. Very very thin albite twinning.	35													Rhydacitic crystal-lapilli tuff	Bedded felsic crystal-lapilli tuff. Calcite alteration is concentrated in the plag phenocrysts. Sericite is throughout.	
22AB172A02	Clinopyroxene	Cracked crystals, grain margins seem fractured and resorbed by groundmass. Ophitic-subophitic texture with altered plagioclase	40	Plagioclase	Almost entirley altered, hard to distinguish individual grains. Commonly penetrates into Cpx crystals.	30	Quartz	disseminated throughout forming the residual matrix of the rock.	30										Fragmental basalt	Not like other samples; similar to 145. Fragmental mafic volcanic.	

Table 4a: Mineralized sample data and geochemistry

All samples taken from station 22AB130 (0378624 E, 5293481 N UTM Zone 17T). Relative location within the occurrence shown in main text (Figure 9A).

		Key base metals (ppm)													Precious metals (ppm)	
Sample	**Type**	**Cu**	**Zn**	**Pb**	**Ni**	**Mo**	**Ta**	**Nb**	**W**	**Co**	**Bi**	**Cd**	**Cr**	**V**	**Au**	**Ag**
22AB130A**01**	Host rock	137.5	73	10.1	96.5	12.95	<0.01	0.05	0.14	9.5	7.76	0.24	17	29	0.02	2.3
22AB130A**03**	Po-dominated, Cross section	651	171	8.7	175	13.6	<0.01	0.21	0.86	11.4	8.06	1.08	9	17	<0.02	1.61
22AB130A**05**	Po-dominated, Cross section	260	129	22.8	44.5	4.28	<0.01	<0.05	0.17	13.8	7.3	0.59	5	7	<0.02	2.71
22AB130A**08**	Po-dominated, Cross section	293	195	16.4	51.1	7.25	<0.01	0.09	0.15	41.5	10.35	0.9	7	5	<0.02	2.95
22AB130A**10**	Po-domianted	324	215	11.3	40.2	9.14	<0.01	<0.05	0.21	87.8	6.7	0.99	6	10	<0.02	2.02
22AB130A**16**	Host rock	77.8	2300	2.7	207	204	<0.01	<0.05	4.18	60.6	0.83	10.45	17	22	<0.02	0.67
22AB130A**20**	Po-dominated	295	365	10.6	37.7	173.5	<0.01	<0.05	0.47	49.5	25.4	1.98	6	8	<0.02	2.98
22AB130A**23**	Py-dominated	247	85	22.6	40.6	19.95	<0.01	<0.05	1.43	77.5	5.6	0.43	10	21	0.02	3.37
22AB130A**24**	Py-dominated	163.5	53	24.7	52.7	42.5	<0.01	<0.05	0.95	149	15.55	0.1	10	23	0.03	5.04
22AB130A**27**	Po-dominated	417	173	10.2	60.2	36.9	<0.01	0.08	0.33	45.9	7.07	1.55	4	8	<0.02	3.21

	Other elements													
Sample	**Al %**	**As (ppm)**	**B (%)**	**Ba (ppm)**	**Be (ppm)**	**Ca (%)**	**Ce (ppm)**	**Cs (ppm)**	**Fe (%)**	**Ga (ppm)**	**Ge (ppm)**	**Hf (ppm)**	**Hg (ppm)**	**In (ppm)**
22AB130A**01**	1.17	0.8	<10	20	0.12	0.13	9.44	0.55	11.05	5.34	0.16	0.53	0.01	0.006
22AB130A**03**	1.07	0.5	<10	10	0.15	0.08	6.41	0.28	41.4	3.36	0.17	0.25	0.02	0.036
22AB130A**05**	0.86	1.6	<10	20	0.08	0.06	5.49	0.14	35.7	2.8	0.11	0.33	0.01	0.01
22AB130A**08**	0.65	0.7	<10	20	0.09	0.03	3.5	0.26	32.9	1.69	0.14	0.31	0.01	0.019
22AB130A**10**	0.82	2	<10	20	0.1	0.06	5.84	0.23	34.5	2.59	0.13	0.25	0.01	0.015
22AB130A**16**	0.99	93.3	<10	30	0.25	2.91	24.2	0.62	4.57	5.04	<0.05	0.38	0.13	0.338
22AB130A**20**	0.69	2.5	<10	20	0.11	0.16	5.01	0.23	33.4	2.13	0.13	0.19	0.02	0.05
22AB130A**23**	2.99	75.8	<10	10	0.27	0.04	4.03	0.17	31	9.2	0.24	0.25	0.02	0.029
22AB130A**24**	2.67	86.1	<10	<10	0.25	0.21	3.85	0.17	30.4	8.34	0.43	0.19	0.01	0.015
22AB130A**27**	0.96	1.9	<10	10	0.1	0.05	4.6	0.15	37.3	2.65	0.15	0.19	0.02	0.024

	Other elements																				
Sample	**K (%)**	**La (ppm)**	**Li (ppm)**	**Mg (%)**	**Mn (ppm)**	**Na (%)**	**P (ppm)**	**Rb (ppm)**	**Re (ppm)**	**S (%)**	**Sb (ppm)**	**Sc (ppm)**	**Se (ppm)**	**Sn (ppm)**	**Sr (ppm)**	**Te (ppm)**	**Th (ppm)**	**Ti (%)**	**Tl (ppm)**	**U (ppm)**	**Y (ppm)**
22AB130A**01**	0.12	4.1	13	0.37	213	0.04	320	4.4	0.005	6.05	0.09	2.4	5.1	0.4	3.4	3.23	1.1	0.008	0.22	0.21	2.75
22AB130A**03**	0.06	3.1	18.8	0.18	146	<0.01	180	2	0.004	9.67	0.07	1.6	13	1.3	1.4	1.48	0.3	0.025	0.12	0.08	1.75
22AB130A**05**	0.07	2.4	10.3	0.27	111	0.01	140	2.1	0.003	>10.0	0.26	0.9	6.1	0.3	1.4	0.97	0.4	<0.005	0.37	0.09	1.27
22AB130A**08**	0.09	1.6	7.1	0.12	78	0.02	110	2.9	0.002	>10.0	0.13	1.1	13.2	0.5	3.9	1.9	0.5	<0.005	0.26	0.13	1.06
22AB130A**10**	0.07	2.5	10.1	0.2	127	0.02	100	2.3	0.002	>10.0	0.11	1.2	9.5	<0.2	2.1	1.36	0.4	<0.005	0.18	0.08	1.26
22AB130A**16**	0.18	11.9	9.9	0.29	258	0.05	350	6.2	0.033	2.07	0.14	3.9	1.5	0.8	41.6	0.36	1.5	<0.005	0.32	0.29	4.68
22AB130A**20**	0.1	2.5	6.8	0.09	101	0.01	110	3.2	0.02	>10.0	0.14	1	16.2	0.4	2.7	12.8	0.4	<0.005	0.21	0.09	1
22AB130A**23**	0.03	2	19	0.29	150	<0.01	160	1.2	0.001	>10.0	2.51	2.8	12.2	0.7	2.5	2.56	0.4	<0.005	0.05	0.07	1.2
22AB130A**24**	0.01	2	17.2	0.35	174	<0.01	130	0.3	0.002	>10.0	1.86	2.8	15.7	0.2	6.2	4.96	0.3	0.005	0.05	0.06	1.16
22AB130A**27**	0.07	2.2	13.2	0.09	133	0.01	100	2.5	0.003	>10.0	0.1	1.2	12.1	0.3	1.5	2.57	0.3	0.006	0.1	0.06	0.89

Table 5: CA-TIMS zircon U-Pb isotopic data.

										Radiogenic Isotope Ratios								Isotopic Dates										
			Th	^{206}Pb*	mol %	Pb*	Pb$_c$	Pb*	^{206}Pb	^{208}Pb	^{207}Pb		^{207}Pb		^{206}Pb		corr.	^{207}Pb		^{207}Pb		^{206}Pb		include in				
Sample	Tracer	LA-ICPMS	U	x10^{-13} mol	^{206}Pb*	(pg)	(pg)	Pb$_c$	^{204}Pb	^{206}Pb	^{206}Pb	% err	^{235}U	% err	^{238}U	% err	coef.	^{206}Pb	±	^{235}U	±	^{238}U	±	weighted mean?	***Weighted Mean Calculations***			
(a)	solution	spot label	(b)	(c)	(c)	(c)	(c)	(c)	(d)	(e)	(e)	(f)	(e)	(f)	(e)	(f)		(g)	(f)	(g)	(f)	(g)	(f)		***95% confidence interval***			
93HNB-206B																												
z6	ET2535	336-338	0.223	9.7354	99.96%	250.7	0.34	747	43433	0.062	0.187379	0.019	13.522103	0.045	0.523622	0.032	0.941	2718.55	0.31	2716.83	0.42	2714.52	0.70					
z1	ET2535	324-326	0.268	17.5598	99.99%	456.8	0.15	3033	174589	0.074	0.187228	0.019	13.493903	0.045	0.522952	0.031	0.934	2717.22	0.32	2714.86	0.42	2711.69	0.69					
z5	ET2535	340-342	0.403	9.3727	99.98%	251.0	0.19	1351	75546	0.111	0.186739	0.015	13.471109	0.044	0.523435	0.031	0.974	2712.91	0.25	2713.26	0.41	2713.73	0.69					
z2	ET2535	343-344	0.280	1.4878	99.90%	38.7	0.13	302	17364	0.077	0.185143	0.019	13.241937	0.063	0.518965	0.054	0.959	2698.75	0.32	2697.05	0.60	2694.79	1.18					
z3	ET2535	327-328	0.176	5.9465	99.97%	151.1	0.16	973	57367	0.049	0.183817	0.019	13.079897	0.043	0.516312	0.030	0.938	2686.87	0.31	2685.43	0.41	2683.52	0.65					
95HNB-0273																												
z6	BSU1B	407	0.481	2.0432	99.91%	55.5	0.15	362	19956	0.133	0.184480	0.064	13.181338	0.133	0.518447	0.077	0.952	2692.82	1.06	2692.72	1.25	2692.59	1.69	x	207Pb/206Pb ± random [+decay constant]		MSWD =	0.4
z3	BSU1B	378	0.458	2.0311	99.93%	54.9	0.12	470	26005	0.127	0.184468	0.062	13.174910	0.131	0.518227	0.075	0.959	2692.72	1.03	2692.26	1.23	2691.66	1.66	x	**2692.46**	**± 0.64** [2.36]	pof =	0.77
z4	BSU1B	383	0.480	2.6488	99.94%	72.0	0.13	535	29512	0.133	0.184439	0.062	13.142203	0.151	0.517023	0.108	0.941	2692.45	1.02	2689.92	1.43	2686.54	2.36	x			n =	5
z2	BSU1B	411	0.492	2.6832	99.94%	73.1	0.13	569	31300	0.136	0.184436	0.062	13.160446	0.133	0.517750	0.080	0.950	2692.42	1.03	2691.22	1.25	2689.63	1.75	x				
z1	BSU1B	380	0.528	2.1252	99.92%	58.3	0.15	395	21542	0.146	0.184379	0.063	13.158527	0.141	0.517833	0.091	0.942	2691.92	1.04	2691.09	1.33	2689.98	2.00	x				
22AB066A02																												
z5	ET2535	237-238	0.472	2.2773	99.92%	61.9	0.15	402	22151	0.131	0.186120	0.019	13.372865	0.066	0.521347	0.057	0.962	2707.43	0.31	2706.34	0.62	2704.89	1.26	x	207Pb/206Pb ± random [+decay constant]		MSWD =	0.8
z2	ET2535	178-180	0.426	2.7041	99.93%	72.7	0.15	489	27263	0.118	0.186111	0.020	13.377049	0.059	0.521534	0.049	0.952	2707.35	0.32	2706.64	0.56	2705.68	1.09	x	**2707.24**	**± 0.17** [2.33]	pof =	0.52
z3	ET2535	176-177	0.508	0.9837	99.82%	26.9	0.15	179	9830	0.141	0.186106	0.021	13.383744	0.079	0.521808	0.071	0.967	2707.31	0.35	2707.11	0.75	2706.85	1.57	x			n =	6
z1	ET2535	172-173	0.520	4.7705	99.94%	130.9	0.25	515	28110	0.144	0.186092	0.019	13.372930	0.057	0.521426	0.046	0.951	2707.19	0.32	2706.35	0.54	2705.23	1.02	x				
z4	ET2535	170-171	0.421	1.8337	99.90%	49.3	0.16	311	17326	0.116	0.186084	0.020	13.372976	0.061	0.521451	0.051	0.951	2707.11	0.33	2706.35	0.57	2705.33	1.12	x				
z6	ET2535	229-230	0.450	2.9938	99.90%	81.0	0.25	328	18199	0.125	0.186077	0.020	13.373468	0.054	0.521491	0.042	0.943	2707.05	0.33	2706.39	0.51	2705.50	0.93	x				
22AB101A02																												
z2	ET2535	21-22	0.449	1.0952	99.87%	29.6	0.12	248	13769	0.124	0.186181	0.020	13.368922	0.061	0.521022	0.051	0.949	2707.97	0.34	2706.06	0.58	2703.51	1.12					
z1	ET2535	1-2	0.631	1.1331	98.39%	31.8	1.53	21	1124	0.175	0.186118	0.077	13.374499	0.232	0.521415	0.206	0.945	2707.41	1.27	2706.46	2.19	2705.18	4.56					
z6	ET2535	none	0.504	0.8366	99.80%	22.9	0.14	166	9083	0.140	0.185609	0.017	13.319815	0.096	0.520707	0.090	0.986	2702.89	0.28	2702.59	0.91	2702.18	1.98					
z7	ET2535	35	0.395	0.7137	99.80%	19.0	0.12	163	9158	0.109	0.184057	0.022	13.121224	0.078	0.517268	0.070	0.964	2689.03	0.36	2688.41	0.74	2687.58	1.53					
z4	ET2535	none	0.394	0.5221	99.69%	13.9	0.14	103	5805	0.109	0.184008	0.028	13.114331	0.128	0.517136	0.122	0.976	2688.58	0.47	2687.91	1.21	2687.02	2.67					
z5	ET2535	19-20	0.385	0.6871	99.80%	18.3	0.12	159	8945	0.107	0.183948	0.022	13.112842	0.121	0.517245	0.115	0.983	2688.05	0.37	2687.81	1.14	2687.48	2.54					
22AB123A02																												
z1	ET2535	300	0.623	2.4509	99.90%	68.7	0.20	341	18227	0.172	0.186192	0.019	13.369715	0.056	0.521021	0.046	0.954	2708.07	0.31	2706.12	0.53	2703.51	1.01	x	207Pb/206Pb ± random [+decay constant]		MSWD =	1.7
z4	ET2535	266-267	0.463	1.9673	99.86%	53.3	0.24	226	12524	0.128	0.186175	0.019	13.385383	0.125	0.521680	0.120	0.989	2707.92	0.31	2707.23	1.18	2706.30	2.65	x	**2707.82**	**± 0.19** [2.34]	pof =	0.16
z5	ET2535	268-269	0.457	2.5121	99.91%	68.0	0.18	379	20970	0.126	0.186168	0.020	13.346964	0.050	0.520201	0.038	0.933	2707.86	0.34	2704.51	0.47	2700.03	0.83	x			n =	5
z2	ET2535	298-299	0.555	2.8649	99.88%	79.2	0.28	286	15507	0.154	0.186151	0.019	13.366538	0.058	0.521013	0.048	0.952	2707.70	0.32	2705.90	0.55	2703.48	1.06	x				
z3	ET2535	294-295	0.543	3.0738	99.90%	84.8	0.27	318	17311	0.150	0.186135	0.018	13.375464	0.053	0.521404	0.042	0.958	2707.57	0.29	2706.53	0.50	2705.13	0.93	x				
22AB124A02																												
z3	ET2535	60-62	0.546	2.4730	99.93%	68.2	0.13	510	27677	0.151	0.186175	0.024	13.373871	0.053	0.521232	0.041	0.906	2707.92	0.39	2706.41	0.50	2704.40	0.90	x	207Pb/206Pb ± random [+decay constant]		MSWD =	0.9
z4	ET2535	49-51	0.528	3.8678	99.96%	106.3	0.13	841	45806	0.146	0.186174	0.019	13.382219	0.049	0.521558	0.037	0.939	2707.91	0.32	2707.00	0.46	2705.78	0.81	x	**2707.74**	**± 0.18** [2.33]	pof =	0.47
z2	ET2535	68-69	0.588	0.8267	99.79%	23.0	0.15	158	8530	0.163	0.186172	0.027	13.351719	0.091	0.520376	0.082	0.957	2707.89	0.45	2704.85	0.86	2700.77	1.80	x			n =	6
z5	ET2535	89-90	0.481	2.0471	99.91%	55.7	0.16	353	19452	0.133	0.186148	0.019	13.381502	0.049	0.521604	0.037	0.940	2707.68	0.32	2706.95	0.46	2705.98	0.81	x				
z1	ET2535	73-75	0.428	3.7094	99.96%	99.8	0.14	737	41037	0.118	0.186147	0.019	13.377335	0.052	0.521444	0.041	0.947	2707.67	0.31	2706.66	0.49	2705.30	0.90	x				
z6	ET2535	52-54	0.496	4.5922	99.97%	125.4	0.12	1008	55303	0.137	0.186131	0.019	13.376461	0.042	0.521454	0.028	0.940	2707.53	0.31	2706.60	0.40	2705.34	0.61	x				

(a) z1, z2, etc. are labels for analyses composed of single zircon grains that were annealed and chemically abraded (Mattinson, 2005).

(b) Model Th/U ratio calculated from radiogenic 208Pb/206Pb ratio and 207Pb/235U date.

(c) Pb* and Pbc are radiogenic and common Pb, respectively. mol % ^{206}Pb* is with respect to radiogenic and blank Pb.

(d) Measured ratio corrected for spike and fractionation only. Fractionation correction for analyses done with tracer solution BSU1B is 0.18 ± 0.03 (1 sigma) %/amu (atomic mass unit) for single-collector Daly analyses, based on analysis of EARTHTIME 202Pb-205Pb ET2535 tracer solution. Fractionation correction for analyses done with tracer solution ET2535 is based on measurement of 202Pb/205Pb in the tracer solution.

(e) Corrected for fractionation and spike. Common Pb in zircon analyses is assigned to procedural blank with composition of 206Pb/204Pb = 18.04 ± 0.61%; 207Pb/204Pb = 15.54 ± 0.52%; 208Pb/204Pb = 37.69 ± 0.63% (1 sigma). 206Pb/238U and 207Pb/206Pb ratios corrected for initial disequilibrium in 230Th/238U using a D(Th/U) of 0.20 ± 0.05 (1 sigma).

(f) Errors are 2 sigma, propagated using algorithms of Schmitz and Schoene (2007) and Crowley et al. (2007).

(g) Calculations based on the decay constants of Jaffey et al. (1971). 206Pb/238U and 207Pb/206Pb dates corrected for initial disequilibrium in 230Th/238U using a D(Th/U) of 0.20 ± 0.05 (1 sigma).

Table 6: U-Pb geochronologic analyses and trace element concentrations.

Zircon_19Jan23_Bayers_2

2717.2, 2698.7, 2686.9, 2712.9, 2718.5 feeder porphyry Shunsby to Blake River (vs. 2699 no ref)

Youngest age is 2686.9, thus this is firmly mid Porcupine-age porphyry and not related to Blake River

2692.46 +/- 0.64 Ma Felsic ash tuff, Swayze Road (van Breemen et al. dated at 2696 +/- 2)

This is a tight age. Must be transitional unit between UBR and Porcupine. Compositionally looks like 66, or antecryst 1 of 123, 124

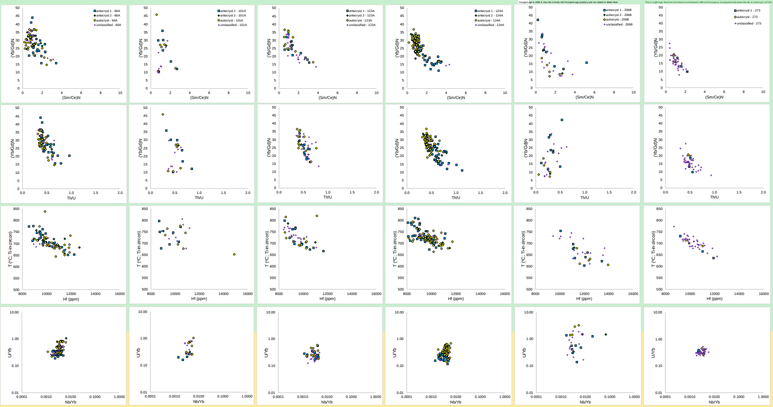
■ antecryst 1 - 66A
◆ antecryst 2 - 66A
● autocryst - 66A
+ unclassified - 66A
■ antecryst 1 - 101A
◆ antecryst 2 - 101A
● autocryst - 101A
+ unclassified - 101A
■ antecryst 1 - 123A
◆ antecryst 2 - 123A
● autocryst - 123A
+ unclassified - 123A
■ antecryst 1 - 124A
◆ antecryst 2 - 124A
● autocryst - 124A
+ unclassified - 124A
■ antecryst 1 - 206B
◆ antecryst 2 - 206B
● autocryst - 206B
+ unclassified - 206B
■ antecryst 1 - 273
● autocryst - 273
+ unclassified - 273
(Yb/Gd)N
(Sm/Ce)N
Th/U
T (°C; Ti-in-zircon)
Hf (ppm)
U/Yb
Nb/Yb